Patterned Aqueous Growth of Single Crystalline Zinc Oxide for Photonic Applications

Patterned Aqueous Growth of Single Crystalline Zinc Oxide for Photonic Applications

A dissertation presented

by

Kathryn Jessica Pooley

to

The School of Engineering and Applied Sciences

in partial fulfillment of the requirements

for the degree of

Doctor of Philosophy

in the subject of

Applied Physics

Harvard University

Cambridge, Massachusetts

April 2015

Dissertation advisor: Evelyn L. Hu Kathryn Jessica Pooley

Patterned Aqueous Growth of Single Crystalline Zinc Oxide for Photonic Applications

Abstract

Typically a top-down approach is used in the fabrication of functional nanodevices beginning with the bulk material and imposing a two or three-dimensional structure on the material through a combination of lithography and etching. Pre-patterning of a substrate, resulting in the selective growth of a material, has potential for forming three-dimensional device structures in ways that can be more efficient and which can avoid process complexity and process induced damage. In this thesis, the low temperature (90°C) aqueous growth of complex, single crystalline zinc oxide (ZnO) three-dimensional devices through pre-patterned micron and nanometer sized molds is presented. This work focuses on the quality of the single crystalline ZnO material, the constrained growth of ZnO through various sizes and shapes of molds, and the fabrication of several device structures including pillars, rings, and photonic crystals. Due to their single crystalline nature and crystallographically smooth sidewalls, photonic devices created using this growth method have the potential to outperform traditionally fabricated structures in a range of optoelectronic applications.

In addition, metal-oxide interfaces are the critical components of many electrical and optical devices, and it is rare to find epitaxial metal-oxide structures. In this work, the first demonstration of low temperature, epitaxial growth of ZnO on single crystalline gold plates is presented. The quality and structure of the ZnO on the gold plates is investigated using

scanning electron microscopy, atomic force microscopy, and photoluminescence spectroscopy. The epitaxial growth is confirmed using electron backscatter diffraction and transmission electron microscopy. The metal-oxide interfaces fabricated have the potential to be used in a number of technologically important applications. Possible examples include creating high quality electrical contacts on high bandgap materials and improving light extraction from planar LED structures.

Table of Contents

Listing of Figures

This work is dedicated to my beloved grandparents: Dorothy Greenberg, Earl W. Harp, and Marian E. Harp.

Acknowledgements

I would like to thank my advisor, Professor Evelyn Hu, for allowing me the opportunity to work in her research laboratory over the past five years. Her enthusiasm, support, and guidance have been instrumental throughout my PhD. I have learned so much throughout my time at Harvard and most of it would not have been possible without Evelyn. She always encouraged me to pursue the research I was most interested in and gave me the freedom to do so while still steering me in the right direction. In addition, she is a tremendously caring and compassionate person who I will truly miss as I move on from my PhD.

I would also like to thank John Joo for all of his help during the first several years of my PhD. I greatly appreciate all of the time that he took to help me learn the ropes of the lab and the details of my ZnO project. He was always there for me when I had a question or was stuck on just exactly what to do next. Thank you also to Kasey, Andrew, and Igor, for all of their guidance and time helping me with my project in many different capacities. It was wonderful to have such smart and talented postdocs in the lab who were passionate about not only research but also helping the graduate students succeed. Christine, thank you for helping me with equipment I was less familiar with, your willingness to help me get to the bottom of a problem I was having with my research, and most of all for being an amazing friend. I am going to miss sitting next to you in the office and all of our chats about anything and everything. David, thank you also for being an amazing friend and for all of your help from PL measurements to simulations. I also always looked forward to our lunchtime conversations and to Friday trivia nights in Boston. Shanying, thank you for being there for me no matter what I needed throughout my PhD. You are such a funny, kind, and caring person who made sure I always kept things in perspective. Your ideas of experiments I could try when I thought nothing would work and your knowledge of so many of the pieces of equipment in both the lab and in CNS were invaluable. I would also like to thank everyone else in the lab, Jonathan, Tsung-li, Nan, Alex W., Danqing, Andy, Alex X., Scott, and Aun,

that I got to know throughout my PhD for all of their help with various parts of my research and for all of the good times that we had over the past 5 years. The group would not be able to function the way that it does without the hard work of Sarah. Thank you for everything that you do from organizing individual meetings with Evelyn to getting to the bottom of who can help with whatever obscure problem has come about.

Thank you also to my committee members, Professor David Clarke and Professor Marko Loncar, for agreeing to be on my committee and for all of their advice and guidance with my research. In addition, thank you to Mor Baram for all of her help with the ZnO on gold work and for all of the TEM measurements that she made for us.

The acknowledgement would not be complete without thanking some of the other people that made this work possible. Thank you to Wallace, Young-Ik, and Anna for all of their insights into many aspects of my research but specifically for all of the time that they took to help me with my FDTD simulations. I am glad that we were all in the same office for so long and were able to become such good friends. Thank you to Mary and Samuel for all of their help with PL measurements and analysis done on the equipment in the Clarke group. Thank you also to all of CNS staff for their hard work maintaining the equipment and for their willingness to share their wealth of knowledge with me regarding my research. There are so many people, more than I can name here, both in Applied Physics and in SEAS that I would like to thank for their help, encouragement, and support during my PhD. I have met amazing people during my time at Harvard who I have made countless memories with that I will remember forever.

Lastly, I would like to thank my family for their love, support, and encouragement throughout my PhD and my entire life. Without them, none of this would have been possible. I am so lucky that for the first three years of my PhD my brother lived only a few minutes away. Thank you Jack for all of the meals together and adventures that we had while you lived in Cambridge. It meant a lot to me to know that you were always close by if I needed a break or just a quick chat. Thank you mom and dad for always being there for me and encouraging me both when I was getting exciting results and also when things just weren't working. I looked forward to each of your countless visits to Boston and enjoyed showing you what I was working on. Last but certainly not least, thank you to my husband, Matt. Throughout my PhD you have supported and been there for me every single day ready

to hear what I was working on and what my next big idea was. I am so thankful for your willingness to move from England to Boston while I finished my PhD and have enjoyed every moment of our time in Boston. I love you and can't wait for life's next adventure.

Chapter 1

Introduction

Wide bandgap semiconductors are a promising avenue for improving and developing semiconductor optoelectronic devices. In addition to creating new devices it is also important to consider how wide bandgap materials can be integrated with existing semiconductor technologies. Semiconductor technology has been widely developed throughout the 20^{th} and 21^{st} centuries as understanding of solid-state physics has drastically increased. The fast paced development of integrated semiconductor circuit technology has revolutionized almost every field of modern life. Most notable is the development of home and mobile computing and the associated dramatic increase in global communication made possible by the development of internet technologies. In addition, technology advances have improved almost every aspect of human life from advanced medical imaging techniques to improved understanding of the solar system via the deployment of autonomous exploration robots.

The most prominent material used in semiconductor technology to date is silicon. Advanced processing techniques have been established for silicon technologies enabling the large-scale mass production of intricate silicon based circuitry. While there has been

explosive growth of silicon integrated electronic devices, the limit of what can be achieved with current approaches is being reached [1], [2]. The size of devices is quickly approaching atomic length scales and improvements in the transmission and processing of information by solely electronic means will soon be no longer feasible. One promising potential solution to this is to integrate optically active components into more established material systems [3]. Direct wide bandgap semiconductors are promising materials for this application as they can be used for high current power control electronics and rapid switching technology [4].

One promising wide bandgap semiconductor is zinc oxide (ZnO). ZnO has long been used in a wide array of non-electrical applications from pigments to medicine because of its material properties [5]. More recently, its potential uses as a semiconductor have drawn considerable attention. Along with other more widely used wide bandgap semiconductor materials such as gallium nitride (GaN), ZnO is promising for optoelectronic devices. Since the early part of the 20^{th} century the structural and optical properties of ZnO have been studied [6]–[9]. Over the past several decades, thin films of ZnO have been fabricated and integrated into several devices such as transistors and LEDs [10]–[13].

Like GaN, which has been an important material in the development of white solid-state lighting, ZnO has an ultraviolet bandgap and wurtzite crystalline structure [14], [15]. There are several advantages to using ZnO instead of GaN. The first advantage is that large single crystalline substrates of ZnO can be produced, which are advantageous for optical and electrical devices [16]. GaN, on the other hand, is typically grown on a substrate of a different material such as sapphire or even ZnO. The lattice mismatch between GaN and sapphire is quite large and leads to numerous defects in the GaN material [17]. Another advantage of ZnO over GaN for optical applications is its larger exciton binding energy. The

exciton binding energy of ZnO is ~60meV, which is larger than the mean electron energy at room temperature (25meV) [18], [19]. Therefore, stable excitons at room temperature in ZnO are possible as well as room temperature UV lasing. GaN, on the other hand, has an exciton binding energy of ~26meV making it very difficult, if not impossible, for lasing to occur at room temperature [19]. Even though there are many advantages of using ZnO over GaN, it has proved difficult to create reliable p-type doping in ZnO and this has prevented it from completely replacing GaN. Recent reports of p-type doping in ZnO are promising, however, the doping has been seen to degrade with time limiting the usefulness in devices [20], [21].

Some additional properties that make ZnO attractive for semiconductor technology include its high piezoelectric constant and high conductivity when doped. ZnO being a highly piezoelectric material makes it attractive for use in ambient energy harvesters or precision actuators. While p-type doping is difficult in ZnO, n-type doping has been extensively shown and leads to conductivities similar to, and in some cases better than, those seen in traditionally used ITO layers [22], [23].

ZnO has already been successfully used in a variety of optoelectronic devices across a range of applications. These include light emitting diodes and solid-state lasers where the high exciton binding energy and large bandgap is advantageous; photovoltaic devices where it has been used as a carrier injecting layer; sensors where its surface chemistry provides high sensitivity to changes in its chemical environment; and transparent transistors which have applications in touchscreen technology. A more detailed overview of ZnO devices and nanostructures can be found in [14], [24]. One of the main challenges associated with using ZnO in optoelectronic devices is fabricating the required device structures and incorporating

them within existing technologies. Several nanostructures of ZnO have been reported including nanowires, nanorods, and photonic crystals to name a few [24]–[26].

Traditionally, top-down fabrication approaches have been used for the creation of optoelectronic devices. These methods typically involve the removal of unwanted material through wet and dry etching processes. While top-down fabrication approaches are accurate and precise, the etching processes needed cause unwanted damage to the material [27], [28]. Bottom-up fabrication of devices, on the other hand, is often much less complex, avoids process-induced damage, and reduces the amount of material wasted. For many bottom-up approaches, top-down fabrication techniques are still needed to create mold structures through which material is grown however, complex three dimensional structures, which would be difficult to create with solely top-down techniques, can be made.

ZnO has been grown using many different growth techniques including chemical vapor deposition, sputtering, electrodeposition, molecular beam epitaxy, pulsed laser deposition, and aqueous processes [14], [15], [24]. This thesis presents work towards the development of complex three dimensional ZnO photonic structures using an aqueous growth technique to selectively grow the required structures. The advantage of aqueous growth is the ability to inexpensively grow high quality single crystalline ZnO at low temperatures with a large amount of control over the resulting structures.

Before proceeding to describe the details of this work, an introduction to the relevant background material is provided in Chapter 2. An overview of semiconductor materials is given along with specific material properties of ZnO. In addition a detailed description of top-down versus bottom-up fabrication processes is elaborated on and details of the aqueous

growth process are presented. Lastly, common defects and dopants of ZnO are mentioned as well as some of their effects on the material properties.

Chapter 3 begins the experimental results of this thesis by detailing the optical investigation of the single crystalline ZnO grown aqueously. Photoluminescence spectroscopy is used to compare the aqueously grown material to both annealed aqueously grown ZnO as well as commercially purchased ZnO. Optical measurements are taken on all three types of samples while they are being heated to further study the material quality. Persistent photoconductivity is also measured and compared for the ZnO samples.

The constrained aqueous growth of ZnO through mold structures is shown in Chapter 4. The fabrication steps for the single crystalline ZnO structures are detailed in the first part of the chapter. Structures grown through molds made with photolithography and electron-beam lithography are studied as well as those grown for various amounts of time, with different concentrations of growth solution, and through different size and shape molds. A detailed analysis of the growth possible is given along with crystallographic studies performed using electron backscatter diffraction.

With the understanding of the types of ZnO structures possible, Chapter 5 presents three specific optical structures that were made out of ZnO and some of the challenges in their fabrication. These structures include microdisk resonators, ring structures, and pillar photonic crystals. In addition, simulations are presented for the microdisk resonators and photonic crystals to explore the structures required for specific applications.

Chapter 6 describes the epitaxial growth of ZnO on single crystalline gold. While ZnO has been epitaxially grown on several substrates, the ability to epitaxially grow a single crystalline continuous film on a metal is advantageous. Details of how changing the growth

kinetics varies both the top surface of the ZnO and the material at the interface are presented. In addition, electron backscatter diffraction and transmission electron microscopy are used to confirm the epitaxial relationship between the ZnO and Au.

Lastly, Chapter 7 summarizes the main results presented in this thesis and provides an outlook for the future of ZnO optoelectronic devices grown using aqueous methods.

Chapter 2

Background

2.1 Semiconductors Overview

The periodic potential of crystalline solids results in an energy range in which no electron states exist. This energy range is known as the bandgap and is critical in determining the electrical and optical properties of a material [29], [30]. In a simple description, which gives the essential elements of the energy landscape of a semiconductor, the bandgap divides the energy structure of a material, creating two energy bands in which electron states exist as shown in Figure 2.1. The lower energy band is known as the valence band and the higher energy band is known as the conduction band. The Fermi level (E_F) is the energy below which all electron states are occupied at a temperature of absolute zero (0K). The position of the Fermi level relative to the conduction and valence bands, combined with the magnitude of the bandgap, determine the electrical properties of a material. In order for a material to be conducting it requires a partially filled band to support a non-zero drift velocity when a voltage bias is applied. In metals, the conduction and valence bands overlap and there is no bandgap as shown in Figure 2.1(a). This means that regardless of where the Fermi level lies there will be a partially filled band, and therefore

metals are good conductors. In insulators, on the other hand, the Fermi level lies within a large bandgap that is much wider than the energy available to thermally excite electrons within the material as shown in Figure 2.1(c). This means that the valence band is completely full and the conduction band is empty, resulting in low electron mobility as expected in an insulator. Semiconductors, as the name suggests, are in between metals and insulators as shown in Figure 2.1(b). Like in insulators, the Fermi level in a semiconductor lies within the bandgap between the conduction and valence bands. This means that at 0K semiconductors do not conduct, as they have a completely full valence band and completely empty conduction band. However, the magnitude of the bandgap in semiconductors is small enough that at temperatures above 0K there is a non-negligible probability of thermally excited electrons occupying states within the conduction band. These conduction band electrons allow semiconductors to conduct, particularly with the addition of dopant states described later. The position of the Fermi level, and thus the occupation of the conduction band, can be controlled by varying the doping within a semiconductor. This allows the conductivity of semiconductors to be varied. In addition, the occupation of the conduction band can be influenced by the application of electric fields, making semiconductors ideal for creating non-linear electrical components such as transistors.

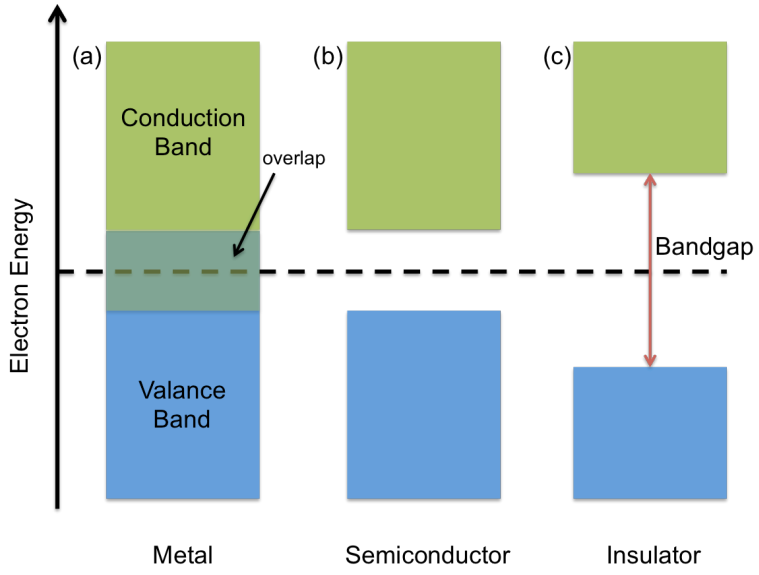

Figure 2.1: Energy bandgaps in (a) metals, (b) semiconductors, and (c) insulators.

Semiconductors can be further divided into two main classes: indirect and direct semiconductors. Indirect semiconductors are less optically active because the minimum conduction band energy does not have the same k-vector as the maximum of the valence band as shown in Figure 2.2(b). This means that optical transitions cannot be driven solely by photons and require interactions with phonons in the crystalline lattice in order to conserve momentum. In direct bandgap semiconductors, the minimum of the conduction band occurs at the same k-vector as the maximum of the valence band, shown in Figure 2.2(a), making optical transitions more efficient as they only require interactions with a photon.

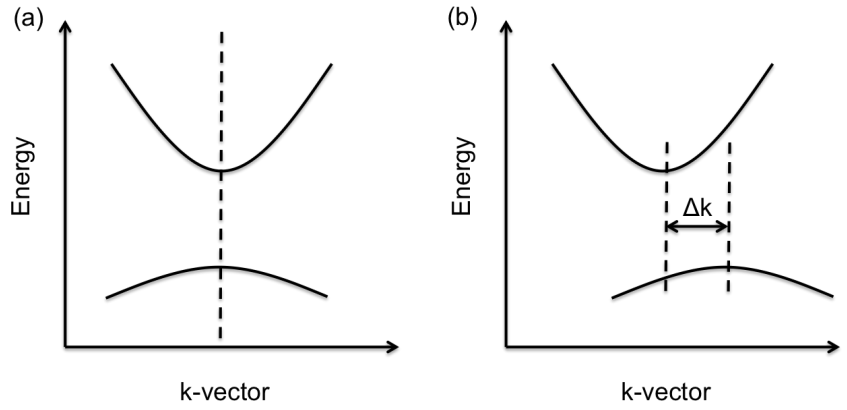

Figure 2.2: Dispersion curves for (a) direct semiconductors and (b) indirect semiconductors.

As mentioned above, the electrical properties, for example the conductivity, of semiconductor materials can be manipulated via the application of external fields or doping. Doping a semiconductor involves the incorporation or removal of mobile charge carriers by donors or acceptors. Two types of doping, n-type and p-type, are possible in materials. In p-type doping, additional positive carriers (holes) are incorporated into the semiconductor by the addition of certain types of atoms. Using silicon as an example, one way that this can be accomplished is by adding a trivalent atom such as boron into the crystalline lattice as shown in Figure 2.3.

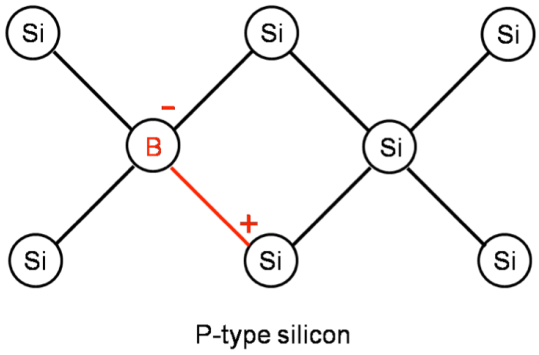

Figure 2.3: P-type doping in silicon using boron electron acceptors.

Typically, silicon atoms form four covalent bonds with neighboring atoms as silicon has four valence shells electrons. Boron however, only has three electrons in its valence shell and therefore can only covalently bond with three of the neighboring silicon atoms. Since there is one less bond when a boron atom replaces a silicon atom a hole is left. The boron atoms can accept an electron from a surrounding silicon atom but now the silicon atom is one electron short and the hole has moved to the silicon. Using a dopant such as boron that accepts electrons from other atoms produces an increased number of holes in the material. Therefore, doping a material with electron acceptors produces p-type doping. If instead an electron donor, for example a phosphorus atom, replaces one of the silicon atoms in the crystalline lattice, as shown in Figure 2.4, the material becomes n-type doped. In this case, the phosphorous atom has five loosely bound valence electrons however; it is only able to make four covalent bonds to nearby silicon atoms. An extra electron is remaining that is only loosely bound and can therefore move around the lattice of the crystal. As the incorporation of phosphorous introduces an extra electron into the material, it is known as an electron donor and leads to n-type doping.

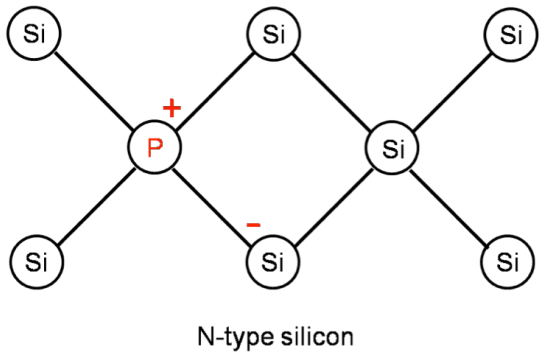

Figure 2.4: N-type doping in silicon using phosphorous electron donors.

In many semiconductors the location and concentration of dopants can be precisely controlled. Current is the movement of free charge carriers (electrons and holes) in the semiconductor, and the ability to change the concentrations of these carriers in specific regions is a powerful tool for numerous structures such as p-n junctions [31]. The addition or removal of charge due to doping changes the electronic band structure of the material relative to the Fermi energy (E_F) by the addition of energy levels in the bandgap. For p-type doping, incorporating additional electron acceptors produces an energy level near the valence band, typically in the range of meV from the valence band edge. Electrons in the valence band can occupy those dopant states, thus creating holes in the valence band. The effect of this p-type doping is that the Fermi level shifts closer to the valence band, as shown in Figure 2.5. For n-type doping the opposite effect occurs. The incorporation of electron donors in the semiconductor material creates additional energy levels inside the bandgap with energy slightly less, typically on the order of meV, than that of the conduction band. As the energy of the defect level is not very different than that of the conduction band, electrons can be easily promoted into the conduction band causing a shift of the Fermi level closer to the conduction band. The ability to change the position of the Fermi energy is advantageous as it allows for engineering of the electrical properties of the semiconductor.

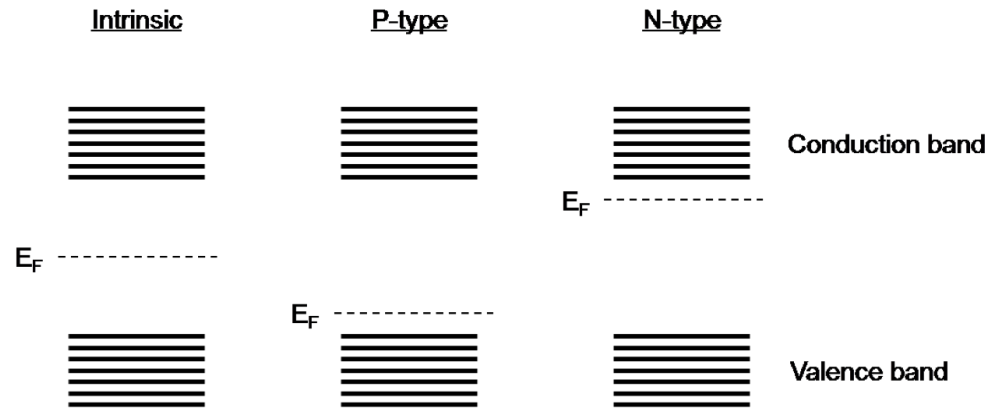

Figure 2.5: Shift in the Fermi level energy (E_F) relative to the electronic band structure due to doping.

Semiconductors are popular materials for optical devices and numerous devices such as lasers, LEDs, and optical interconnects have been researched, developed, and commercially produced [32]–[34]. Semiconductors interact with light via transitions of electrons across the bandgap of the material. When light is incident upon a material the absorption of photons promotes electrons from the valence band to the conduction band creating photo-generated carriers. Recombination events, where an electron in the conduction band transitions into a hole in the valence band, result in the emission of a photon from the semiconductor. The energy of the emitted photon directly corresponds to the change in energy of the electron as it transitions between the bands. In addition to photo-driven transitions, semiconductors interact with light via their dielectric constant/ refractive index. Engineered semiconductor structures can be used to create periodic variations in the refractive index encountered by a propagating light wave. This allows for a wide range of photonic applications and devices such as photonic crystals, distributed Bragg reflector mirrors, and waveguides [35]–[37].

2.2 Bottom-Up Fabrication

There are two distinctive approaches used for the fabrication of semiconductor structures and devices: top-down and bottom-up. Typically, a top-down approach is used where fabrication begins with a bulk piece of the desired semiconductor. Structures are formed by the selective removal of material using various etching techniques. Two of the most commonly used etching methods are reactive ion etching and wet chemical etching. Both of these etching methods result in the removal of unwanted material. A schematic example of a top-down fabrication approach is depicted in Figure 2.6. A layer of resist is evenly spin coated onto the bulk semiconductor. Lithographic patterning of the resist results in a mask for the subsequent etching process. With the mask made on top of the semiconductor, a reactive ion etch is used to form tall pillar structures. The final step in the top-down fabrication of nanopillars shown here is the removal of the remaining mask material using an appropriate wet chemical etch. Top-down fabrication is used in the fabrication of numerous other structures including photonic crystals, lasers, and resonators [38]–[41].

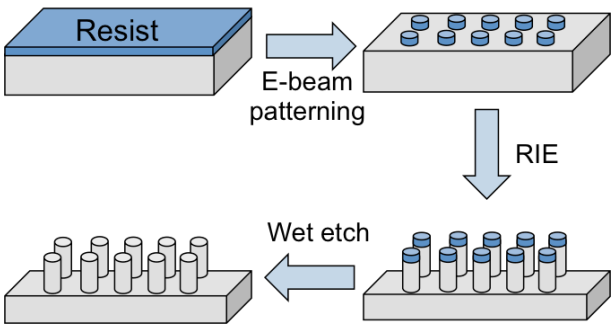

Figure 2.6: Schematic representation of top-down fabrication. A pattern is created in a layer of resist and transferred to the underlying material via an etching process.

Bottom-up fabrication, on the other hand, involves controlling the growth of the semiconductor material. The size and shape of the structures formed using this fabrication method are determined by the thermodynamics and kinetics of the growth system and material. The bottom-up growth technique will be extensively used throughout this thesis. A schematic of a bottom-up growth fabrication process is shown in Figure 2.7. An appropriate material is chosen as the substrate for the material growth such that, typically, the lattice constants and crystal structure of the two materials are similar. Resist is then evenly spin coated onto the clean substrate. Lithography is used to open up holes in the resist through which the semiconductor growth can occur. Once the fabrication of the mold is complete, the semiconductor material is grown from the regions of bare substrate. Initially, the lateral growth of the material is constrained by the mold, however, once the growth reaches the top of the mold the material will continue to grow unconstrained. The growth continues until structures of the desired size are produced, at which point the sample is removed from the growth solution and the resist is removed from the sample. The example of the bottom-up growth fabrication shown in Figure 2.7 is similar to the method used throughout this work. Other variations of bottom-up fabrication of semiconductor structures have also been used but they all involve the growth of a material from or through a chosen area [42]–[45].

Another example where bottom-up fabrication is used is in the vapor-liquid-solid growth of semiconductor nanowires. This fabrication technique has resulted in nanowires of GaAs, ZnO, and many other semiconducting materials [46], [47]. For this technique metal nanoparticles are deposited onto the surface of a bulk semiconductor layer. Through the use of chemical vapor deposition and annealing of the sample, growth of the semiconductor occurs at the interface of the semiconductor and the metal nanoparticles resulting in

nanowires. Bottom-up growth is a powerful fabrication method for the formation of many high quality semiconductor devices.

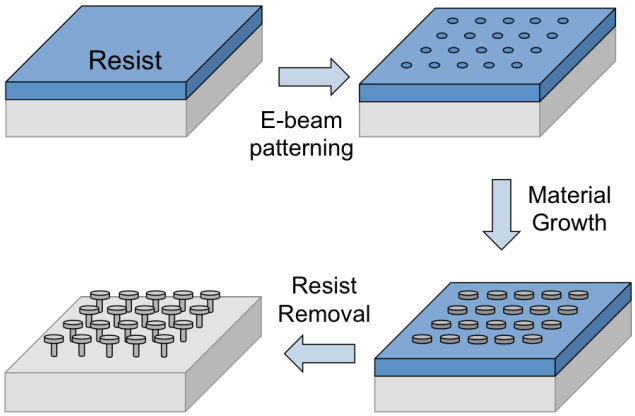

Figure 2.7: Schematic representation of bottom-up fabrication. A pattern is created in a layer of resist and material is grown through the mold.

The top-down and bottom-up growth techniques both have advantages and disadvantages, and depending on the semiconductor material and the desired device one technique may be more appropriate than another. Top-down fabrication techniques have been the most widely used to date. Therefore, there are often well-developed fabrication methods for certain material systems. This is certainly true for silicon as it is the most common semiconductor currently used. Another advantage of top-down fabrication is that it is accurate and precise. The masks used for etching are often made using lithography tools, such as e-beam lithography, and allow for the precise patterning of the resist. This pattern can then be transferred to the semiconductor using etching processes. Therefore, fine control of patterned designs in the mask resist often directly translate to the structures that are made. However, there is a major drawback to top-down fabrication. The use of etching techniques, both wet and dry, often results in unwanted damage to the semiconductor material [48]–[51].

Bottom-up fabrication is advantageous as it allows for the formation of structures that are difficult to obtain using top-down methods. For example, using a top-down fabrication technique it can often be difficult to create the undercut structures that are desirable for many optical devices. Bottom-up fabrication however, as shown previously in Figure 2.7, allows for formation of such structures without elaborate processing methods. The bottom-up fabrication is also advantageous as there is little material waste. In addition, as will be discussed in more detail in later chapters, bottom-up growth can result in structures with crystallographically smooth sidewalls and minimal structural defects. Bottom-up growth offers additional flexibility for the integration of other materials within structures. For example, materials could be embedded within the larger structure by halting the growth process and depositing additional materials before resuming growth.

2.3 Zinc Oxide Material Properties

In this work the semiconductor being investigated is zinc oxide (ZnO). ZnO is a direct, wide bandgap semiconductor, has a large exciton binding energy, and has a large thermal conductivity [14], [15]. The bandgap of ZnO can be engineered by alloying the material with either MgO or CdO [14], [15], [52]. The refractive index of zinc oxide is approximately 2.0 [14], [53]. Many of the material properties of ZnO will be discussed in detail throughout this section. ZnO has many similar properties, such as crystalline structure and bandgap, to the more commonly used semiconductor gallium nitride (GaN). The bandgap of ZnO is 3.37eV while that for GaN is 3.4eV [19], [54], [55]. Over the past several decades GaN has been increasingly used in optoelectronic devices due to its emission in the UV-blue region, and in 2014 the Nobel Prize was awarded to Isamu Akasaki, Hiroshi

Amano, and Shuji Nakamura for their development of efficient blue light emitting diodes [56], [57]. LEDs, lasers, and other optical devices used in many applications such as displays, flashlights, and traffic lights have been made using GaN [58].

Interest in using ZnO for optoelectronic applications has also increased over the past decade as it has several advantages over GaN. GaN can be difficult to grow without the inclusion of threading dislocations and other defects due to the large lattice mismatch between it and the sapphire substrate it is often grown on [17], [59]. Large area single crystalline substrates of ZnO, on the other hand, can easily be fabricated and have lead to a surge in ZnO optical devices such as LEDs, lasers, sensors, and photodetectors [15], [16]. In addition, there are a variety of growth techniques, which will be discussed in the following section, for ZnO that allow for a wide array of structures and devices to be fabricated. For optical devices one of the key advantages of ZnO over GaN is the large exciton binding energy of ~60meV compared to ~26meV for GaN [18], [19]. The mean electron energy at room temperature is about 25meV. Therefore, excitons in ZnO are stable at room temperature, while those in GaN are easily dissociated. In addition, the larger exciton binding energy for ZnO allows for room temperature UV lasing in ZnO devices, which is not possible in similar devices made with GaN.

Zinc oxide can have three different crystalline structures shown in Figure 2.8: hexagonal wurtzite, zinc blende, and rocksalt [14], [60], [61]. The hexagonal wurtzite crystalline structure is the most common as it is thermodynamically stable in ambient conditions. The zinc blende crystalline structure is possible with growth on cubic substrates, while high pressures are need for ZnO to have a cubic rocksalt structure.

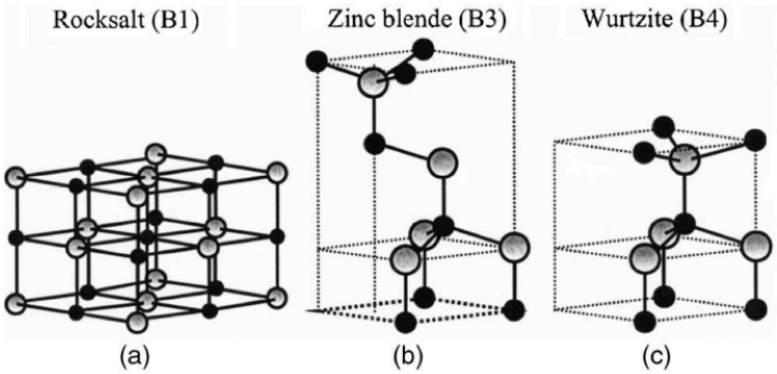

Figure 2.8: Three crystalline structures of ZnO from [14]. Reprinted with permission from U. Özgür, Y. I. Alivov, C. Liu, A. Teke, M. A. Reshchikov, S. Doğan, V. Avrutin, S.-J. Cho, and H. Morkoç, "A comprehensive review of ZnO materials and devices," *J. Appl. Phys.*, vol. 98, no. 4, p. 041301, 2005. Copyright 2005, AIP Publishing LLC.

The hexagonal wurtzite structure for ZnO is shown in Figure 2.9 [62]. The crystal is made up of two interpenetrating close-packed hexagonal lattices with a stacking sequence along the vertical [0001] axis of AaBbAaBbAaBb where the capital letters refer to zinc atoms and the lower case letters to oxygen atoms. The crystalline structure has a hexagonal unit cell with lattice constants a=0.325nm and c=0.52nm. The space group for ZnO in the Schoenflies notation is C_{6v}^4 and $P6_3mc$ in the Hermann-Mauguin notation [25], [63]. Each of the zinc atoms in the crystalline lattice is surrounded by four oxygen atoms, which form the corners of a tetrahedron. In addition, four zinc atoms in the same configuration surround each oxygen atom in the lattice. In many ZnO crystals, there is a slight distortion and variation in the c/a value.

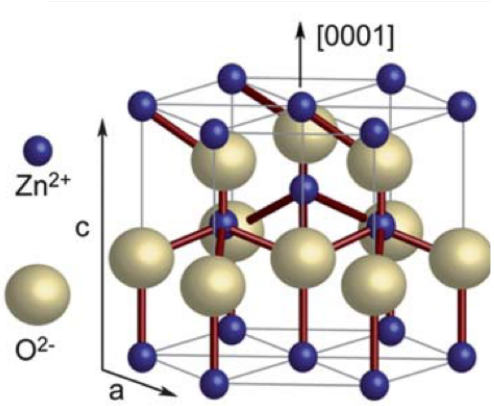

Figure 2.9: Hexagonal wurtzite structure of ZnO. Reproduced from Ref [62] with permission of The Royal Society of Chemistry.

There are several prominent and important crystalline planes of ZnO in the wurtzite structure as shown in Figure 2.10. The basal planes are the (0001) and the $(000\bar{1})$ planes. The (0001) plane is made entirely of zinc atoms while the $(000\bar{1})$ plane consists only of oxygen atoms. As there is no inversion point in the crystal structure a polarity in ZnO exists. The non-zero dipole moment is the result of a positively charged Zn-(0001) surface and a negatively charged O-$(000\bar{1})$ surface and leads to the piezoelectric properties in ZnO. The basal plane of most interest is the (0001) plane and is referred to as the c-plane in the crystal, shown in Figure 2.10(a). Several groups have investigated which basal plane is most seen in crystal growth using etching techniques [64], [65]. Since the (0001) and the $(000\bar{1})$ planes etch at different rates, researchers were able to determine that vertical growth occurs in the (0001) direction. Prism planes in ZnO are the $(10\bar{1}0)$ and $(11\bar{2}0)$ planes. The m-planes, which produce the hexagonal shapes in the structures, are the $(10\bar{1}0)$ planes and are shown in Figure 2.10(b). The a-planes are the $(11\bar{2}0)$ prism planes, as shown in Figure 2.10(c) and also create hexagonal structures rotated 30° from those defined by m-planes. The final planes of interest in ZnO are the pyramidal $(1\bar{1}02)$ r-planes shown in Figure 2.10(d).

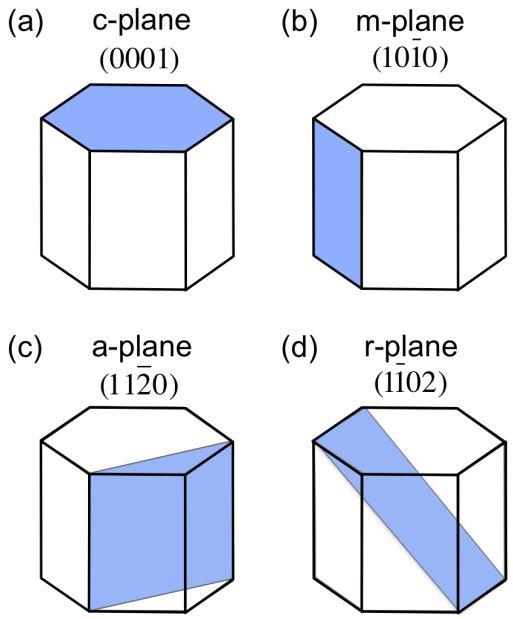

Figure 2.10: Crystalline planes in ZnO.

The surface energies of the c-plane, m-planes, and a-planes are important to understand as they determine the sizes and shapes of ZnO structures. The (0001) basal plane has been found to have the largest surface energy, and therefore the fastest growth rate occurs in the (0001) direction [25]. This fast growth rate in the vertical direction leads to the tall structures, which will be seen throughout this thesis. The (10$\bar{1}$0) m-planes have the second highest surface energy and cause the ZnO to grow out laterally from a point [66]. Finally, the (11$\bar{2}$0) a-planes have the lowest surface energy out of the three planes mentioned here, and therefore growth in this direction is the slowest [66]. Using the ZnO aqueous growth technique described in the next section, these crystalline planes will be apparent in the ZnO structures fabricated and discussed throughout this work.

In addition to crystalline properties of bulk materials it is often important to consider the crystalline properties of interfaces between different materials. The configuration of

atoms at the surface of a material is often different than that in the bulk. This is because the atoms at the surface have dangling bonds and rearrange themselves to minimize their surface energies. The abrupt change in lattice constant at the boundary between two materials causes a rearrangement of the atoms at the interface. The relationship between the crystalline structures on each side of the boundary is used to classify the interface. If there is a well defined relationship between the crystalline structures of the two materials where they join the interface is considered epitaxial. This is in contrast to the case where there is a random relationship that varies over the interface. Epitaxial interfaces are often desirable for optoelectronic devices because they can lead to superior electrical and optical properties. It has been shown that ZnO can be epitaxially grown on several substrates including GaN, spinel, and silicon carbide [52], [65], [67]. The epitaxial growth of ZnO on single crystalline gold will be presented in Chapter 6.

2.4 Aqueous Growth

ZnO has been grown and deposited using many different methods including sputtering [68], molecular-beam epitaxy [69], chemical vapor deposition [70], and pulsed laser deposition [52]. In addition, several methods such as electrodeposition [71], chemical bath deposition [72], and hydrothermal growth [73] have also been used. Many of these techniques require high temperatures, which is not always ideal for device fabrication.

The ZnO grown in this thesis was done using a low temperature (90°C) aqueous growth technique developed by Lange et al. [74], [75]. This technique is advantageous as it avoids high temperature processing and is often more cost effective. The growth solution consists of zinc nitrate, ammonium hydroxide, and water. The spinel ($MgAl_2O_4$) substrates

used throughout this work were chosen because of the small lattice mismatch (as low as ~1.3%) between ZnO and $MgAl_2O_4$, as well as the ability to epitaxially grow ZnO on spinel [65]. ZnO grown on $MgAl_2O_4$ using plasma assisted molecular beam epitaxy was found to have a 13.6% lattice mismatch [76]. More recently, it has been determined that there is a 30° rotation, with respect to the perpendicular of the substrate surface, between the close-packed directions in the ZnO and spinel when ZnO is grown hydrothermally. The effect of this rotation is that, at the interface between the ZnO and spinel, tetrahedral sites are available for zinc atoms to attach to. With the zinc atoms attached to the spinel, growth can begin [65].

The first step in the aqueous growth process of ZnO is a nucleation step. A seed layer can be formed on the substrate in a variety of ways including by vapor deposition, a rapid change in the pH of a zinc nitrate and ammonium nitrate solution [77], the thermal decomposition of a zinc-organic precursor in solution [78], or solution deposition of prefabricated ZnO nanoparticles [79]. Here the seed layer is formed during an aqueous nucleation process. Zinc nitrate, ammonium hydroxide, and water are placed in a Teflon container with the spinel substrate. The substrate is suspended upside down in the solution using a custom made Teflon holder. In contrast to chemical bath techniques, the Teflon container is tightly closed which allows for an increase in the pressure in the container during nucleation. The Teflon container is placed in a microwave oven for 25 seconds, which quickly raises the temperature of the solution. Richardson and Lange have studied the thermodynamics of the aqueous growth of ZnO and found a surprising retrograde solubility [74]. As the temperature of the solution increases, the solubility of the zinc species in the solution decreases. The rapid change in temperature of the solution causes a supersaturation to occur leading to ZnO nucleation on the spinel substrate. As the change in the solubility of

the zinc oxide occurs quickly and many ZnO nuclei form, the amount of ZnO growth is limited during this step. Individual, densely packed ZnO nuclei are epitaxially formed on the substrate. As the polar, basal c-planes have the highest surface energies, ZnO growth will result in tall nuclei with the same orientation. These nuclei all have a similar height because they are all created simultaneously and subjected to the same growth duration.

The second step of the aqueous growth process involves a similar solution of zinc nitrate, ammonium hydroxide, sodium citrate, and water. The nucleated sample is put upside-down in the growth solution in a closed Teflon container. The container is then placed in a 90°C oven for several hours. As the growth solution warms, a supersaturation occurs due the retrograde solubility of ZnO as discussed by Richardson and Lange in [74]. In contrast to the nucleation step, the slow increase in temperature allows for ZnO growth to occur and for the solution to remain near equilibrium. There are several variables, including temperature, growth time, pH, concentration of the zinc salt in solution, and choice of ligand, that can change the growth of ZnO. How these different variables can change the aqueous growth has been studied by several groups [74], [80]. The ability to change various factors in the growth solution leads to the creation of a variety of different ZnO topologies including micro-islands, nanowires, platelets, and smooth continuous films [74], [77], [81]. In addition, the kind of growth and the surface morphology of the resulting ZnO structures can be controlled by varying the growth conditions. In this work, many of the variables, such as temperature, pH, ligand, and substrate, are kept fixed. In Chapter 4, a study is done into the growth rates of the ZnO in different directions with various concentrations of zinc salts in the growth solution. In addition, the growth time is chosen for many of the structures presented such that the optimal shape is produced. Typically, the growth solution is depleted of

nutrients after about 4 hours of growth however, the growth solution can be refreshed and ZnO growth will continue as before.

A detailed description of the growth chemistry can be found in [80] however, a summary of the solution chemistry is included here. In the aqueous solution, the zinc cations (Zn^{2+}) are solvated by water to form $[Zn(OH_2)_n]^{2+}$. The nearby water molecules are deprotonated due to polarized Zn-OH_2 bonds. In dilute solutions, a range of monomeric species can exist denoted as $[Zn(OH_2)_{n-p}(OH)_p]^{(2-p)+}$. Particulates of ZnO can condense out of the solution in a two step process. The first step is known as olation and is described by

$$\text{Zn-OH} + \text{Zn-OH}_2 \rightarrow \text{Zn-OH-Zn} + \text{H}_2\text{O} \tag{2.1}$$

which enables

$$\text{Zn}_2\text{-(OH)}_2 \rightarrow \text{Zn-O-Zn} + \text{H}_2\text{O}. \tag{2.2}$$

As zinc hydroxide is amphoteric, the solubility of ZnO is dependent on the pH of the solution. Often hexamine (sometimes referred to as hexamethylenetetramine (HMT)) is used as a pH buffer. The slow decomposition of hexamine into formaldehyde and ammonia leads to a gradual increase in the pH of the solution. This in turn causes the solubility of ZnO to gradually reduce with time resulting in the forced hydrolysis of Zn aqua-ions and the precipitation of ZnO. It is the effect of the ammonia as a ligand for the Zn ions that leads to the retrograde solubility which is crucial for the nucleation and growth technique discussed above [74].

To more easily form thin films of zinc oxide, sodium citrate was added to the growth solution. Sodium citrate preferentially binds to the (0001) surface of ZnO and reduces the number of sites where growth can occur on this plane [82], [83]. This in turn allows for the manipulation of the aspect ratio of resulting structures by inhibiting the vertical growth of the

material and allowing for additional lateral growth. At low sodium citrate concentrations the height to width ratio of the structures decreases. With high concentrations of sodium citrate it has been shown that ZnO platelets form. Therefore, careful control of the amount of sodium citrate can allow for the creation of various structures. In addition, it has been shown that adding ethylenediamine during the growth decreases the growth rates of the $(10\bar{1}0)$ m-planes due to the adsorption of ethylenediamine onto those surfaces [82]. The addition of sodium citrate into the growth solution allows for the coalescence of the nuclei formed during the nucleation step into a thin film of ZnO. Most of the structures grown and presented in this thesis are grown with sodium citrate in the solution leading to structures with flat tops. When the sodium citrate is removed, as is the case for the photonic crystals presented in Chapter 5, tapered rod structures form.

In order to form many of the structures and devices in subsequent chapters, a base layer of ZnO is first grown on the substrate using the nucleation and growth method described above. Photolithography and electron beam lithography are then used to pattern a mold on top of the base layer. This mold restricts the regions where subsequent ZnO growth can occur. During additional growth steps, the lateral ZnO growth is constrained until the ZnO reaches the top of the mold where it then grows unconstrained. Constraining the growth via a mold, made of a layer of patterned resist, allows for custom shapes to be created and the ability to selectively grow semiconductor structures, which is important for their integration into devices.

The aqueous, bottom-up growth of ZnO is advantageous over other techniques as it epitaxially forms a single crystalline layer of ZnO at a low temperature with little waste of material. In addition, structures grown with this aqueous technique have crystallographically

smooth, vertical sidewalls, which is often difficult to achieve with traditional fabrication methods. Such sidewalls are highly desirable for a wide range of optical and photonic applications where surface roughness and non-vertical sidewalls can significantly degrade the performance of devices. Therefore, bottom-up aqueous growth has significant potential for drastically improving the next generation of integrated optoelectronic devices.

2.5 Defects and Doping in ZnO

Defects in ZnO can profoundly alter the electrical and optical properties of the material. As with other semiconductor materials, one common use of defects in ZnO is for creating doping. The first part of this section will discuss common defects found in ZnO and the second part will describe some common impurities used for doping.

2.5.1 Defects

When defects are present in a material additional trapped states within the bandgap are created. If a photon is incident on a material with defect states inside the bandgap the optical transitions that occur will be different than those in a material with no defects. In addition, the trapped states can change the electron mobility within the material. Some common types of defects in crystalline materials are vacancies, interstitials, and anti-site defects. Vacancies are the absence of certain atoms from their usual positions in the crystalline lattice. They are denoted V_x where V means it is a vacancy and x is the type of atom missing. Interstitials are the inclusion of atoms into the lattice where there typically would not be an atom. An interstitial defect is written as Y_i where Y is the additional atom in the lattice and i indicates it is an interstitial. Finally, anti-site defects are where one atom (atom A) in the lattice replaces another (atom B). The way to indicate an anti-site defect

where atom A is in atom B's usual position is A_B. These three types of defects are found in many types of crystalline structures.

Zinc oxide is a semiconductor material that is intrinsically grown with defects. It is typically a n-type semiconductor as grown due to included defects. Several defects are native to zinc oxide including: oxygen vacancies (V_o), zinc vacancies (V_{Zn}), oxygen interstitials (O_i), zinc interstitials (Zn_i), oxygen anti-sites (O_{Zn}), and zinc anti-sites (Zn_O) [15], [84]–[86]. One common way to study defects in ZnO is using photoluminescence spectroscopy where light of a certain wavelength is incident on the sample and the luminescence from the ZnO is analyzed. Three common bands in the visible range of the photoluminescence of ZnO have been studied: green, yellow, and red [14], [87]. The exact origin of these emission peaks is subject to ongoing research. In particular, there have been a lot of different reports about the origin of the green emission from ZnO including from zinc interstitials [88], oxygen vacancies [89]–[92], ZnO anti-sites [93], and extrinsic impurities [94], [95]. However, the present consensus is that the green emission is due to zinc vacancies [85]; the yellow emission is due to oxygen interstitials or lithium dopants [96], [97]; and the red emission is due to zinc interstitials [98].

As grown zinc oxide is found to be a n-type semiconductor. For decades research has been performed to determine the exact defect causing the material to be n-type. In the 1950's it was found that hydrogen acts as a shallow donor in ZnO [99], [100]. While it had been reported that hydrogen is a likely cause of the n-type properties, it was widely believed for the next several decades that the n-type properties were caused by intrinsic oxygen vacancies and zinc interstitials that were acting as shallow donors [101]. In 1999, Look et al. did high energy electron irradiation on ZnO samples and reported that the main shallow donors in

ZnO are zinc interstitials or zinc interstitial related complexes [101]. This however, turned out to not be the case after several groups performed first principles investigations. Kohan et al. found, using a first principles pseudopotential approach, that native defects in ZnO are not present in high concentrations as shallow donors. Shortly thereafter, Van de Walle et al. reported a first-principles density functional theory investigation where it was determined that the incorporation of hydrogen is likely the cause of the n-type conductivity in ZnO [86], [102]. This was experimentally confirmed in 2002 when electron paramagnetic resonance (EPR) and electron nuclear double resonance (ENDOR) spectroscopy were performed on ZnO samples [103]. It is interesting to note the unusual behavior of hydrogen in ZnO. In most semiconductors hydrogen can either donate an electron or accept an electron [104]. In ZnO however, hydrogen has a low ionization energy and only acts as a donor by tightly binding to oxygen in the crystalline lattice forming OH bonds [85], [86], [105], [106]. Hydrogen is also very mobile and large amounts can easily be incorporated into materials [14]. As hydrogen is always present, it is not surprising that ZnO grown by many different techniques is found to have n-type conductivity. In terms of the aqueous growth method described in the previous chapter, it has been shown that large amounts of hydrogen are incorporated into the ZnO [107], [108]. This incorporated hydrogen is due to residual water in the sample or $Zn(OH)_2$.

2.5.2 Doping

Doping is the intentional inclusion of impurities within the crystalline structure in order to change the concentration of available free carriers. Unlike the intrinsic defects described in the previous section, doping is useful as a way to manipulate the local electrical properties of the material in order to fabricate devices, such as pn junctions. As mentioned

ZnO as grown is a n-type semiconductor, and while many reports of n-type doping exist, p-type doping has proven to be difficult. N-type doping in ZnO has been shown with several different Group III elements of the periodic table, such as Al, Ga, and In. These elements are used for n-type doping in ZnO because they contain an additional electron in their outer shells compared to Zn. Therefore, when Al [109], [110], Ga [111], [112], or In [113] replace Zn in the crystalline structure additional electrons are present, which in many cases causes degenerate doping. Group VII elements of the periodic table, such as Cl [114] and I [115], that replace oxygen atoms in the lattice can also cause n-type doping in ZnO. N-type doping has been shown to cause a large increase in the conductivity of ZnO. ZnO doped with Al for example has been used as a replacement for ITO in several devices [116]. P-type doping in ZnO, on the other hand, has proven to be very difficult. The difficulty of p-type doping is thought to be due to a number of things including the inherent n-type doping and large acceptor activation energies. There have been reports of p-type doping in ZnO using N [117], As [118]–[120], P [121], Sb [122], and Li [123] elements however, reproduction and interpretation of the results has proven difficult.

Chapter 3

Optical Properties of Aqueously Grown ZnO

3.1 Introduction and Motivation

Although optical properties of zinc oxide have been studied extensively over the past few decades, understanding the specific properties of low temperature, aqueously grown material is important as we look to incorporate it into high quality devices. As mentioned in Chapter 2, ZnO is a direct, wide bandgap semiconductor that can show luminescence in several energy ranges based on the quality of the material and the types of defects present. In addition, ZnO has a high exciton binding energy (~60meV), which is much larger than the mean electron energy at room temperature (~25meV). This large exciton binding energy enables emission from the exciton states at room temperature; a major advantage for UV optical applications. The growth method for our ZnO is water-based which can lead to several types of defects in the material due to residual water and OH^- that are trapped in the material. Therefore, several optical experiments were performed to investigate the material quality.

In this chapter, the band edge and green defect band luminescence of both aqueously grown single crystalline material and commercially purchased single crystal ZnO from MTI are investigated. The commercial sample is used as a baseline to which the aqueously grown material is compared. Previous studies have measured the photoluminescence from both bulk and nanostructures of ZnO [98], [124]–[126]. While there has been debate in the research community about the exact sources of different luminescent transitions, it is widely agreed that the bandgap of ZnO is approximately 3.3eV and that there is a green defect band centered between 2.4eV and 2.5eV [15], [127], [128].

Photoluminescence has been conducted at room temperature on many ZnO samples, although very little has been reported about measurements made on aqueously grown material [77], [129]. One group has focused on using self-assembled monolayer templates and growing ZnO at low temperatures using an electroless deposition method [108]. While the fabrication process involves aqueous growth, the ZnO produced is not smooth nor single crystalline. Several low temperature photoluminescence measurements have determined the main excitonic lines present in ZnO [19], [130]–[133]. A few more recent reports have also investigated luminescence from ZnO at elevated temperatures up to 1350°C [134]–[136]. A more in depth investigation into the material properties is possible by heating the ZnO. An increase in temperature results in a greater probability of donor impurities being ionized and may lead to the out-diffusion or removal of impurities. In the case of aqueous growth, where water is involved in the growth process, heating the ZnO during photoluminescence measurements allows for the observation of the effects of the included water and at what temperatures they are most prevalent. The photoluminescence of the as-grown ZnO shows the presence of additional energy levels that are most likely associated with the aqueous

growth method of the material. Thermal treatment of the aqueously grown ZnO however, removes the majority of those states. A comparison of the photoluminescence of the annealed sample and the commercial ZnO prove that high quality single crystalline ZnO can be grown using a low temperature aqueous growth method. Understanding the optical properties of the ZnO will allow for the ability to optimally design optoelectronic devices using low temperature, aqueously grown ZnO.

3.2 Experimental Setup

All photoluminescence measurements were taken on a LabRAM ARAMIS integrated confocal microRaman system. The confocal microscope is coupled to a 460-mm focal length spectrograph including four (600, 1200, 1800, and 2400 lines/mm) gratings as shown in Figure 3.1.

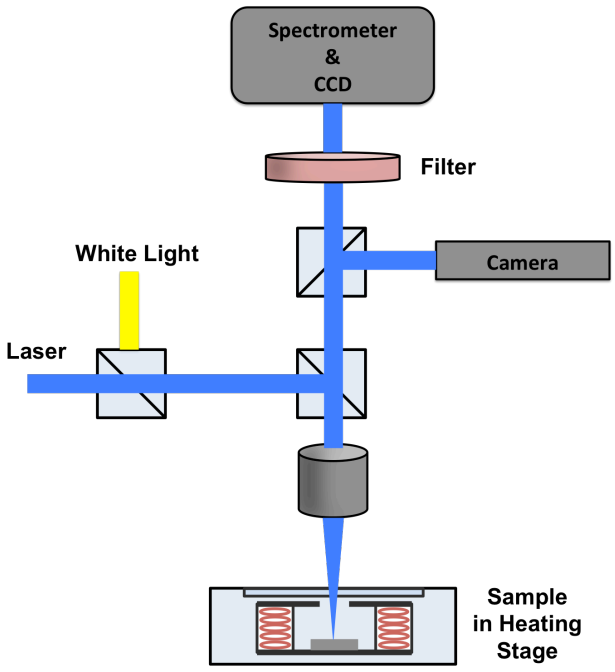

Figure 3.1: Experimental setup of LabRAM ARAMIS integrated confocal microRaman system with 325nm He-Cd laser and sample heating stage.

A white light source and camera are used for visualization of the sample. The system consists of several lasers including a 325nm He-Cd laser used in this work. The incoming laser is directed to the microscope through changeable neutral density filters that attenuate the laser (D0, D0.3, D0.6, D1, D2, D3, and D4) where D0 is no filter in the path. Attenuations produced by the neutral density filters are shown in Table 3.1.

Neutral Density Filter	Power
D0	P_0
D0.3	$P_0/2$
D0.6	$P_0/4$
D1	$P_0/10$
D2	$P_0/100$
D3	$P_0/1000$
D4	$P_0/10000$

Table 3.1: Power attenuation of neutral density filters in LabRAM ARAMIS system.

In the majority of the experiments performed in this chapter a 10x objective (purchased from OFR) producing a spot size of ~10μm in diameter was used. The power measured after the objective, P_0, was found to be 2.8mW. In the remaining experiments a 100x UV objective was used. Light is collected back through the selected objective and is dispersed by a grating onto a CCD multichannel detector. Appropriate exposure time, iterations collected, and neutral density filters were used and determined for each experiment as to not saturate the CCD detector during the photoluminescence experiments.

All heating measurements were done in a remotely controlled Linkam Scientific TS 1500 hot-stage, which had a thermocouple in it to measure the temperature. In this work, set

temperatures ranged from room temperature to 700°C. Before high temperature photoluminescence measurements were taken the hot-stage was set to stay at the desired temperature for at least 5 minutes, during which time the temperature stabilized. For all heating measurements the 10x long working distance objective was used so there would be room for the hot-stage in the microscope setup.

3.3 Details About Fits to the Photoluminescence Data

Throughout this chapter the band edge peaks in the photoluminescence spectra are fit using Voigt functions. Ideal band edge emission would result in a Lorenzian lineshape, however broadening mechanisms lead to the inclusion of a Gaussian component necessitating a Voigt fitting function. As will be seen throughout this chapter, it is believed that the asymmetric band edge peak measured for the aqueous ZnO samples is actually two overlapping transition distributions each with their own mean energy. To accurately extract the emission from these two transitions we use the fitting function:

$$\text{Intensity}= a\left(0.9*\text{gauss}\left(\frac{x-p}{w}\right)+0.1*\text{loren}\left(\frac{x-p}{w}\right)\right)+d\left(0.7*\text{gauss}\left(\frac{x-p+c}{b}\right)+0.3*\text{loren}\left(\frac{x-p+c}{b}\right)\right)$$

where *a* is the amplitude of the first peak, *p* is the mean energy of the first peak, *w* is the width of the first peak, *d* is the amplitude of the second peak, *b* is the width of the second peak, and *c* is the splitting in energy between the means of the two peaks. In an attempt to extract the mean energy of each distribution, the fit is constrained by fixing the ratio of the Gaussian component to the Lorenzian component for each Voigt function. This ratio was chosen as it fit the data the best over a wide range of temperatures.

3.4 Sample Preparation

Single crystalline $MgAl_2O_4$ (spinel) substrates purchased from MTI were used as the substrate for ZnO nucleation and growth. These substrates were chosen due to the similar crystalline structure of the ZnO and spinel and the ability for epitaxial growth of ZnO [65]. Figure 3.2 shows the crystal structure of the spinel, the ZnO at the interface, and the overall ZnO structure. It has been reported by Lange et al. that a 30° rotation of the close packed oxygen directions of the two materials occurs when ZnO is grown on spinel. Without the rotation of the material the lattice mismatch between ZnO and spinel would be 13.6%. With the 30° rotation however, the lattice mismatch becomes -1.6% [65]. The negative sign indicates that the ZnO is under tensile stress and that the atoms in the ZnO are spaced further apart than they would be in a standalone crystal of material.

Substrates were cleaned with aqua regia and piranha (3:1 mixture of sulfuric acid and hydrogen peroxide) before being annealed in an 800°C furnace for 6 hours to ensure the removal of any remaining organic material. A nucleated epitaxial layer of ZnO was achieved by suspending the substrate in a solution of 0.2g of zinc nitrate hexahydrate, 1.25mL of 15M ammonium hydroxide, and 24mL of deionized water. The sample was then heated in the microwave for 25 seconds which caused a fast increase in the temperature, up to approximately 100°C, and a supersaturation of the solution [74]. Small, tapered ZnO pillars on the order of 100nm in diameter and 100nm-200nm tall grew on the spinel as seen in Figure 3.3.

Growth of single crystalline ZnO into smooth, continuous films was achieved using a solution of 0.2g of zinc nitrate hexahydrate, 0.05 g of sodium citrate tribasic dehydrate, 1.25mL of 15M ammonium hydroxide, and 24mL of deionized water [65], [137], [138]. The

sample was suspended upside-down in the solution using a Teflon holder, to avoid unwanted precipitates landing on the growth surface of the ZnO, and placed in a 90°C oven for 18 hours. Following growth, the sample was removed from the solution, rinsed with deionized water, and dried with air.

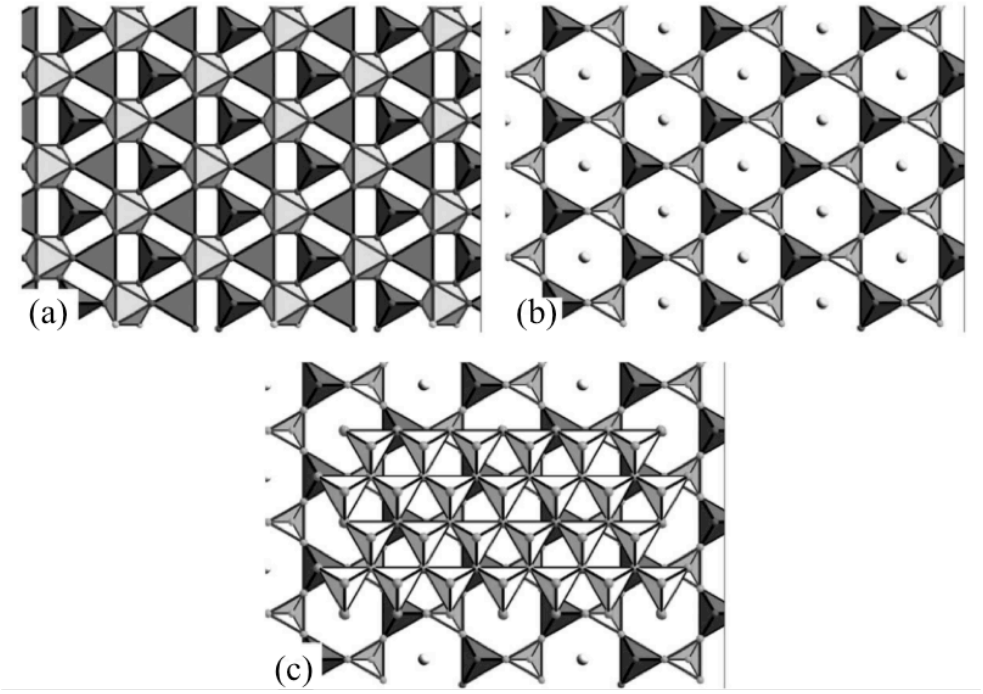

Figure 3.2: (a) Overview of the mixed cation layer of the spinel structure along the [1 1 1]. Darker polyhedrons represent Mg T+ (pointing out of the page) and Mg T- tetrahedrons (face triangles, pointing into the page). Lighter polyhedrons are the Al octahedrons, lying on their side. (b) Interfacial layer with two tetrahedral sites, represented as dark and light tetrahedrons, and two-fold proton sites, represented by light dots. (c) ZnO layer, represented as tetrahedrons, on top of the spinel and interfacial layers. Note that the ZnO has been scaled to a zero lattice mismatch for this illustration. Reprinted from [65], Copyright 2003, with permission from Elsevier.

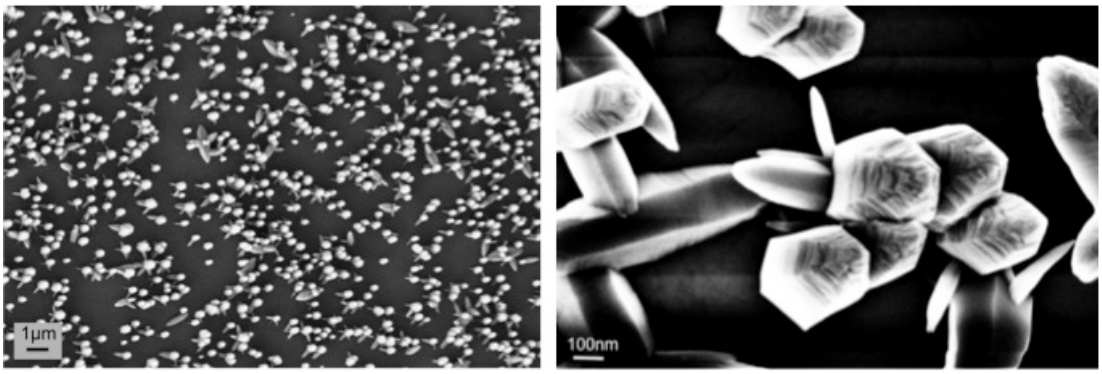

Figure 3.3: SEM images from the top-down of nucleated ZnO on spinel substrate achieved by microwave nucleation. Left image shows densely nucleated ZnO pillars. Right image shows details of individual tapered pillars.

3.5 Photoluminescence of Aqueously Grown ZnO

A thin film of ZnO on spinel grown as explained in Section 3.4 was illuminated with a 325nm laser using the LabRAM ARAMIS confocal system. The photoluminescence of the aqueously grown ZnO layer measured at room temperature is shown in Figure 3.4.

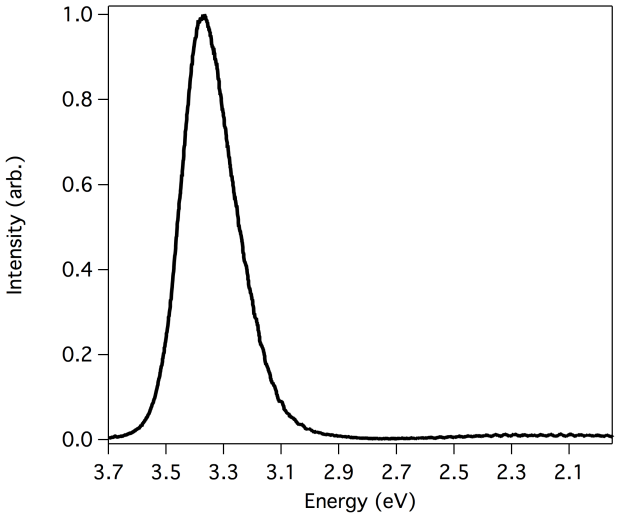

Figure 3.4: Photoluminescence spectra of aqueously grown thin film of ZnO measured at room temperature.

As expected a band edge peak and a green defect peak are observed. The green defect peak has a very low intensity compared to many of the ZnO samples measured in the literature; however, the intensity of this defect peak can vary based on the growth method [139]–[142]. The peak due to the bandgap transition, however, is located at a slightly higher energy than is usually reported in the literature [128]. One group that grew zinc oxide using an aqueous method also reported a slightly shifted UV peak which was attributed to effects of the water [108]. Upon fitting the band edge peak as explained in Section 3.3, it was realized that what was originally thought to be the band edge of the aqueously grown ZnO is in fact two overlapping peaks. It is believed that the higher energy transition is the bandgap and that the other transition is caused by defects due to the aqueous growth method of the zinc oxide. The fit is shown in Figure 3.5 where the black curve is the overall fit on top of the original spectra, the red curve is the higher energy peak with a mean energy of 3.39eV, and the green curve is the lower energy peak with a mean energy of 3.27eV.

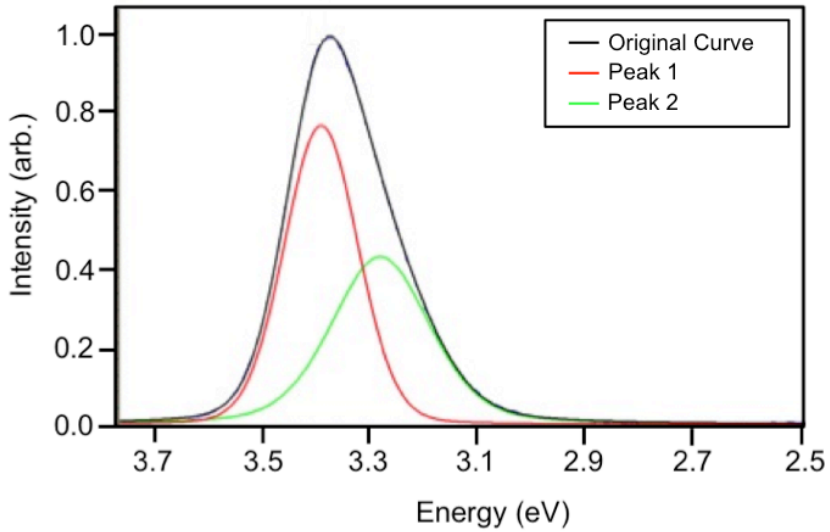

Figure 3.5: Photoluminescence spectra of aqueously grown ZnO at room temperature including Voigt fitting function.

To further optically investigate the aqueously grown ZnO, the sample was heated and subsequent photoluminescence measurements were made as shown in Figure 3.6. While many factors can cause shifts in both the bandgap transition and defect peaks measured using photoluminescence, varying the temperature often causes a dramatic change. A shift of the UV peak to lower energies with temperature is observed in the ZnO sample. As the temperature is increased, the vibration of the atoms in the material also increases leading to the expansion of the crystalline lattice. This expansion changes the length scale of the periodic potential and decreases the potential seen by the electrons in the material, thus leading to a smaller bandgap. The defect peak is also observed to shift with temperature due to the change in the energy between the defect level and the valance band.

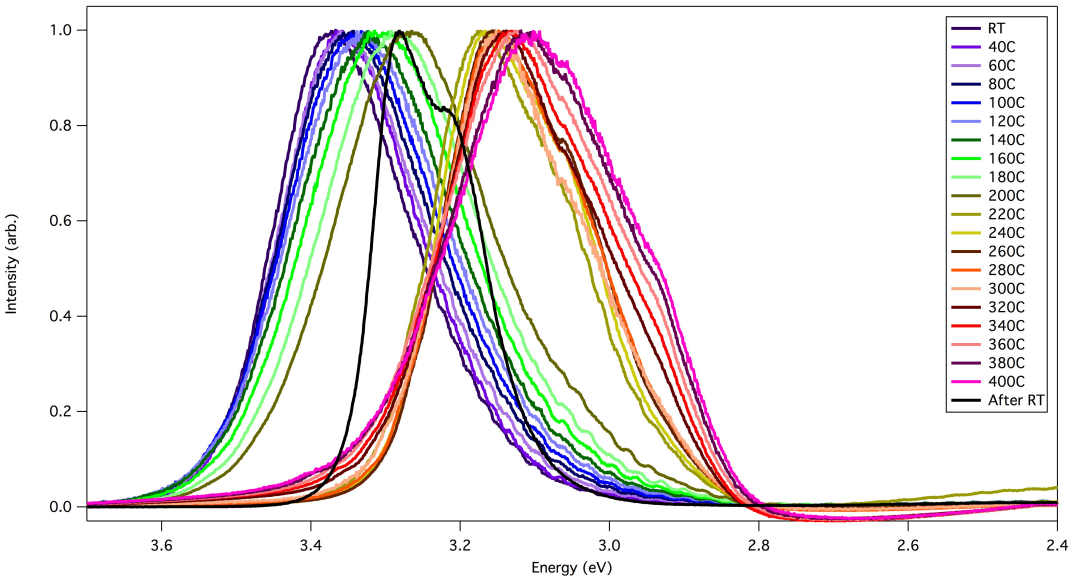

Figure 3.6: Photoluminescence spectra of aqueously grown ZnO at increasing temperatures.

By fitting the spectra taken at each temperature the two peak energies could be extracted. Both of the peak energies decreased with temperature as expected as shown in Figure 3.7(a); however, a jump in the peak energy of approximately 0.1eV is observed

between the 200°C and 220°C measurements. This abrupt 0.1eV jump in the peak energy suggests a dramatic phase change in the ZnO material. Indeed, a cracking of the ZnO film on the spinel is observed to occur between the 200°C and 220°C measurements. Additional samples of ZnO grown on spinel were also found to crack around the same temperature. Photoluminescence measurements made above 220°C were done on a flake of ZnO which had delaminated from the spinel substrate. It is believed that the initially grown ZnO was strained, and therefore as heating progressed the strain due to the ZnO growth and the difference in the thermal expansion coefficients of the materials caused the ZnO to crack. The thermal expansion coefficients of ZnO are $\Delta a/a = 4.7 \times 10^{-6}\ K^{-1}$ and $\Delta c/c = 2.9 \times 10^{-6}\ K^{-1}$ [143] while that of $MgAl_2O_4$ is $5.9 \times 10^{-6}\ K^{-1}$ [144].

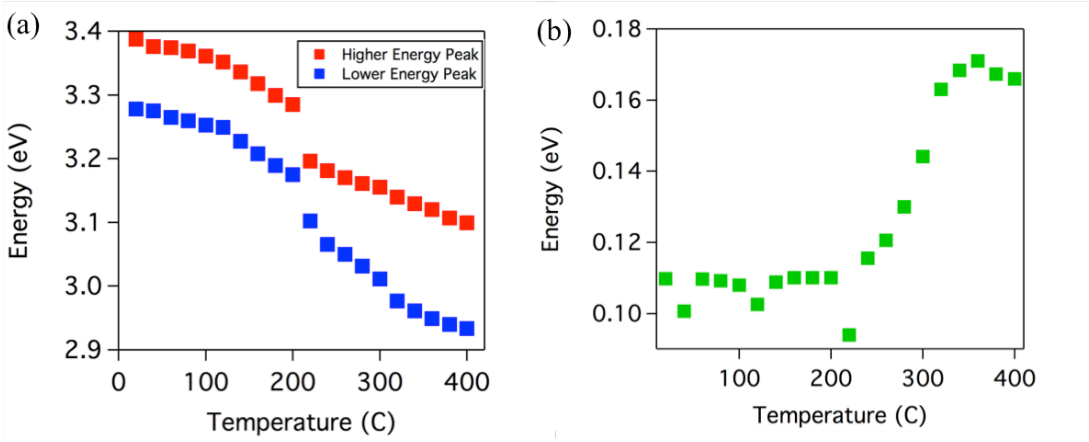

Figure 3.7: Fitting of photoluminescence spectra using Voigt fitting. (a) Peak energies versus temperature for initial heating of ZnO grown on spinel. (b) Energy splitting between the two peaks.

The splitting between the two fitting peaks was extracted and plotted versus temperature in Figure 3.7(b). At low temperatures, up to 200°C, the splitting stays constant at about 0.11eV. At higher temperatures however, a splitting of approximately 0.16eV is found. These values for the splitting between the two fitted peaks are consistent with Ozawa

et al.'s angle-resolved photoelectron spectroscopy measurements of the binding energy of the H-induced state [145]. As a H-induced state could be caused by the aqueous growth of the ZnO, it is plausible that one of our fitted peaks is indeed a shallow defect in the material. Further investigation is needed to confirm the exact type of defect in our ZnO.

Photoluminescence measurements made at room temperature after heating the aqueously grown ZnO sample to various high temperatures are shown in Figure 3.8(a). The measurements taken on samples heated above 200°C were done on flakes of ZnO as the initially grown film cracked. Samples were heated and then allowed to cool to room temperature before optical data was taken. For example, the After 100°C data was obtained by heating the ZnO sample from room temperature to 100°C, letting the sample sit at 100°C for several minutes, and then allowing the sample to cool back down to room temperature at which point photoluminescence data was taken. The room temperature and After 100°C heating curves are very similar; however, a significant change is evident in samples heated to higher temperatures. A ZnO sample heated to high temperatures (300°C to 700°C) not only clearly shows a UV peak made up of two separate peaks but also a measured UV peak at a lower energy than the room temperature (RT) and After 100°C measurements.

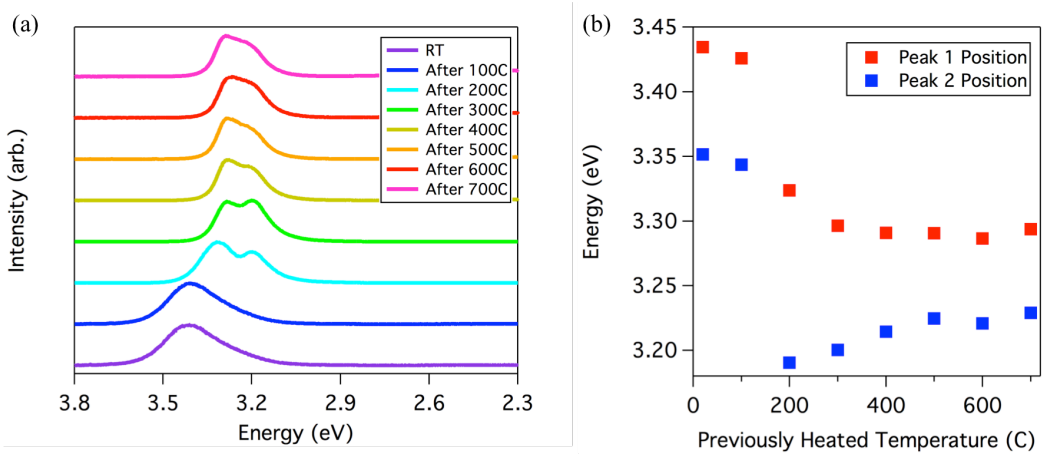

Figure 3.8: Photoluminescence of aqueously grown ZnO film taken at room temperature after being heated. (a) Individual spectra after each heating measurement of the ZnO. (b) Peak positions from fitting of each PL spectra.

The fitting of Voigt functions to the data shown in Figure 3.8(a) is plotted in Figure 3.8(b). A dramatic drop in the peak energies after the ZnO has been heated to temperatures above 200°C and then measured at room temperature is observed. This effect is irreversible and as it occurs with the cracking of the ZnO film it is likely to be caused by a change in the strain of the ZnO. The flakes of ZnO are likely to have much less strain than the initially grown film and possibly a better quality. In many strained materials there is an observed change in the bandgap. It is possible that the initial strain in the ZnO causes the bandgap to increase slightly as is observed in the fitted photoluminescence data. Once the strain is released due to cracking, the bandgap decreases as observed in Figure 3.8.

It is almost certain that there are defects in the ZnO material due to the aqueous growth method however; these defects would appear in the PL measurements below the bandgap of the material. The characteristic energy for defects is the energy from the defect/impurity state to either the conduction or the valance band. It is therefore likely that the lower energy peak is due to defects in the ZnO material. While the exact defects are

currently unknown it is believed that they are due to the aqueous growth method, as they have not been observed in optical studies of ZnO grown using other techniques.

Comparing the room temperature photoluminescence measurement of the ZnO before and after being heated to 700°C shows a large change as can be seen in Figure 3.9. This irreversible shift in the UV peak indicates a significant change in the material that is important to understand when designing optoelectronic devices. To further study the quality of the ZnO after being heated additional optical measurements were done on the flakes of ZnO.

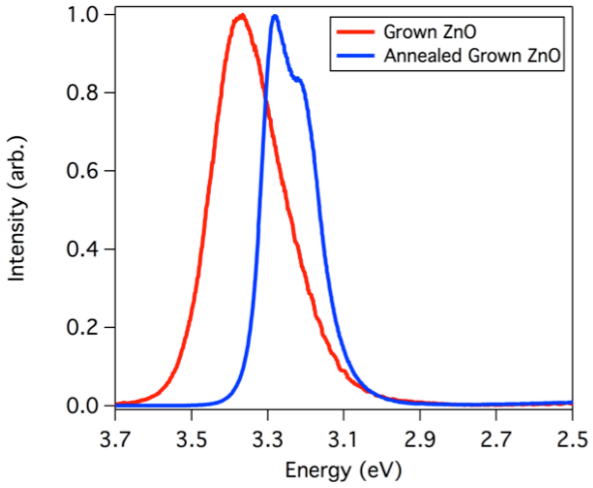

Figure 3.9: Comparison of PL of aqueously grown ZnO before and after being heated. All measurements taken at room temperature.

3.6 Photoluminescence of Aqueously Grown ZnO After Exposure to High Temperatures

With the knowledge that aqueously grown ZnO shows very different photoluminescence before and after being heated, further investigations into the effect of heating on ZnO were performed. A previously annealed ZnO sample was placed in the heating stage and the temperature slowly ramped up to 400°C. A measurement was taken every 20°C and the temperature was ramped by 10°C/min. The temperature was held constant for 5 minutes before each measurement was made. The spectra were again fit with the Voigt function in Section 3.3. Figure 3.10 shows the positions of the two fitting peaks versus temperature. For both peaks a linear relationship is observed with a slope of 5.2×10^{-4} eV/°C and 8.5×10^{-4} eV/°C. The splitting between the two peaks is plotted in Figure 3.11 and also shows a linear increase. In the measurements, the mean energy of the defect peak (lower energy peak) shifts more with temperature than the mean energy of bandgap transition (higher energy peak).

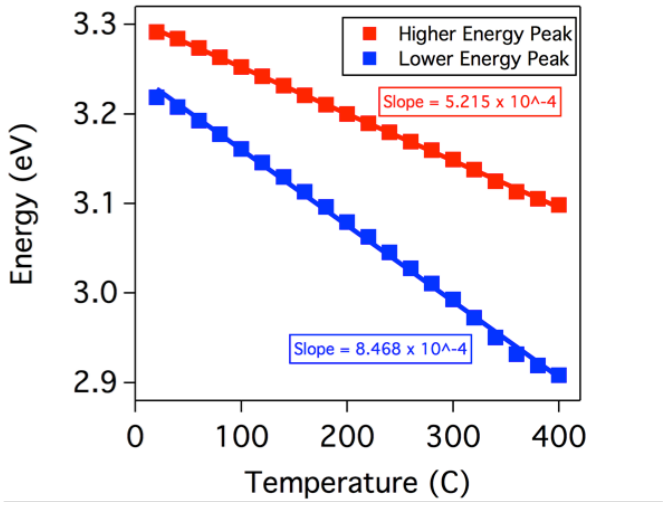

Figure 3.10: Peak position versus temperature determined using Voigt function for previously heated aqueously grown ZnO.

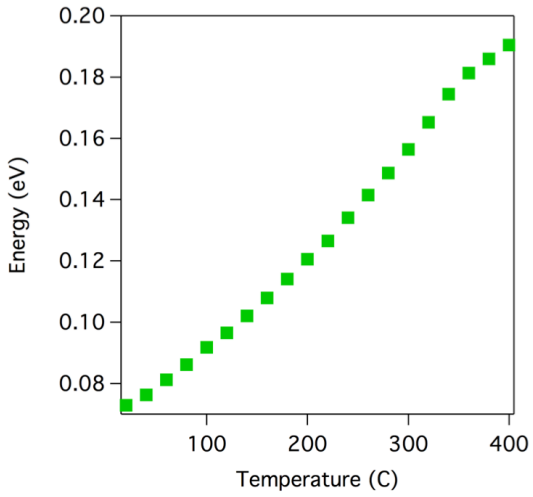

Figure 3.11: Splitting between two fitted peaks of aqueously grown ZnO after being exposed to high temperatures.

Repeating the annealing of the aqueously grown material additional times shows none of the effects seen during the initial heating of the sample. The optical measurements of the heated sample align very well with expected results. Therefore, we conclude that the initial heating of the ZnO causes an immediate and irreversible change in the material that is not noticed upon subsequent heating. The strain in the initially grown ZnO and difference in the thermal expansion coefficients of the ZnO and $MgAl_2O_4$ cause the ZnO to crack during the first heating cycle above 200°C. Subsequent optical measurements were made on the delaminated flakes of ZnO and no additional cracking of the ZnO was observed, which led to the expected linear trends in the optical data shown in Figure 3.10 and Figure 3.11. The fitted peak with the lower energy is associated with defects in the ZnO and is observed throughout the heating of the previously annealed sample.

The change in the strain of the ZnO can be calculated from the photoluminescence measurements. The difference in the higher energy peak of the as grown ZnO and the annealed ZnO is found to be 0.096eV. Using the slope (5.215×10^{-4} eV/°C) from the energy

versus temperature plot in Figure 3.10 for the annealed ZnO sample and the ZnO thermal expansion coefficient perpendicular to the c-axis (4.7×10^{-6} K^{-1}) [143], the change in strain between the aqueously grown ZnO and the annealed ZnO is calculated to be 8.75×10^{-4}.

3.7 Photoluminescence of Commercial ZnO

Commercial single crystalline ZnO was purchased and optically measured to use as a comparison for the aqueously grown material. Room temperature PL was first taken on the commercial sample as shown in Figure 3.12 and compared with the aqueously grown ZnO. The bandgap peak position is approximately 3.3eV and the width of the peak is significantly smaller than that of the aqueously grown ZnO both before and after the application of high temperatures. The fitting function from Section 3.3 was again used and the commercial ZnO photoluminescence also appeared to consist of two peaks. The splitting between the two peaks was much smaller for the commercial ZnO than for the aqueously grown samples. The commercial ZnO is grown hydrothermally and from optical measurements a much larger green defect band luminescence is observed. In addition, the annealed aqueously grown ZnO more closely resembles the commercial material than the originally grown ZnO.

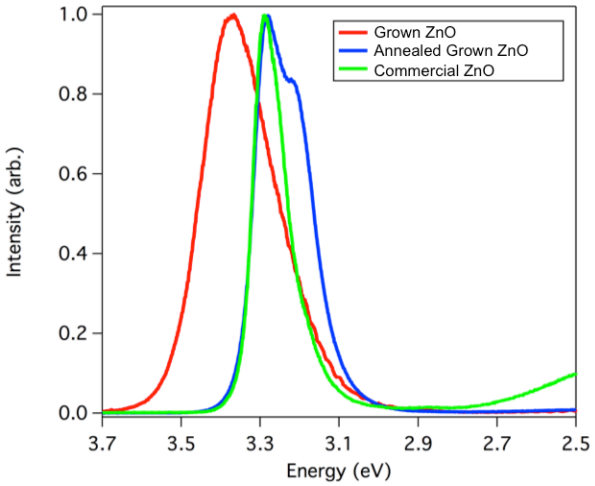

Figure 3.12: Comparison of photoluminescence of aqueously grown ZnO, annealed aqueously grown ZnO, and commercial ZnO. All spectra taken at room temperature.

Heating measurements were performed on the commercial material as shown in Figure 3.13. A redshift of the UV photoluminescence peak is observed, as is a broadening of the peak with increasing temperatures. Figure 3.14 shows the peak positions versus temperature for the commercial sample. A slope of approximately 5.0 x 10^{-4} eV/°C for both of the peaks is calculated and closely matches those for the annealed aqueously grown ZnO. As mentioned earlier, the splitting between the two peaks for the commercial sample is very small, however, the material was grown using a different technique than the aqueously grown ZnO samples. In addition, the splitting between the two peaks remains fairly constant with increasing temperature, which was not the case for the annealed aqueously grown material. While the exact source of the second peak in the UV portion of the commercial ZnO's photoluminescence has not been confirmed, it is believed that it is again due to a defect in the material.

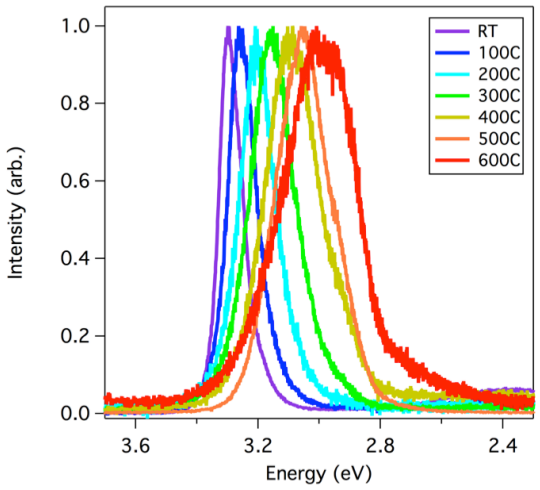

Figure 3.13: PL spectra of commercial ZnO at various temperatures.

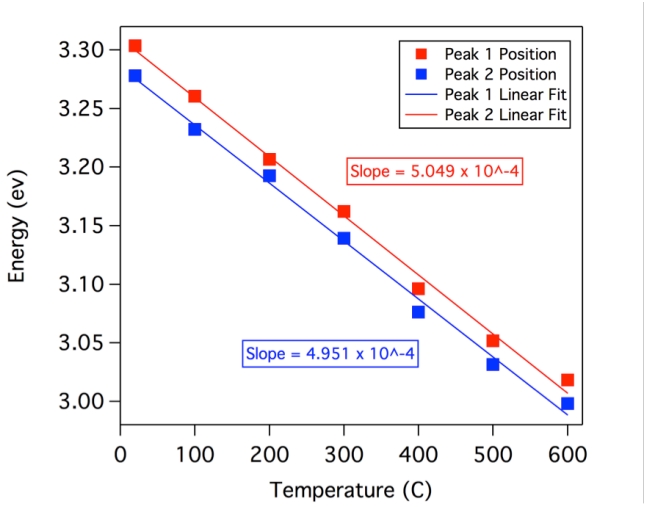

Figure 3.14: Photoluminescence peak position versus temperature for commercial ZnO.

After taking the photoluminescence measurement at each desired temperature, the PL of the ZnO at room temperature was measured as shown in Figure 3.15. Unlike the original aqueously grown ZnO, the commercial ZnO has approximately the same mean peak energy values regardless of the previous temperature the sample is heated to. No cracking in the commercially purchased ZnO crystal was observed with heating and, therefore similar room

temperature photoluminescence measurements taken after being heated to different temperatures are expected.

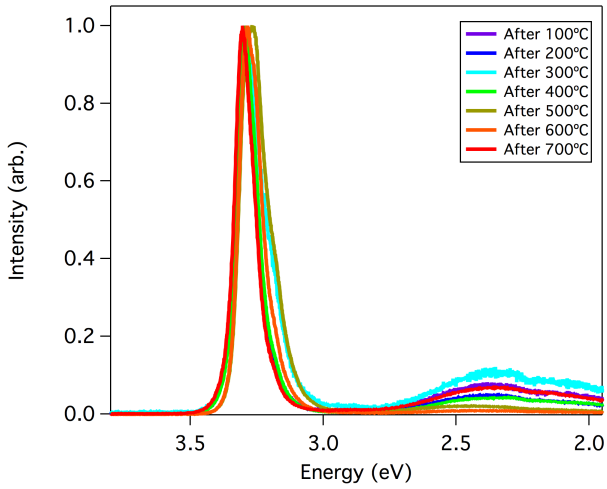

Figure 3.15: PL spectra of commercial ZnO taken at room temperature after being exposed to high temperatures.

3.8 Persistent Photoconductivity Measurements on ZnO Samples

As the name suggests, persistent photoconductivity is the presence of a photocurrent in a material long after it has been exposed to, in our case, UV excitation. Persistent photoconductivity has been measured in many types of semiconductor materials and devices including zinc oxide [146]–[148]. The presence of persistent photoconductivity is important to understand as it can drastically alter the performance of a device even after excitation is applied. Many of the reports in ZnO systems to date have cited persistent photoconductivity as an issue related to defects in the material, but the absolute cause is still in question [148], [149]. Several reports have investigated the role that the amount of oxygen adsorbed onto the surface plays, while another believes it involves the bistability of substitutional hydrogen

at oxygen sites [149], [150]. Regardless of the exact cause, the lack of decay over time of the photoresponse in a material is import to identify and can lead to further information about the material being measured.

One way to optically measure if the three samples under investigation (aqueously grown, annealed aqueously grown, and commercial) have persistent photoconductivity is to compare the photoluminescence of the samples before and after being exposed to the full power of the 325nm laser (~5mW) for 2 seconds. In the case of the aqueously grown ZnO, shown in Figure 3.16, the intensity of the initial photoluminescence signal is significantly less than the photoluminescence intensity after the sample was exposed to the full intensity of the laser. This large increase in the intensity is attributed to persistent photoconductivity. When the ZnO is exposed to the ~5mW UV laser, many of the carriers may become stuck in various defects and traps in the material as shown in Figure 3.17. Therefore, when the second photoluminescence curve is taken, a significantly larger proportion of the traps are filled. With the traps now full, a greater number of electrons and holes produced by the photoluminescence excitation recombine, leading to the higher spectra intensity.

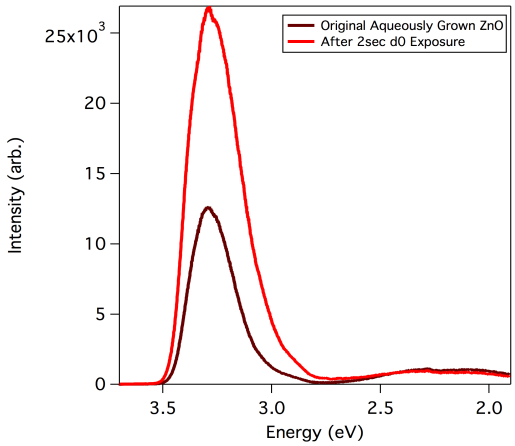

Figure 3.16: Comparison of aqueously grown ZnO photoluminescence before and after being exposed to full laser power (~5 mW) for 2 seconds.

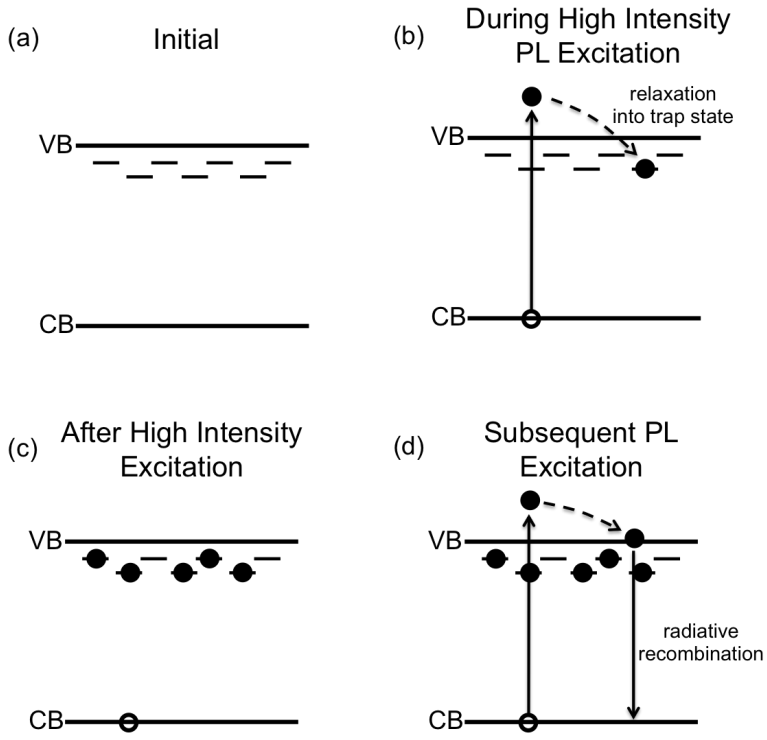

Figure 3.17: (a) Energy level diagram showing conduction band, valance band, and defect states. (b) During above band excitation electrons are promoted from the conduction band into the valance band. When they relax the electrons can become trapped in the defect states. (c) Following high intensity excitation the defect states are highly populated. (d) Upon subsequent PL excitation carriers are once again promoted across the bandgap however, now they have a much smaller probability of becoming trapped in defects due to the existing electron population within the traps. This causes a higher proportion of the photo-excited carriers to radiatively recombine with holes in the valance band.

After exposing the aqueously grown ZnO to the full laser power, the intensity of the photoluminescence after certain amounts of time was measured as shown in Figure 3.18. The photoluminescence curves slowly decrease over time; however, even after almost a day, the measured intensity is still above that of the before exposed material. This means that there may be some very long-lived traps in the material that cause the persistent photoconductivity to last for a significant amount of time. The presence of persistent conductivity over long periods of time in ZnO has been previously reported in the literature

[148]. The effect on the material of additional 2-second full power laser exposures as shown in Figure 3.18 was also investigated. Subsequent exposures of the ZnO continued to result in increases in the intensity of the photoluminescence. The additional increases in the intensity were observed to be much smaller than the initial effect shown in Figure 3.16. While many of the traps were filled during the initial 5mW UV laser exposure, additional traps may become filled upon subsequent optical exposures.

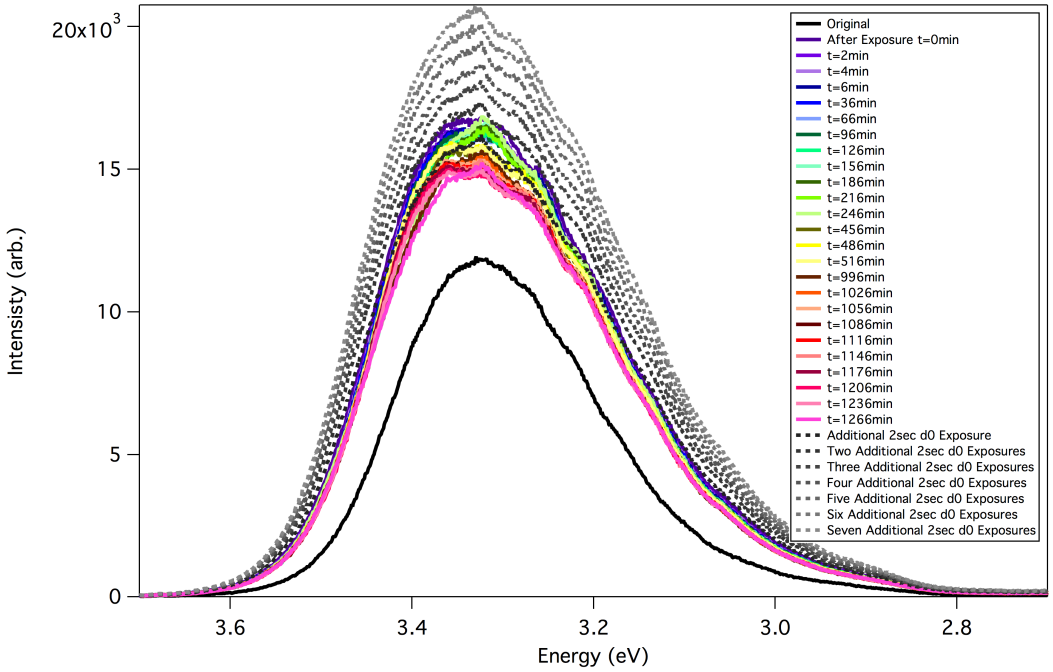

Figure 3.18: Decay of PL from aqueously grown ZnO over time. In addition, PL spectra from additional full power laser exposures on the ZnO.

Similar photoluminescence data were taken on the annealed aqueously grown and commercial ZnO samples as shown in Figure 3.19 and Figure 3.20. In the case of the annealed aqueously grown ZnO sample, the initial PL spectra and the after full laser power exposure spectra taken were the same. For the commercial ZnO sample, the initial photoluminescence spectra was slightly higher than the after full laser power exposure.

Compared to the change observed in the aqueously grown ZnO, the difference measured for the commercial sample was very small.

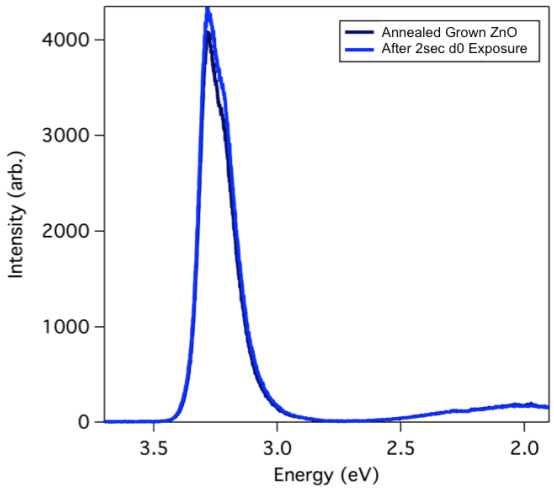

Figure 3.19: Comparison of the annealed aqueously grown ZnO before and after being exposed to full laser power (~5 mW) for 2 seconds.

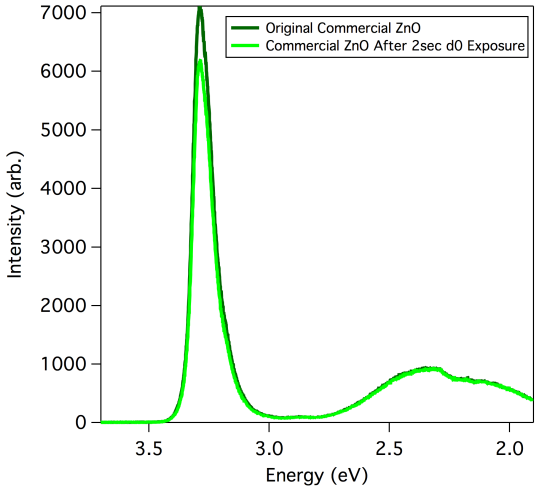

Figure 3.20: Comparison of commercial ZnO photoluminescence before and after being exposed to full laser power (~5 mW) for 2 seconds.

Overall, further optical measurements on the three ZnO samples in which they were exposed to a high intensity UV laser beam resulted in very different photoluminescence

curves. The aqueously grown ZnO showed a persistent photoconductivity that upon further investigation appears to decay over a matter of days. The photoluminescence intensity could be further increased by additional high power UV laser exposures. In contrast, the annealed ZnO and the commercially purchased material did not show a persistent photoconductivity. These experiments further indicate the presence of defects in the aqueously grown material that appear to not be present after it is annealed. In addition, the annealed ZnO and commercial material show very similar optical responses to the high power UV laser exposure.

3.9 Comparisons and Summary of ZnO Photoluminescence

Putting together all of the optical measurements performed on the ZnO samples one can see that the commercial ZnO and the annealed aqueously grown ZnO show the most similarities. Comparing the behavior of each of the samples during the temperature dependent measurements as shown in Figure 3.21, it becomes apparent that the commercial ZnO and Peak 1, the higher energy peak, of the annealed aqueously grown ZnO show very similar behaviors over a wide temperature range. Therefore, it can be concluded that Peak 1 for the annealed sample is due to the bandgap transition and that Peak 2 is due to shallow donor defect inclusions from the aqueous growth. For the aqueously grown ZnO sample, initially there is a peak higher than the expected bandgap energy, which is believed to be the bandgap energy slightly shifted due to the strain in the ZnO (Peak 1 up to 200°C). Once heating of the sample above 200°C occurs this higher energy peak shifts to the expected ZnO bandgap at the given temperatures, as can be seen in Figure 3.21. This jump in the bandgap occurs when the ZnO film delaminates from the substrate and cracks. In doing so it is

believed that the strain is reduced and that the flakes of ZnO are higher quality. Above 200°C the higher energy peak, Peak 1, for the aqueously grown and annealed samples are comparable at the full range of temperatures measured. The lower energy peak, Peak 2, for the aqueously grown ZnO is attributed to shallow donor defects in the material due to the aqueous growth. This photoluminescence peak also shows a sudden jump in energy with the cracking of the ZnO film and closely matches the calculated peak energies for the lower energy peak, Peak 2, of the annealed ZnO. Optical measurements made at room temperature following heating, shown in Figure 3.22, confirm that Peak 1 of the aqueously grown ZnO is most likely the bandgap transition in the material. Once the cracking of the ZnO occurs the higher energy peak, Peak 1, of the aqueously grown ZnO closely matches the energies for Peak 1 of the commercial ZnO sample.

Lastly, persistent photoconductivity is measured in the initially grown ZnO, which is no longer observed once high temperature heating is performed. The presence of persistent photoconductivity along with the change in the photoluminescence in the aqueously grown ZnO upon heating lead to the belief that additional defects and strain are introduced into the material due to the growth method. Heating of the ZnO can however, remove some of the effects and produce an optical signal more similar to commercially purchased zinc oxide. It may be possible to engineer a growth pattern for the ZnO on the spinel substrates that reduces the amount of strain present and avoids the cracking of the ZnO film. Regardless, the ability to aqueously grow high quality ZnO is a promising step towards the development of wide bandgap photonic devices fabricated using a bottom-up, low temperature growth technique. The advantage of this method is that it allows single crystalline layers to be easily

grown and has the potential for creating complex photonic device structures via lithographic patterning of the substrate.

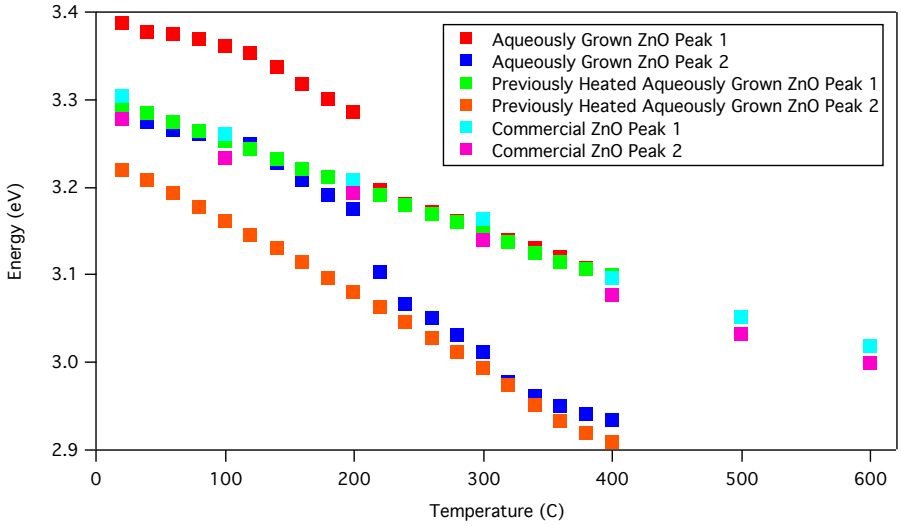

Figure 3.21: Fitted peak positions for the three different ZnO samples during heating measurements.

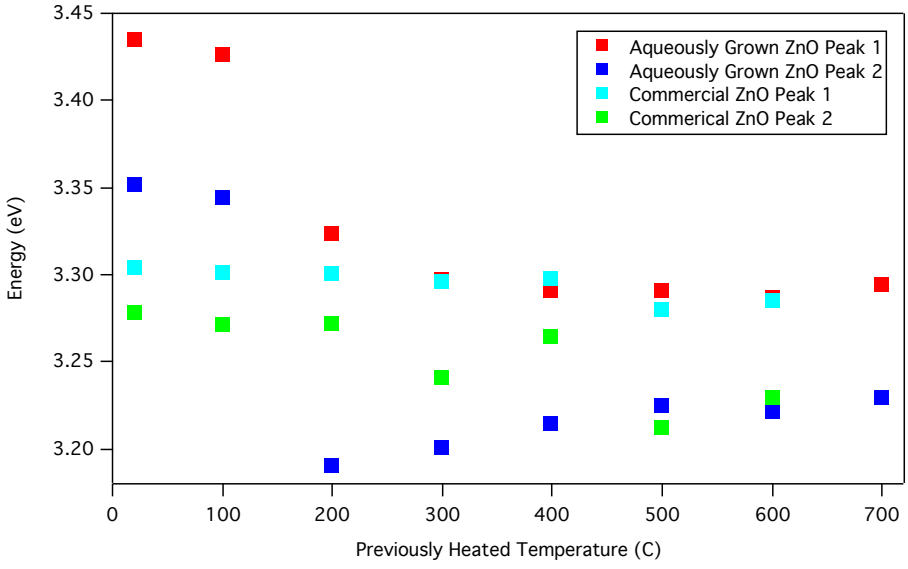

Figure 3.22: Fitted peak positions for aqueously grown and commercial ZnO after being heated. All measurements taken at room temperature.

Chapter 4

Constrained, Aqueous Growth of Zinc Oxide Structures

4.1 Introduction and Motivation

Selective growth of semiconductor materials through pre-patterned masking layers can provide important advantages for the definition and performance of the final structures. Such an approach can control the placement of arrays of microstructures or nano-structures [44], [75], [77], [151], [152]. In addition to simplification of the fabrication process, one of the main advantages of selective growth in terms of device fabrication is that it could result in structures with crystallographically smooth sidewalls without the challenges of degradation brought about by an etch process [48]–[51]. In many cases, patterned, epitaxial growth of high quality semiconductor materials occurs only at high temperatures (typically >500°C) [153], [154]. At these temperatures masking the desired regions of the sample and control of the growth process can be difficult. In this chapter, experiments are performed that explore the selective growth of singe crystal zinc oxide (ZnO), formed through a low temperature, aqueous process. The growth is directed by nanometer-scale and micron-scale pre-patterned "molds" formed of photoresist or electron-beam resist. The effects of the mask

material on the constrained growth, size and shape of the pre-patterned opening, as well as the orientation of the mask with respect to the underlying crystalline structure are investigated. The structures fabricated demonstrate the ability to easily control the final 3D shape of the grown ZnO simply by controlling the growth duration and strategically choosing the size, shape, and orientation of the masking material.

4.2 Sample Preparation

ZnO is a transparent, wide bandgap (~3.3eV) semiconductor, with a predominant hexagonal wurtzite crystalline structure at ambient conditions [14], [15], [24]. A variety of techniques have been employed to form ZnO as discussed in Chapter 2 [24], [155], [156]. The approach used here incorporates a solution-based growth in zinc nitrate hexahydrate, ammonium hydroxide, sodium citrate, and deionized water, the details of which can be found in Chapter 2.4 [65], [129], [137], [138]. The fabrication process steps are outlined in Figure 4.1.

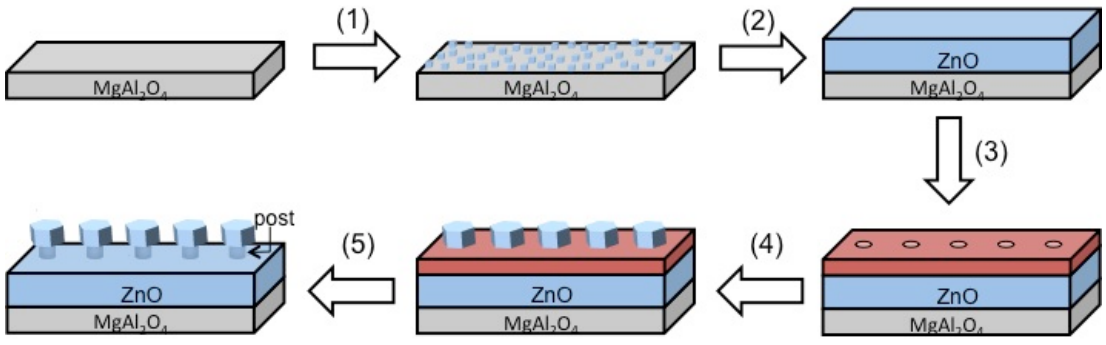

Figure 4.1: Overall fabrication process of aqueously grown ZnO structures on spinel ($MgAl_2O_4$). (1) Nucleation of ZnO on $MgAl_2O_4$ substrate in the microwave. (2) Overnight growth of ZnO in 90°C oven. (3) Photolithography or e-beam lithography patterning and subsequent developing of resist. (4) Growth in 90°C oven for desired amount of time. (5) Resist removal.

A seed layer was first formed on the lattice matched (111) $MgAl_2O_4$ spinel substrates under microwave treatment. Samples were then placed in a 90°C oven overnight to form a smooth and continuous base layer. The base layer was lithographically patterned with either photoresist or e-beam resist, resulting in polymer "molds" of different shapes and orientations. Following the making of the mold, the sample was again put in the growth solution containing sodium citrate, to limit the growth in the vertical (0001) direction, and placed in the 90°C conventional oven for the desired amount of time. Typical growth times for the structures presented in this chapter ranged from 2 hours to 4 hours, producing a range of structure sizes with heights up to approximately 7μm depending on the growth solution. Following all growth steps, the resist was removed from the sample by placing the sample in PG Remover on a 100°C hotplate for 5-10 minutes.

4.3 Experimental Techniques

Photolithography was performed using a Suss MJB4 Mask Aligner. Shipley 1811 and 1813 photoresists were spun onto the samples for 45 seconds at either 4000rpm or 5000rpm resulting in resist thicknesses between 1μm and 1.5μm. Samples were placed on a 115°C hotplate for 1 minute immediately following the spin coating of the resist. Masks with various thicknesses of lines and sizes of circles were used for the lithography process. Hard contact mode was found to produce the straightest sidewalls and was therefore the most utilized contact mode. Samples were developed in CD-26 developer for 1 minute and then thoroughly rinsed with water for 1 minute before being dried with nitrogen.

Electron beam (E-beam) lithography was done on an Elionix ELS-F125 system. Appropriate doses and exposure times were determined to provide the best resolution for the

pattern being written. Polymethylmethacrylate (PMMA) was used as the resist for e-beam written molds. PMMA was spin-coated onto the ZnO base layers at 4000rpm for 45 seconds. The samples were then baked on a 180°C hotplate for 3 minutes. The ZnO is non-conducting, and therefore to produce a conductive sample, as is need to ensure the best results when using the e-beam lithography system, a 10nm layer of gold was spin coated onto the samples. Following the e-beam write, the gold was removed from the sample using a wet gold etch for 20 seconds and then rinsed with water. The samples were developed in 1:3 MIBK:IPA for 1 minute and then placed in IPA for 1 minute.

Scanning electron microscopy (SEM) images of the fabricated structures were obtained using the FESEM Ultra55 or FESEM Supra55VP. A 5keV electron beam was used for imaging the ZnO samples. Both systems are equipped with a titling stage, which allows for more in depth surface examination of the sides of fabricated structures. For samples where charging was a particular problem, 5nm of gold was sputtered onto the surface of the samples.

The crystallographic orientations of the ZnO were measured using electron backscatter diffraction (EBSD) on the FESEM Supra55VP. In addition to investigating the crystal orientation of the material, EBSD allows for the measurement of the misorientation, grain size, phase identification, etc.. A 20keV electron beam hits the sample and diffracted electrons are measured on a phosphor screen. A CCD camera is used to view the diffraction pattern produced on the screen. These diffraction patterns are used to determine the crystalline orientation along with other material properties.

4.4 Structures Formed Using Photolithography Masks

Using resist as a mold for the growth of ZnO allows for the possibility to create numerous sizes and shapes of structures. Photolithography was initially used to create the mask layers due to the ease of fabrication. Figure 4.2 shows a cross-section of ZnO growth along the patterned lines of photoresist. The ZnO exactly follows the shape of the photoresist, which shows that using resist as a mold during ZnO growth is a viable option.

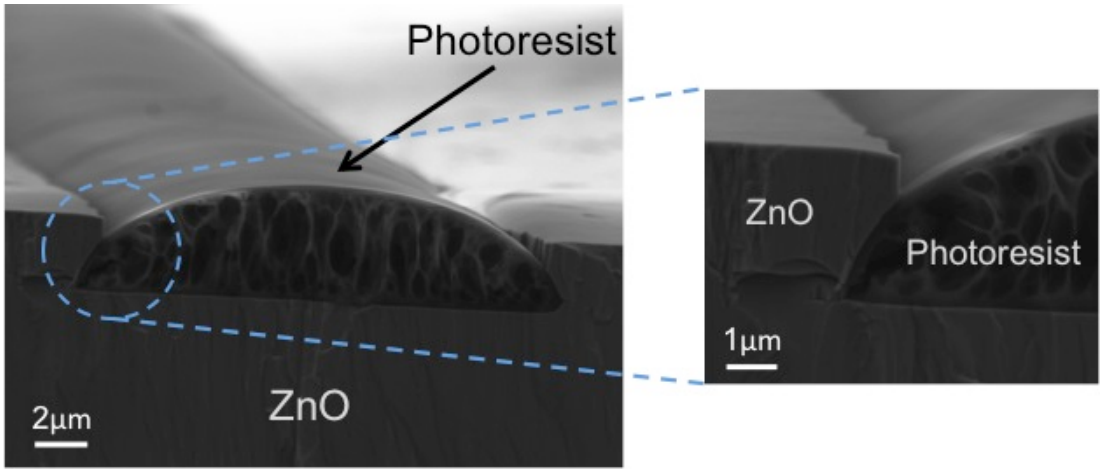

Figure 4.2: ZnO aqueous growth exactly following the shape of the photoresist pattern.

One of the advantages of bottom-up growth is the ability to vary conditions such as the growth time and create structures of different sizes and shapes. Figure 4.3 shows ZnO structures grown for different amounts of time through circular holes in the photoresist. During the growth, the ZnO initially grows in the constrained region of the mold. Once the mold region is filled, the ZnO overgrows the resist and grows unconstrained, eventually leading to hexagonal structures due to the crystalline structure of zinc oxide.

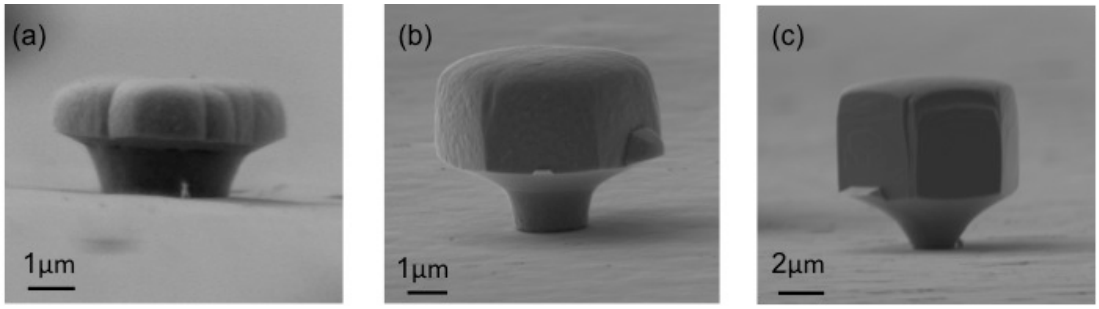

Figure 4.3: ZnO structures grown through holes patterned in photoresist grown for a) 2.25 hours, b) 3 hours, and c) 4 hours.

In Figure 4.3 the post regions of the ZnO structures are tapered due to the slope in the photoresist mold caused by the photolithography processing. The ZnO structure grown for 2.25 hours (Figure 4.3(a)) overgrows the post region. Rounded edges of the overgrown material are observed, as it has not grown for long enough to produce the hexagonal facets that are often found with ZnO structures. The structures grown for 3 hours and 4 hours (Figure 4.3(b) and Figure 4.3(c)) have grown for long enough where smooth, hexagonal ZnO structures are fabricated. The amount of growth in both the vertical (0001) direction and the $(10\bar{1}0)$ direction of the ZnO after it reaches the top of the mold were measured and are shown in Table 4.1.

	2.25 Hours	**3 Hours**	**4 Hours**
Overgrown ZnO Height	~1μm	~2.7μm	~4μm
Overgrown ZnO Diameter	~2.5μm	~7μm	~10μm

Table 4.1: Amount of ZnO growth above the circular mold openings for different growth times.

Another advantage of the aqueous growth method is the ability to stop growth at a desired point and be able to continue the growth process at a later time with no observed

effect. Figure 4.4 shows a ZnO structure grown through a photolithographically defined hole. The sample was grown for 4 hours in the growth solution, removed from the solution, and placed in a new growth solution where it was again grown for four hours four different times. The SEM image shows extremely smooth, hexagonal sidewalls for the overgrown ZnO material and no indication that the growth was interrupted numerous times. The ability to stop growth and replenish the growth solution, as the constituents are used up during the growth, allows for the growth of very tall ZnO structures with large aspect ratios. Such structures would be difficult to fabricate using top-down fabrication techniques.

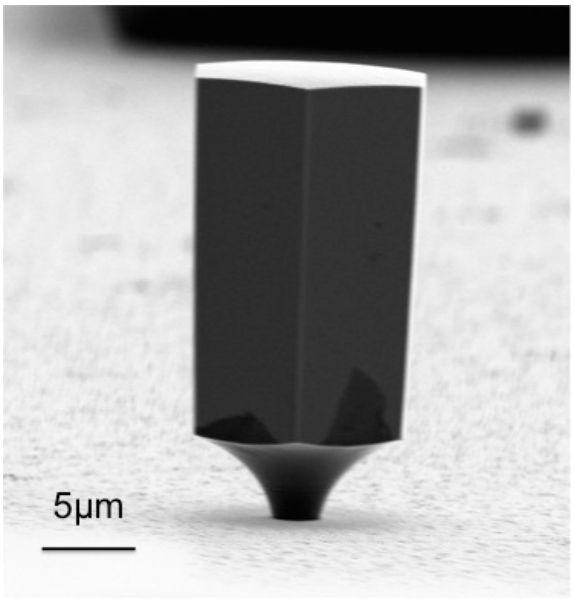

Figure 4.4: Single crystalline ZnO structure grown through a photoresist mold. The growth was stopped 3 times to exchange the growth solution and replenish the solution constituents.

4.5 Structures Formed Using Electron Beam Lithography Defined Masks

The resist masks fabricated using photolithography had significant tapered sidewalls as shown in the previous section. For many applications where undercut structures could prove to be advantageous, vertical profiles in the resist are required to obtain well-defined undercuts in the material. To achieve such structures electron beam lithography was used rather than photolithography. Initial experiments utilized four different diameter circular molds (2μm, 1μm, 0.50μm, and 0.20μm) formed of approximately 500nm thick patterned PMMA. ZnO was grown for 4 hours, with an 8M zinc nitrate growth solution. The final structures are shown in Figure 4.5. For all of the grown structures the ZnO fully fills the circular molds and assumes the shape of the post region. The final height of the hexagonal structures grown through all four patterned diameter sizes was found to be the same (3.6 ± 0.1μm), unaltered by the size of the hole opening. Therefore, the growth rate in the (0001) direction dominates the ZnO growth. Once the growth reached the top of the mold and is laterally unconstrained, the "natural" hexagonal symmetry of the ZnO structures emerges and the sidewalls of the overgrown region become smooth with crystallographically-defined m-plane facets as was observed in the structures grown through photoresist molds.

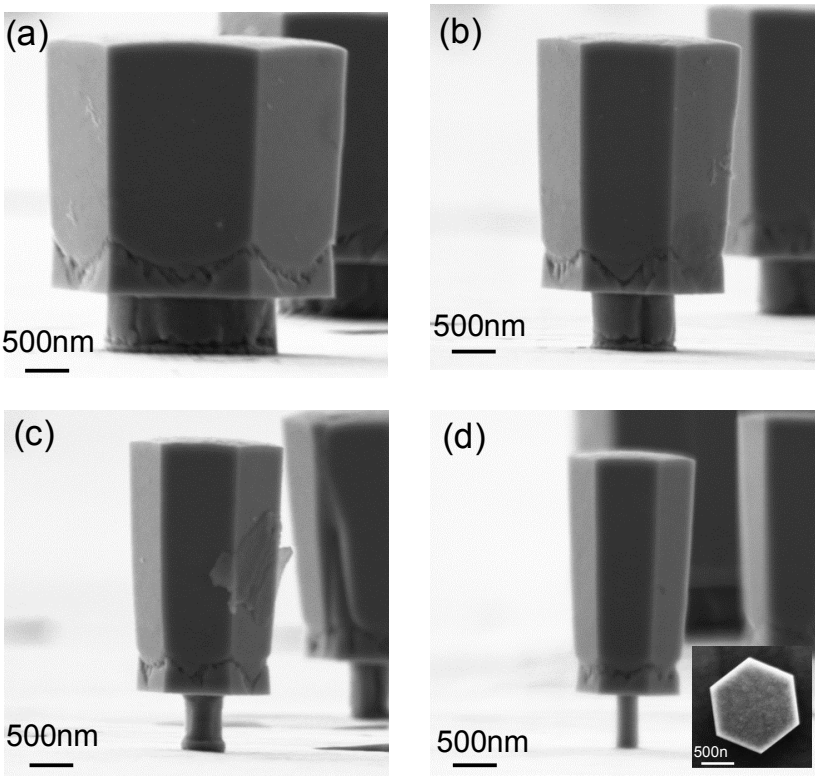

Figure 4.5: SEM micrographs of ZnO grown in an 8M zinc nitrate solution for 4 hours through a) 2μm, b) 1μm, c) 0.50μm, and d) 0.20μm diameter circular holes. Insert in d) shows a top-down view of the ZnO structure with the scale bar equal to 500nm.

Figure 4.6 shows that a linear dependence between the hole opening and the final structure diameter is observed. Regardless of the diameter of the post, the lateral overgrowth of the structure is 0.55 ± 0.04μm. This indicates a lateral growth rate independent of the mold size and shape, which is determined by the rate of the growth perpendicular to each (slow-growing) m-plane facet. Therefore, it can be concluded that the ZnO growth is determined by the c-plane growth in the vertical direction and by the m-plane growth in the lateral direction.

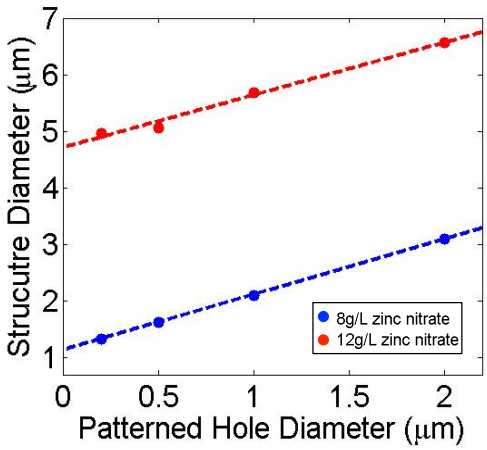

Figure 4.6: Comparison of the size of ZnO structures grown through patterned circular openings with both 8M (blue) and 12M (red) zinc nitrate growth solutions.

The exact growth rate of the various ZnO crystalline planes is non-trivial to calculate due to the fact that the rate is nonlinear. The patterned samples require some time to come to thermal equilibrium with the 90°C oven temperature. Growth will occur when the increased temperature results in the decreased solubility of the ZnO solution [74]. Preliminary experiments established that the ZnO growth begins approximately 2 hours after the sample is placed in the oven. If we assume a subsequent constant growth rate, the vertical (0001) c-axis growth rate of the ZnO is calculated to be ~30 nm/min. In addition, using the same assumptions and taking into account the time required to grow to the top of the patterned mold, the growth rate of the $(10\bar{1}0)$ m-planes is found to be ~6 nm/min. These two rates may be separately controlled by changing the concentration of the zinc nitrate and/or the sodium citrate in the growth solution. For the same growth time, changing the concentration of the zinc nitrate in the growth solution to 12M resulted in an increased height of the structures to 6.8 ± 0.30μm and an additional lateral epitaxial overgrowth to 2.32 ± 0.05μm for all four hole openings. This corresponds to growth rates in the vertical and lateral

directions of ~57 nm/min and ~21 nm/min, respectively. The linear relationship between the patterned hole diameter and the final structure diameter for the higher concentration solution is shown in red in Figure 4.6.

The shapes of the mold were then altered and the geometry of the resulting structures was investigated. Several different shapes (circle, hexagon, triangle, and square) each with a lateral dimension *d* of 3μm as shown in Figure 4.7 were patterned in the approximately 500nm thick PMMA to create molds for the ZnO growth.

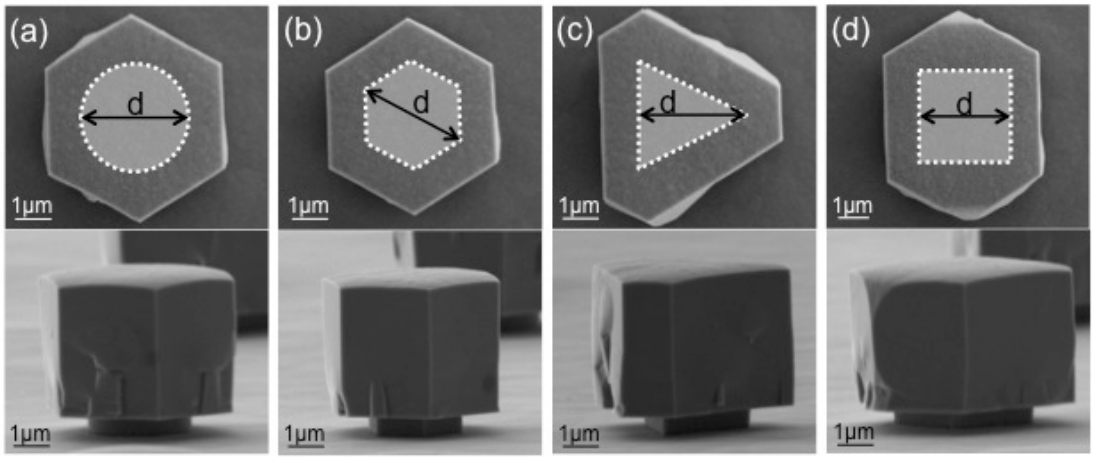

Figure 4.7: Scanning electron microscopy images taken perpendicularly to the substrate (upper images) and at a tilt of 6.5° from the substrate (lower images) of the resulting ZnO structures after 4 hours of growth in a 90°C oven with initially patterned (a) circle, (b) hexagon, (c) triangle, and (d) square. Outlined shaded region indicates the e-beam lithography patterned post and d = 3μm.

The upper and lower SEM images in Figure 4.7 show the resulting structures after 4 hours of growth, imaged perpendicularly to the plane of the substrate and at a 6.5° angle from the substrate, respectively. The bottom part of the ZnO structure (post region), which is visible in the lower SEM images in Figure 4.7, again exactly fills the mold that was patterned. Similar to the results obtained for the circular molds, once the thickness of the ZnO exceeds

the height of the mask layer the growth is no longer constrained in the lateral direction, and the natural hexagonal symmetry of the structures emerges.

The clear hexagonal symmetry of the ZnO structure suggests that there is a defined crystallographic orientation in the material that guides the growth of the structures, perhaps present in the base layer. Such an orientation was confirmed by electron backscatter diffraction (EBSD) measurements, seen in the combined image quality (IQ) and inverse pole figure (IPF) in Figure 4.8(a). The colors in the figure indicate the collective quality [157] of the electron backscatter diffraction pattern together with the crystal orientations of the material. The m-planes in the ZnO are indicated by yellow lines. Given the crystallographic orientation of the base layer, it is important to consider the effect of the orientation of the mold geometry relative to the base layer. These data are shown in Figure 4.8(d): 3μm triangular openings were patterned in the PMMA with each successive pattern rotated by 10°. The scanning electron microscope images of the resulting structures after 3.5 hours of growth show the shape of the overgrown material relative to the orientation of the original mold pattern. Deviations of the mold orientation from that of the ZnO base layer's crystalline structure result in growth of less regular geometrical shapes in the xy-plane. These structures can be seen as intermediary shapes, before the overall structures become hexagonal. When the edges of the patterned opening align with the $(10\bar{1}0)$ m-planes of the ZnO, very smooth and vertical sidewalls are observed. The ability to easily form extremely smooth sidewalls is particularly important for optical devices to minimize scattering loss. These experiments suggest that smooth sidewalls can be obtained, even for non-hexagonal structures and molds, through the judicious orientation of the mold pattern to the base layer.

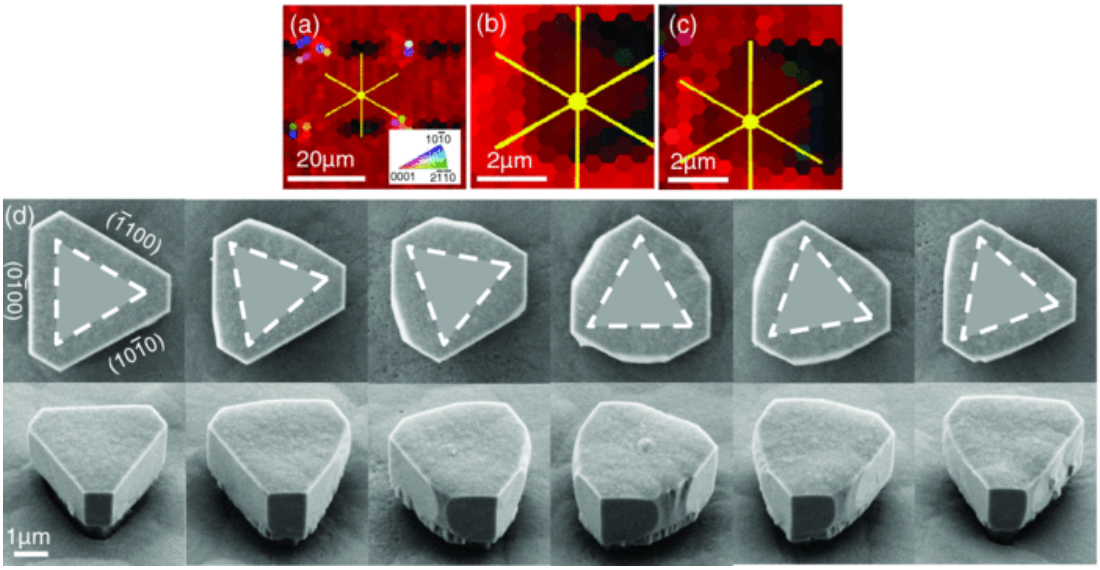

Figure 4.8: Successive rotation of e-beam lithography patterned triangular mold with ZnO growth of 3.5 h. (a) Combined image quality (IQ) and inverse pole figure (IPF) obtained using electron backscatter diffraction (EBSD) of the ZnO base layer with the direction of the m-planes of the ZnO indicated with yellow lines. Electron backscatter diffraction combined IQ and IPF of a ZnO structure grown through (b) a mold aligned with the base layer crystalline planes and (c) a mold misaligned from the base layer crystalline planes by 30°. Yellow lines indicate the m-planes of the ZnO. (d) SEM micrographs taken perpendicular to the sample (upper images) and at a 45° tilt angle (lower images) with each pattern from left to right rotated an additional 10°. The first image shows when the mold and therefore the final ZnO structure was aligned with the hexagonal crystalline planes of the ZnO base layer.

EBSD measurements performed on the top surface of the grown ZnO structures confirm a common orientation of all the ZnO material relative to the base layer's crystallographic orientation. Figure 4.8(b) and Figure 4.8(c) show the combined image qualities and inverse pole figures, as well as measured ZnO m-plane orientations for a mold aligned with the base layer's crystallographic planes and for a mold misaligned 30° from the crystal structure of the base layer, respectively. Although the initial shape in the xy-plane is heavily influenced by the mold orientation, the m-plane orientation of the ZnO in both figures is the same. This indicates that while the crystalline orientation of the material is always the same, the final shape of the ZnO in the xy-plane can be changed by rotating the

mold through which it is grown. Similar measurements were taken on growth through other rotated shapes, such as squares and hexagons, and similar results were observed.

The data shown in Figure 4.7 and Figure 4.8 show the dominance of the growth rate perpendicular to the m-planes in producing the hexagonal symmetry in the xy-plane. Different sized patterned openings were combined with various rotations of the triangular patterns as shown in Figure 4.9 to better understand the transition from the lateral shape, defined by the mold, to the eventual hexagonal shape, dictated by the underlying orientation of the base layer. All of the growth conditions for the structures are kept the same, with a triangular core dimension of d= 3μm, 1.5μm, and 0.75μm, respectively, and growth time of 4 hours. Using a simple geometric calculation the length of each edge of the final structure at a given growth time can be calculated. The three edges of the hexagonal structure parallel to those of the patterned triangle have a length of $\sigma = 2\sqrt{3}b(t)/3 + a$, where $a = 2d\sqrt{3}/3$ is the side length of the patterned triangle and *b(t)* is the amount of growth perpendicular to the $(10\bar{1}0)$ m-plane direction as a function of time, as shown in the left most panel of Figure 4.9(a). The amount of lateral growth, *b(t)*, is found to be independent of the size of the patterned triangle. The remaining three sides of the final ZnO structure, which form from the vertices of the patterned triangle, have a length of $\beta = 2\sqrt{3}b(t)/3$. As expected, these are the same length for the three different size triangles patterned (2.99 ± 0.03μm). As the size of the patterned triangle openings is reduced, the value of *a* becomes small compared to $2\sqrt{3}b(t)/3$ and thus the shape in the xy-plane approaches a regular hexagon at earlier times in the growth. Therefore, by choosing a mold for the post region and strategically orienting the mold with respect to the crystalline orientation of the base layer, a variety of three-dimensional ZnO shapes can be grown with high quality sidewalls determined by the crystal

facets. In addition, if the diameter of the post is significantly less than the amount of lateral overgrowth then the resulting structures are hexagonal with smooth sidewalls, and have no dependence on the initial mold orientation.

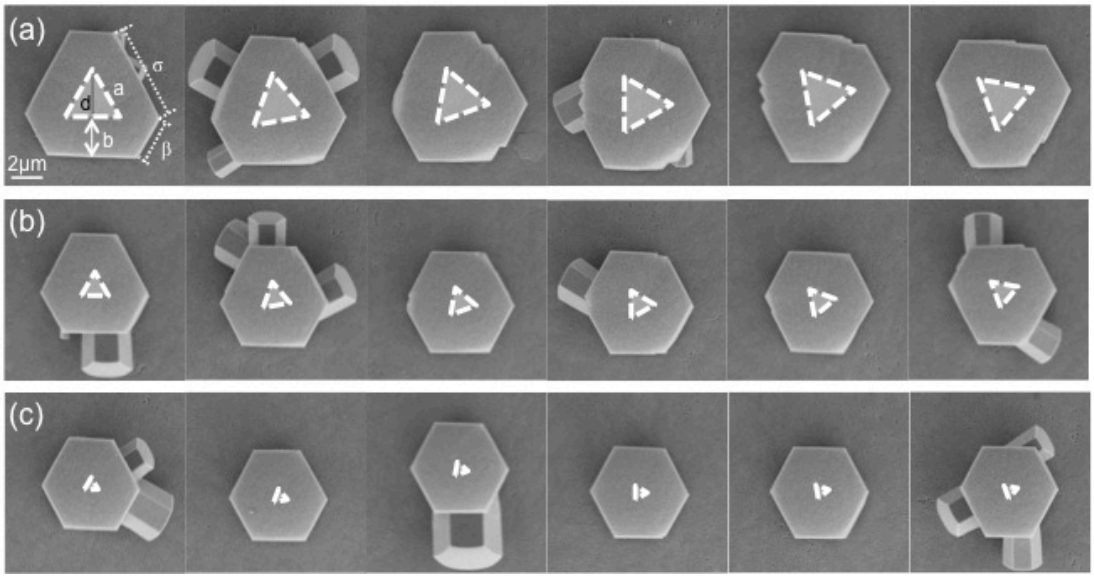

Figure 4.9: SEM micrographs of ZnO grown through (a) d = 3μm, (b) d = 1.5μm, and (c) d = 0.75μm patterned triangles in resist. (a is the length of the triangle, b is the amount of growth perpendicular to the m-plane direction of the ZnO, $\sigma = 2\sqrt{3}b(t)/3 + a$, and $\beta = 2\sqrt{3}b(t)/3$). In each successive image from left to right the patterned triangle was rotated an additional 10° relative to the crystalline planes in the ZnO base layer. Scale is the same for all images.

In some of the images in Figure 4.9 additional ZnO growth of the sides of the structures has occurred and is believed to have resulted from nucleation at specific sites on the lower part of the sidewalls of some of the structures [158]. While the origin of the extra nucleation is currently unknown, the density of the extra nucleation varies between samples which suggests some sort of contamination either in the growth solution or on the surface of the mold utilized. Further investigation is required to control the formation of such extra nucleation, and to further understand how the structure is modified as growth proceeds from constrained (by the mold) to unconstrained.

In this chapter, the ability to exert control over single crystalline zinc oxide structures aqueously grown through patterned molds of various shapes and sizes is shown. The ZnO precisely fills the molded region during growth regardless of the shape of the mold patterned. As expected, the faster growth rate of the c-plane of the ZnO with respect to the m-plane growth rate has been observed. The m-plane growth determines the lateral shape of the final ZnO structures, and the orientation of the mold with respect to the crystalline planes in the base layer is found to play an important role in the crystal facets observed in the final ZnO structures. By aligning the mold to the crystalline planes in the base layer, smooth, high quality sidewalls are observed. When misaligned, a variety of three-dimensional structures can be fabricated. In addition, when the diameter of the post is much smaller than the lateral overgrowth the final ZnO structures are hexagonal regardless of the orientation of the mold. The ability to easily fabricate ZnO structures with such smooth sides using this patterned aqueous growth technique, and without the use of possibly damaging etching techniques, opens the door to new and improved devices such as microdisks, photonic crystals, and lasers. Good quality material and smooth sidewalls are necessary for many devices as loss and scattering mechanisms need to be kept to a minimum for efficiently operating devices.

Chapter 5

Simulations and Fabrication of ZnO Devices

5.1 Introduction and Motivation

Photons, which travel at the speed of light and exhibit long coherence times, are excellent for transmitting information, and light has long been used as a means for communication. Optical telecommunication technologies, which have developed from the Nobel Prize winning first demonstration of light transmission along glass rods into a global high-speed broadband network, have transformed the modern world [159]–[162]. The development of photonic and optoelectronic devices has played an important role in the maturing of modern optical communication technology. The inventions of LEDs [56], [163]–[166], photodiodes [167]–[170], and most importantly solid-state laser diodes [171]–[173], have all been crucial in both miniaturizing and reducing the cost of telecommunication technology. These technologies have revolutionized optical science by providing reliable, cheap, and robust devices for transmitting and receiving optical information.

While light has proven to be an excellent means for transmitting information, as it does not suffer as greatly from interference and attenuation effects common with electric

transmission of information, it is less useful for information processing. In order for information processing to occur manipulation of data is required and it has proven difficult to interact with light in a nondestructive way. Typically, well-developed LED and laser diodes encode information in light and transmit it using fiber optics. Once the light is received at its destination it is converted into an electrical signal where information is processed in the solid state using well-developed integrated circuit technologies. These integrated circuit technologies have been developing at an astounding rate and companies such as Intel and IBM have been utilizing extensive resources to further develop these technologies. Moore's Law shown in Figure 5.1 describes the rate at which integrated circuit technology has been developing over the past several decades [1]. Approximately every two years the number of transistors per unit area of an integrated circuit doubles. This increase in transistor density over time will be difficult to sustain using established technologies as the dimensions of the transistors are currently approaching the size of atoms and quantum effects will become important at these length scales. As the size of the transistors is reduced, and the density of transistors increased, the thermal properties of integrated circuits become harder to control [2], [174]. Increased resistive heating from narrow transistor channels, combined with reduced surface area to volume effects, can make thermal management difficult [175], [176].

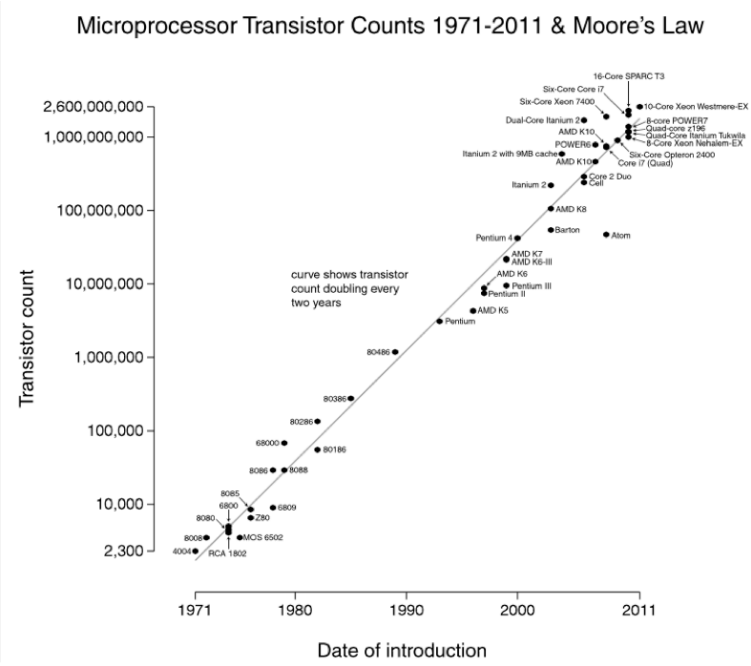

Figure 5.1: Number of transistors on a chip versus the year showing the increase predicted by Moore's Law. Reprinted with permission from [177].

As the practical limits of Moore's Law are being reached with established technologies there is a push to find new technologies to continue the development of processing power. Intel for example has developed an Ivy Bridge processor, which uses their 22nm process technology [178]. In these processors 3D tri-gate transistors are fabricated which allow for lower operating voltages and more channel control due to conductive channels formed using fin-like structures [179]. IBM on the other hand has demonstrated graphene integrated circuits [180], [181]. An advantage to using graphene is that faster processing of information can be achieved because of the much higher carrier mobilities in graphene than in previously used materials.

While new technologies continue to emerge that utilize information processing of electrical signals, a promising avenue of research is looking into using photonic technology

for information processing. Researchers at IBM have shown the ability to use pulses of light rather than electric current through small wires to transfer information from one processor to another on a chip [3], [182]. The ability to do so increases the processing speed while significantly reducing the cost, power used, and heating effects in the chip. These hybrid photonic-electronic technologies are shaping up to be the future for integrated circuits, and therefore photonic engineering of materials is likely to play an important role in developing new optical technologies.

5.2 Optical Cavities

Photonically engineered structures are typically very selective to the wavelength, propagation direction, phase, and other attributes of a photon's state. Importantly, these structures confine, store, and interact with light in a particular location overcoming the difficulty of creating stationary information. One such type of device that is specifically designed and fabricated to interact with light at a resonant wavelength is an optical cavity. In free space the wave vector for a given wave is unrestrained and can therefore propagate with any k-value. Cavities on the other hand, alter the density of states such that certain k-values are enhanced and others are suppressed. Take the basic example of a cube shaped cavity with edge lengths equal to L. The solution of Maxwell's equations for an electromagnetic wave within a volume V yields

$$E(r,t) = \sum_{k} E_k e^{i(k\cdot r-\omega t)} \tag{5.1}$$

The electromagnetic field is made up of the superposition of travelling waves where $\omega = c|k|$. The allowed values of k_x, k_y, k_z can be determined by considering the boundary conditions for the cavity. In this example:

$$k_x L = 2\pi n_x$$
$$k_y L = 2\pi n_y \quad (5.2)$$
$$k_z L = 2\pi n_z$$

where n_x, n_y, and n_z are integers. The allowed values for the wave vector in the cavity can be written as shown in Equation 5.3.

$$k \equiv (k_x, k_y, k_z) = \frac{2\pi}{L}(n_x, n_y, n_z) \quad (5.3)$$

Due to the boundary conditions when solving Maxwell's First Equation, each set of (n_x, n_y, n_z) integers actually represents two modes of the cavity with different polarizations. From Equation 5.3 it is apparent that waves with only certain k values are allowed in the cavity as these are standing waves that constructively interfere. Waves that are out of phase will destructively interfere and will be suppressed by the cavity. While this example is specifically for a cube shaped cavity, the basic principle of only certain k-values being sustained in the cavity remains the same regardless of the shape of the cavity.

The patterns created by standing waves in cavities are referred to as the modes of the cavity. Typically, optical resonators are characterized by two key qualities: the quality factor (Q-factor) and the modal volume. The quality factor of a cavity characterizes how well the cavity contains the light and is related to the decay time of the resonant mode. The quality factor can also be thought about as the fraction of photons that will escape the cavity in a given time. The modal volume is simply the volume that is occupied by the confined optical mode.

In general, cavities alter the density of states in a very frequency dependent way, which allows for the engineering of cavities such that there is a high degree of selectivity of the wavelength and polarization of the light enhanced in them. A simple cavity designed to operate at a specific resonant wavelength can be made from small volumes of materials with the correct dimensions so that an integer number of wavelengths are contained in the structure as described above. The confinement in these cavities can be achieved by reflections at the edges of the volume due to the difference in the refractive indices of the material, for example between a dielectric and air or two different low-loss dielectric materials. These microcavities typically have at least one dimension on the order of the wavelength of light that it is designed for. Several optical cavity geometries have been fabricated such as micropillars, microspheres, and microdisks [183]. Silica microspheres have been found to be one of the best cavities at containing light (highest Q-factor) however; they have numerous densely spaced modes limiting their usefulness for certain applications such as stable lasers [184]–[186]. Microrings and microdisks also have relatively high quality factors and in general are easier to fabricate than microspheres making them more attractive for integrated optical networks. These micro-cavities have been fabricated out of numerous types of materials and are important for well-developed optical technologies such as lasers [187]–[189] and wavelength dependent sensors [190], [191]. Some various types of microcavities from Vahala's review paper are shown in Figure 5.2 [183]. In addition, there are more advanced applications of cavities in emerging fields such as optical computing where they are used to enable photon-photon interaction and non-destructive measurements of photon states [192], [193].

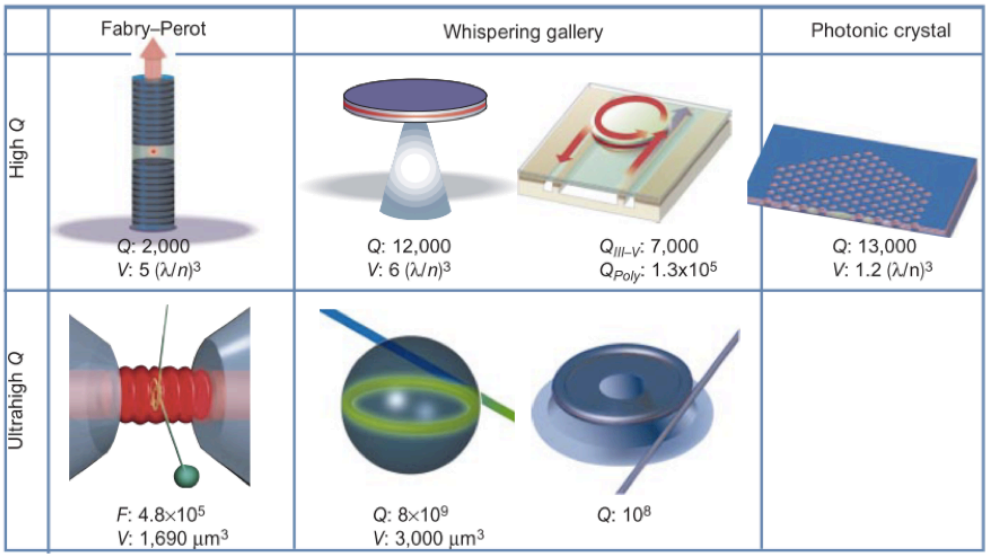

Figure 5.2: Illustrations of several types of microcavities from [183]. The top row, from left to right, shows a micropost, a microdisk, an add/drop filter, and a photonic crystal. The bottom row, from left to right, shows a Fabry-Perot bulk optical cavity, a microsphere, and a microtoroid. Reprinted by permission from Macmillan Publishers Ltd: Nature [183], copyright 2003.

Often the inherently available confinement ability of the cavities mentioned above is not at the desired wavelength for a given application. As a structure about the size of the wavelength being investigated is needed for optical manipulations it may not always be possible to fabricate a device small enough. One way to overcome this is to use photonic crystals, which are materials with an engineered periodicity that is different than the periodicity of their underlying material crystalline structure. Bragg reflection from the engineered periodicity allows the structures to interact strongly with other wavelengths of light. In addition to pure reflection, the structures can be engineered to have complicated spatially varying periodicity patterns to allow for other manipulations.

In addition to cavities, periodic structures have also been used to make filters and waveguides. The periodicity of a structure can be engineered in such a way as to allow light

of only certain wavelengths to pass or reflect through the structure. Such devices are known as transmission and reflection filters respectively and have been used in a range of fields. For example, distributed Bragg reflector (DBR) mirrors, used in many types of optoelectronic devices, strongly reflect certain designed wavelengths of light while allowing others to pass through. Periodic structures have also been used as waveguides to confine and direct light in many types of optoelectronic devices. Devices with materials of different indices of refraction are designed such that optical waves are guided through the structure by total internal reflection.

Careful fabrication of cavities and periodic structures is crucial as it is often important for them to have smooth sides, flat faces, precise shapes and sizes, and be made out of high quality material. Traditionally most of the microcavities to date have been fabricated using top-down approaches where a bulk piece of material is etched away to create the desired structure [40], [194]. Often these top-down techniques damage the material the cavity is made out of and don't always provide the most smooth structure edges. As shown in the previous chapter, the constrained aqueous growth of ZnO technique used in this work is an ideal method for fabricating high quality optical structures of various shapes and sizes. Not only are the structures single crystalline but they also have crystalographically smooth sidewalls, which are ideal for optical devices. In addition, pillar structures with high aspect ratios are inherently difficult to fabricate using most top-down techniques. The constrained aqueous growth method used throughout this work allows for the easy fabrication of high aspect ratio pillars, which can be made into cavities, filters, and waveguides. In this chapter, three types of microcavities made out of single crystalline ZnO are fabricated and simulated. These devices include microdisk resonators, ring structures, and photonic crystals. In

addition to detailing the progress made towards fabricating and measuring these three types of devices, a detailed explanation of some of the challenges will be presented.

5.3 Microdisk Resonators

Microdisk resonators are circular cavities of dielectric materials where light is confined by total internal reflection at the boundary of the structure. The light propagates around the inner circumference of the disk such that the angle of incidence of the light is greater than the critical angle resulting in whispering gallery modes as shown in Figure 5.3. The round trip path length of the light in the circular cavity can be written as:

$$\text{round trip path length} = Nd \tag{5.4}$$

where

$$d = 2a(\sin(\pi/N))$$

and *a* is the radius of the disk. One condition of a resonant mode in a cavity is that the path length of the cavity must be equal to an integer number of wavelengths as shown in Equation 5.5.

$$Nd = q\lambda = qc/\nu, \quad q = 1, 2, 3\ldots \tag{5.5}$$

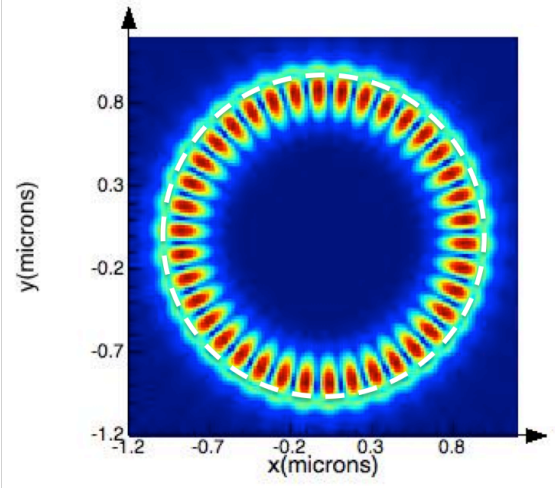

Figure 5.3: FDTD simulation of whispering gallery modes of circular ZnO microdisk resonator with r = 1μm and 250nm thickness. The white dotted line is the boundary of the microdisk.

This results in resonant frequencies (ν_q) of the cavity and spacing (ν_F) between the frequencies as given in Equations 5.6 and 5.7.

$$\nu_q = qc/Nd \tag{5.6}$$

$$\nu_F = c/Nd \tag{5.7}$$

For a circular cavity such as a microdisk resonator, the limit where N, the number of reflections, approaches infinity is used. In this case the path length becomes the circumference of the disk ($2\pi a$) and the spacing between the resonant frequencies is $c/2\pi a$.

The mode profile of a cavity shows how the electric field is distributed for electromagnetic waves of a certain k-value in a cavity. In microdisk resonators, circular optical modes, also referred to as whispering gallery modes, are present as shown in Figure 5.3. Derivations of the whispering gallery mode profile can be found in [195]. Whispering gallery modes are the highest quality factor modes in microdisks but there are also other modes, such as radial modes, that are not as well confined to the structure. The mode

profiles for all optical structures in this chapter were calculated using Lumerical FDTD Solutions.

Microdisk resonators have been fabricated out of many materials including silicon, GaAs, GaN, and diamond [194], [196]–[198]. These structures are fabricated from a bulk piece of material and masked such that etching processes produce the desired size and shape of the microdisks. The use of etching steps in the fabrication of optical structures is often less than ideal as it can damage the material and decrease the quality factor of the device. In addition, selective undercut etching to produce good optical isolation is often a challenge. Microdisk resonators have also been fabricated in ZnO although there are limited reports of such structures [45], [199]–[201]. Most of the reports of observed whispering gallery modes in ZnO have come from microwire and nanowire structures [53], [202]–[205]. Controlled etching of zinc oxide is difficult and therefore the ZnO microdisks reported in the literature were grown using chemical vapor transport or metal-organic chemical vapor deposition (MOCVD). While these techniques produce the thin microdisk structures needed to observe whispering gallery modes, the fabrication of the structures is done at high temperatures, the precise size of the microdisk can be difficult to control, and the material is often polycrystalline. In addition, the crystalline structure of zinc oxide strongly influences the shape of the grown microdisks and therefore only ZnO hexagonal microdisks have been reported to date with fairly low quality factors compared to circular disks [45], [199].

In contrast, our aqueous growth is done at low temperature (90°C), produces single crystalline ZnO, and allows for control of the size and shape of the disks. The fabrication steps used to make ZnO microdisks is shown in Figure 5.4.

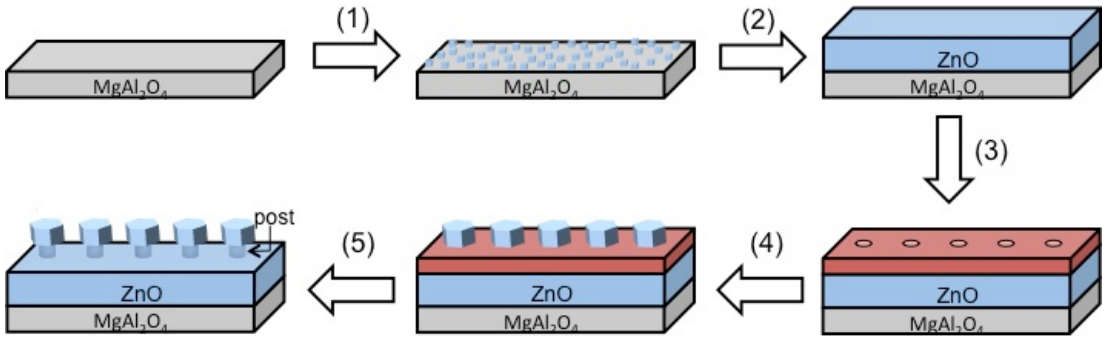

Figure 5.4: Fabrication process for ZnO microdisk formation. (1) ZnO nucleated on $MgAl_2O_4$ substrate. (2) ZnO base layer growth. (3) E-beam patterning of PMMA. (4) ZnO growth. (5) Resist removal.

To create optical isolation from the base layer of ZnO, the microdisks were fabricated by allowing the ZnO to overgrow the masked regions and produce undercut structures. The ZnO structures grown were predominately hexagonal, as has been shown in Chapter 4 and previously reported in the literature. More rounded structures can be achieved by varying the growth time although typically at the expense of the amount of undercut achieved. FDTD simulations were performed to investigate the effect of varying the amount of undercut for 250nm thick, 1μm radius microdisks. The cross-sectional and top-down mode profiles for post radii of 250nm, 750nm, 850nm, and 975nm are shown in Figure 5.5. In addition, the quality factors are calculated for the λ=472nm mode for different post radii and are shown in Table 5.1. These simulations show that for the 1μm radii disks the whispering gallery modes remain in the 250nm thick disk region with posts up to radii of 850nm. As the post radius increases above this point, more of the mode leaks into the post region as shown in Figure 5.5(g). The quality factors of the mode at λ=472nm are found to stay relatively the same until a post radius of 750nm and then begin to sharply decrease for larger radii posts. The

calculated quality factor for the ZnO microdisk with the 750nm post seems to be an anomaly and has a large error. Therefore, this quality factor value was mostly discounted.

Post Radius	Quality Factor
0nm	167,882 +/- 675.9
250nm	166,563 +/- 942.2
500nm	167,125 +/- 944.2
750nm	391,778 +/- 10,452.9
850nm	59,745.9 +/- 34.9
975nm	19,8876 +/- 4,409

Table 5.1: Quality factors for 250nm thick, 1μm radii ZnO microdisks on 500nm thick posts of varying radii.

The optical confinement in these circular microdisks on posts can be achieved with relatively large posts due to the difference in the effective refractive index of the post region versus the microdisk. As the post radius increases, the effective refractive index of the post region approaches that of the microdisk causing leaking of the optical mode from the microdisk into the post and lowers the quality factor. To fabricate circular ZnO microdisks using the aqueous growth method, very short growth times are required as to not allow the ZnO enough time to form into the usual hexagonal shape. We have found that at these relatively short growth times the amount of undercut achieved is very small and significant leaking of the light into the post region would occur based on simulated values.

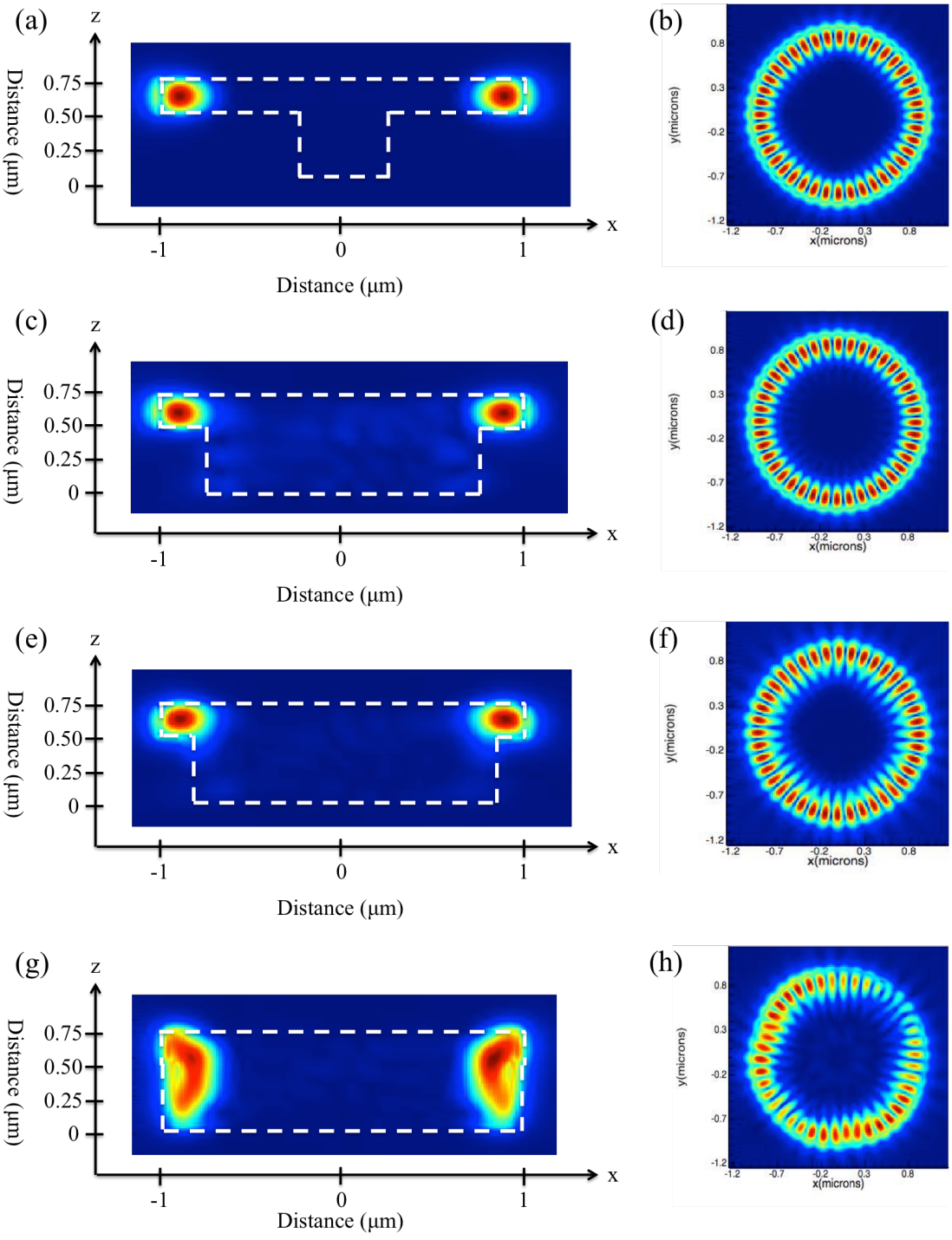

Figure 5.5: Cross-section FDTD simulations of 250nm thick circular ZnO microdisks on 500nm tall posts with radii (a) 250nm, (c) 750nm, (e) 850nm, and (g) 975nm. (b), (d), (f), and (h) are the corresponding top-down view of the simulations shown in (a), (c), (e), and (g) respectively.

On the other hand, crystallographically smooth hexagonal structures can easily be fabricated as shown in Figure 5.6. While these hexagonal structures have smooth, vertical sidewalls, they are typically several microns tall and therefore will not be able to produce optical confinement in the vertical direction. Sodium citrate is included in the growth solution to slow down the growth in the vertical direction as shown in Chapter 4 however, the vertical growth could not be slowed down enough to produce ~250nm-500nm tall structures with suitable undercuts. Figure 5.7 is a FDTD simulation of the cross-section of two circular microdisks of different heights showing the optical confinement achieved for a 0.25μm and 1μm thick circular microdisk at a wavelength of 402nm and 383nm respectively. The 0.25μm tall microdisk has only one whispering gallery mode in the vertical direction that is well confined to the outer part of the disk. The 1μm tall microdisk, on the other hand, has poor vertical confinement with multiple lobes in the vertical direction, which can lead to lower quality factors.

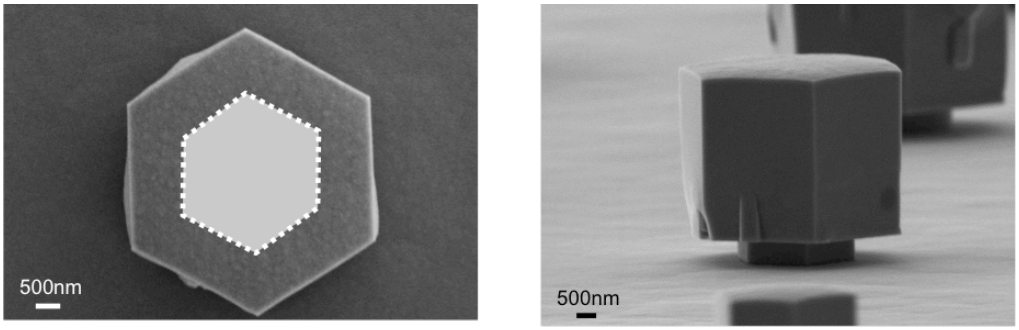

Figure 5.6: ZnO "microdisk" structure grown for 4 hours through a hexagonal mold. The left SEM image is taken perpendicular to the substrate and the right image is at a 6.5° angle.

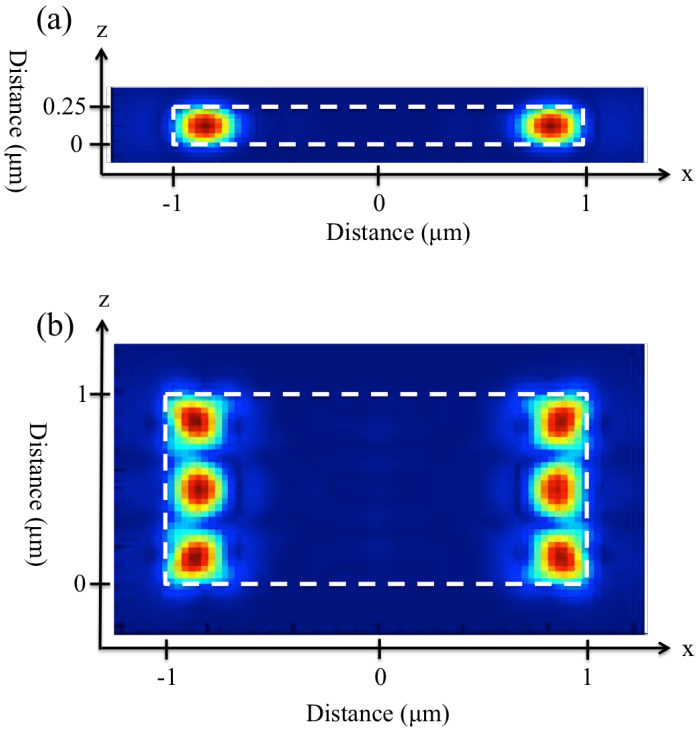

Figure 5.7: Cross-section FDTD simulation of (a) 0.25μm tall circular microdisks at 402nm and of (b) 1μm tall circular microdisks at 383nm.

Optical measurements were performed on structures such as those shown in Figure 5.6 however, modes were not observed. While this is in part due to the height of the structures grown, it has been shown that modes are still present in thicker structures. It is therefore believe that the hexagonal shape of the ZnO devices severely limits the modes confined in the cavity. To thoroughly investigate the modes and quality factors of the modes expected in microdisks with different number of sides, FDTD simulations were performed as shown in Figure 5.8. All microdisks in Figure 5.8 are 0.25μm tall and have a radius of 1μm. The quality factors of the microdisks increase as the number of sides of the microdisks increase. This is expected, as the limit of increasing the number of sides of a geometric shape is a circle. It is also noted that while the hexagonal microdisk is able to confine light at

certain wavelengths, the quality factor of such modes is very low. In the mode profile of the hexagonal microdisk, one can see significant leaking of the light from the microdisk leading to the low quality factor of approximately 200. A ZnO microdisk with 8 sides however shows an almost 5 times improvement in the quality factor, and a microdisk with 10 sides has a quality factor of approximately 1400.

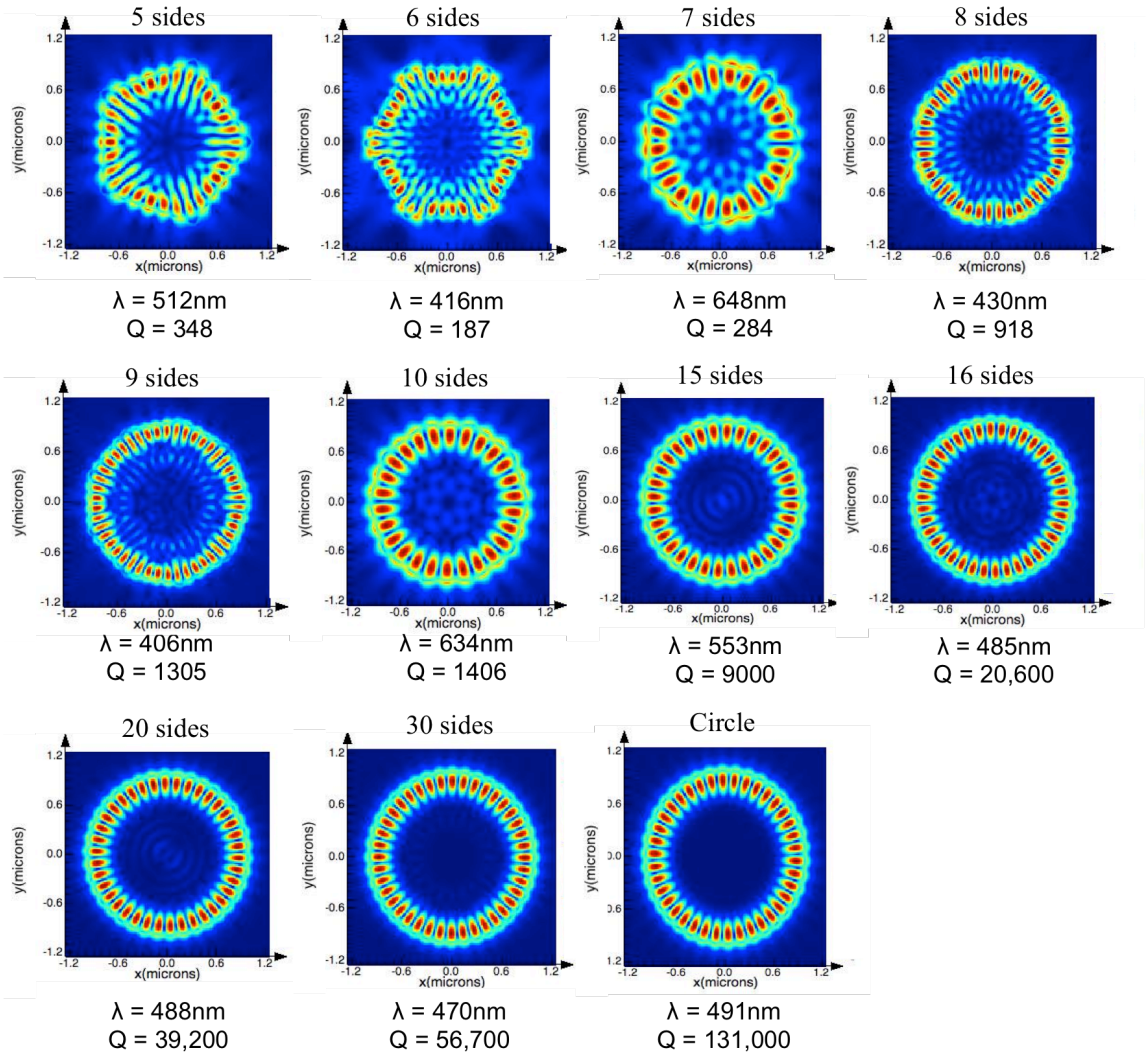

Figure 5.8: FDTD simulations of the mode profiles in ZnO microdisks with different number of sides. The wavelength of the mode and the quality factor are also reported for each microdisk. All microdisks are 250nm thick and have a radius of 1μm.

Due to the height and hexagonal shape of the ZnO microdisk structures, as well as the amount of undercut that can be obtained for the shortest, most circular structures, it is concluded that our aqueous growth method is not the ideal fabrication method to produce high quality ZnO microdisks. While it is possible that altering the growth solution and growth time may be able to produce more circular structures, the height of such structures is still more than the ideal height for typical microdisks.

5.4 Ring Structures

Similar to microdisk resonators, ring resonators confine light due to total internal reflection at the boundary of the ring and often air. One can think of a ring resonator as a waveguide that has its two ends brought together. Modes will be supported in the structure when the wavelength of the light is equal to the optical path length in the ring. Ring resonators have been fabricated in many material systems including silicon and III-V materials [206], [207]. These structures have been used as filters, biosensors, and lasers due to their ability to effectively confine light at specific frequencies [208]–[211]. Circular ring structures have shown quality factors on the order of 10^5, which is higher than quality factors measured in microdisk resonators. For many applications ring resonators are only useful if they can be coupled to another device or structure. In this work the investigation is restricted to only consider the fabrication of the ring itself and the possibility of modes being supported in the structures.

ZnO ring structures were fabricated in a similar manner to the ZnO microdisks in the previous section. A base layer of ZnO was grown and electron-beam resist was used as a mold for the growth. Triangular, circular, and hexagonal rings of various shapes and sizes

were patterned in the resist. The single crystalline ZnO was then grown through this mold and overgrown to produce the ring structures. Figure 5.9 shows ZnO ring structures grown for 2.25 hours through triangular ring openings of different thicknesses. The edges of the triangular molds were aligned with the m-planes of the ZnO in the base layer, which therefore resulted in triangular ZnO ring structures. While these structures will not make good resonators they do provide additional insight into the growth of ZnO through constrained molds.

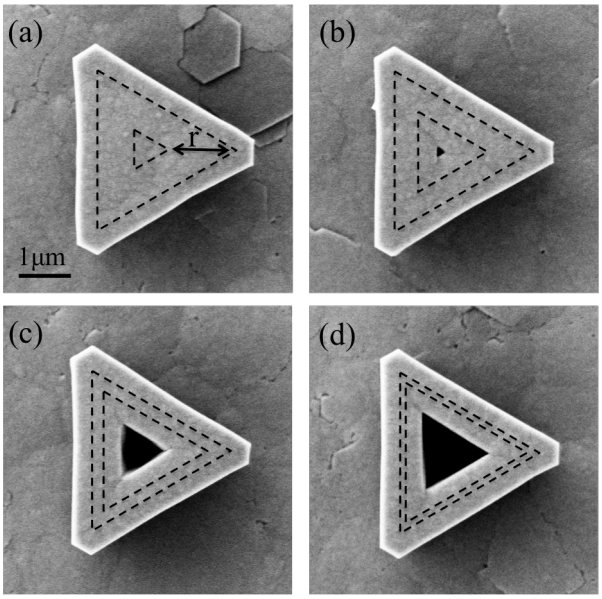

Figure 5.9: Triangular ZnO rings grown for 2.25 hours through (a) r =1.5μm, (b) r= 1.0μm, (c) r= 0.5μm, and (d) r= 0.25μm ring openings outlined by the black dashed lines.

As seen in Figure 5.9(a), if the thickness of the patterned ring is large enough the ZnO in the center of the triangular ring coalesces without any indication that the material grew together. In addition, the inside edges of the ZnO structures form triangles instead of the usual hexagons seen with ZnO. The outside edges of the structure are hexagonal as seen in previous chapters with growth through triangular molds.

Hexagonal and circular rings of different thicknesses were also patterned in the e-beam resist and ZnO was grown through the molds for 2.25 hours. The resulting structures are shown in Figure 5.10 and Figure 5.11 respectively. Again for the rings with r=1.5μm, the ZnO coalesces in the center with no indication that the overgrown ZnO grew from ring patterns. The shape of the overgrown, unconstrained material is determined by the rate of growth of different crystalline planes of ZnO. The growth outward from the ring molds results in the typical hexagonal shape due to the slow growing m-planes of ZnO. The growth inward from the ring mold, resulting in the inner facets, however, results in a 30° rotation with respect to the outer facets of the structures. This rotation between the inner and outer facets can most clearly be seen in the structures grown through the thinnest ring molds, Figure 5.10(d) and Figure 5.11(d). The inner facets are defined by the faster growing $(11\bar{2}0)$ a-planes of ZnO due to the shrinking of a void. This is the first report of ZnO growth from patterned openings resulting in ring structures where the inward and outward growth of the material can be studied. Previously, Jindal et al. simulated the expected growth shapes of GaN grown through circular ring openings at various times and compared them to actual GaN structures grown using a selective area growth technique. GaN and ZnO have the same crystalline structure and one would expect similar results from growth through circular ring molds in each case. The results reported here are in good agreement with Jindal et al.'s findings that the outer growth front results in six $(1\bar{1}01)$ planes and that the inner growth front results in six $(11\bar{2}1)$ planes [212].

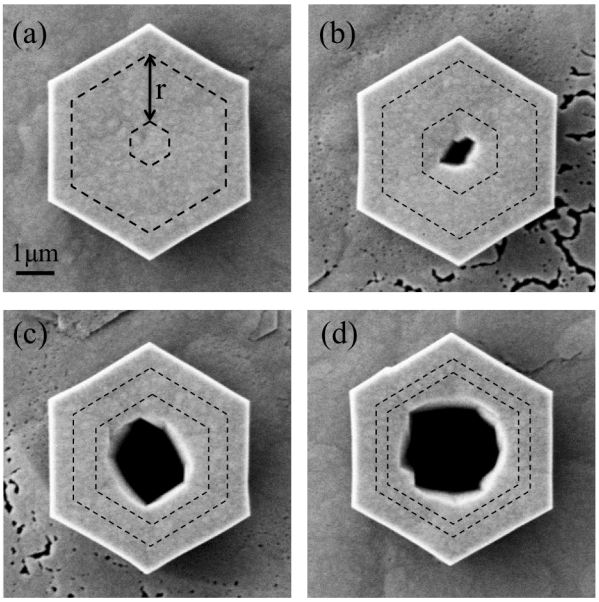

Figure 5.10: Hexagonal ZnO rings grown for 2.25 hours through (a) r =1.5μm, (b) r= 1.0μm, (c) r= 0.5μm, and (d) r= 0.25μm hexagonal ring openings outlined by the black dashed lines. The distance from the center of the patterned ring to the vertex of the outer hexagon is equal to 2.0μm.

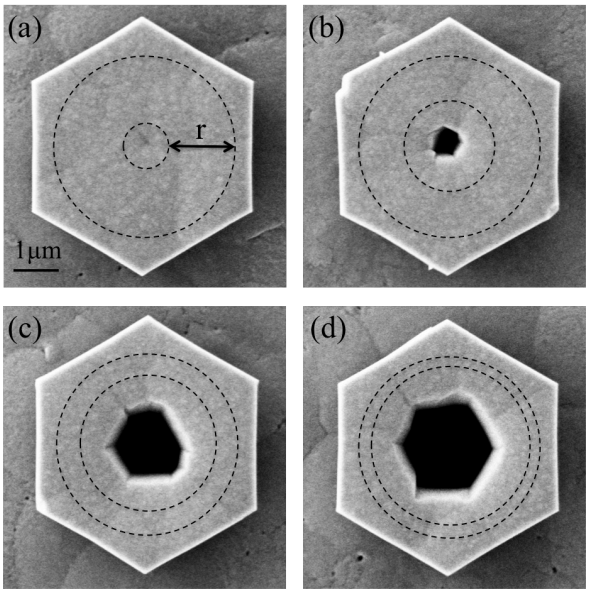

Figure 5.11: Hexagonal ZnO rings grown for 2.25 hours through (a) r =1.5μm, (b) r= 1.0μm, (c) r= 0.5μm, and (d) r= 0.25μm circular ring openings outlined by the black dashed lines. The outer ring radius is equal to 2.0μm.

Focused ion beam milling was used to cut the grown ZnO ring structures in half to image the cross-sectional profile. Scanning electron microscopy images of the ZnO structures grown for 2.25 hours through hexagonal ring molds with r = 1.5μm, 1.0μm, 0.5μm, and 0.25μm are shown in Figure 5.12. Similar cross-section images were taken of ZnO grown through circular ring molds as shown in Figure 5.13.

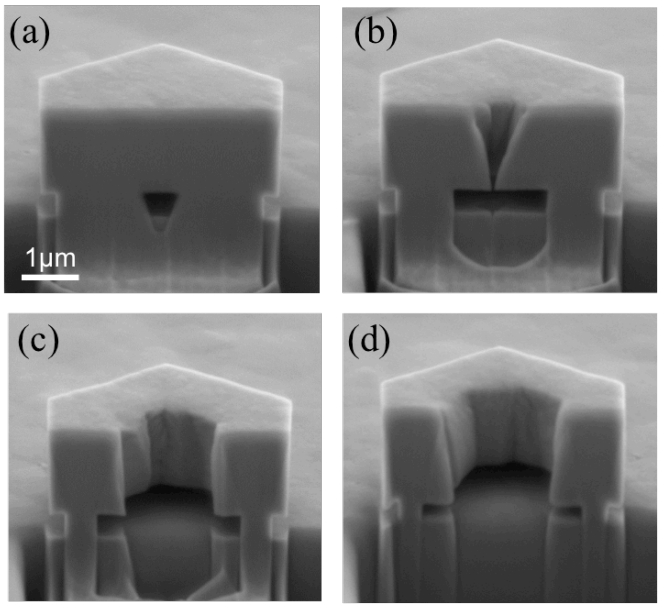

Figure 5.12: SEM images of focused ion beam cut ZnO structures grown for 2.25 hours through (a) r =1.5μm, (b) r= 1.0μm, (c) r= 0.5μm, and (d) r= 0.25μm hexagonal ring openings.

All of the single crystalline ZnO ring structures grown for 2.25 hours have a height of approximately 1.3μm. In Figure 5.12(a) and Figure 5.13(a) where the largest (r=1.5μm) ring was patterned in the e-beam resist the overgrown single crystalline ZnO still shows no signs, such as defects, of where it joined together during the growth process. The outer facets of all of the structures are vertical, however, the interior facets in some cases appear to be slanted. While the exact cause of these tilted interior facets is still under investigation, it is believed

that they may be due to insufficient flow of the growth solution in these small regions during the growth processes.

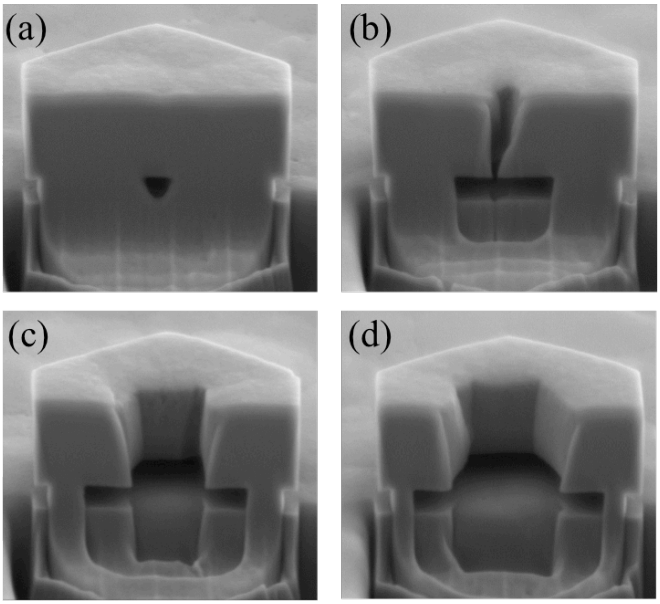

Figure 5.13: SEM images of focused ion beam cut ZnO structures grown for 2.25 hours through (a) r =1.5μm, (b) r= 1.0μm, (c) r= 0.5μm, and (d) r= 0.25μm circular ring openings.

In order to fabricate more circular ZnO ring structures, circular rings were patterned in e-beam resist with a variety of outer radii ranging from 3μm to 10μm. All rings were patterned with a thickness of 250nm. Top-down SEM images of the ZnO structures are shown in Figure 5.14. The larger ZnO ring structures appear to have slightly more rounded corners than the smaller radii structures however; a clear hexagonal shape for both the interior and exterior facets of the rings is observed. When fabricating optical devices it is important to have control over both the size and shape of the device being fabricated. Changing the radius of the ZnO ring structure changes the wavelength of the mode supported in the cavity. Therefore, depending on the application of the device a wide range of different sized resonators may be needed.

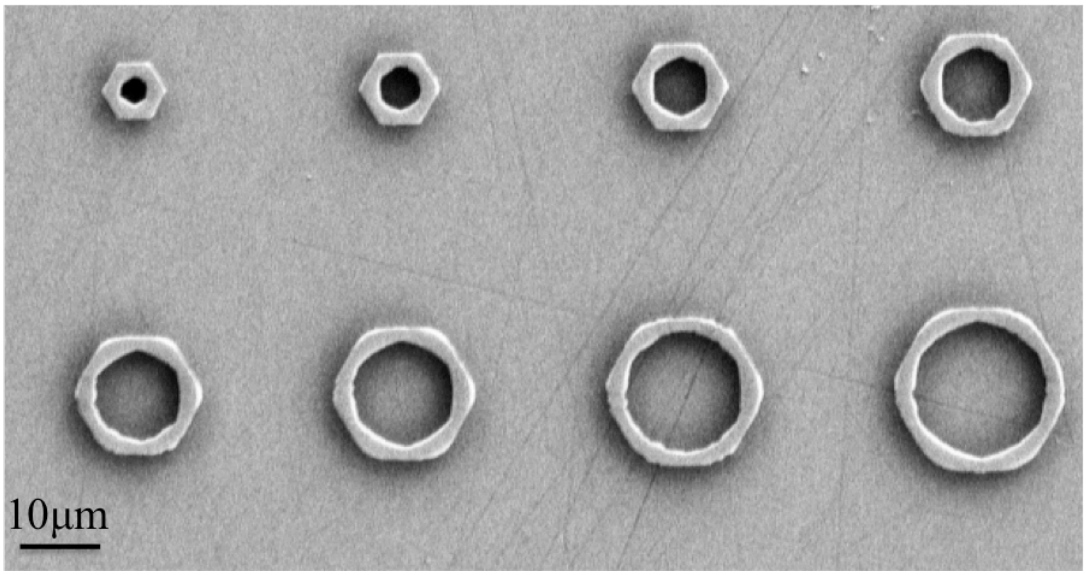

Figure 5.14: SEM image of single crystalline ZnO ring structures grown for 2.25 hours through circular rings patterned in PMMA. Outer ring radii ranged from 3.0μm (upper left) to 10.0μm (lower right). The thickness of the patterned rings is equal to 250nm.

Similar to the ZnO microdisks in the previous chapter, the height of these ring structures along with the hexagonal shape limits their usefulness for optical resonators due to the low quality factors of modes in the structures. The fabrication of the ZnO ring structures is however, important to further understand the capabilities of the aqueous ZnO growth method in this work. ZnO grown through larger ring shaped molds coalesce into smooth overgrown structures without any indication of where the material grew together. In addition, these ring structures allowed for the study of ZnO growth both outward and inward from the patterned ring mold.

5.5 Photonic Crystals

In a crystalline material, the atoms are arranged in a periodic fashion referred to as the crystalline lattice. An electron moving in this crystalline lattice will experience a periodic

potential due to the repeating structure of the crystal. These electrons will propagate through the crystal as waves, known as Bloch waves. The relationship between the momentum and energy of electrons in a Bloch wave is known as the dispersion curve. Not every combination of momentum and energy is allowed, as there are some ranges of energy for which no propagating Bloch waves exist. This range of energies is known as the bandgap, which manifests itself as a range of energies in which no electron states exist.

The optical analogy of electrons moving through a crystal is photons moving through a periodically engineered material, known as a photonic crystal. Photonic crystals can be fabricated in one dimension, two dimensions, or three dimensions, as shown in Figure 5.15 [35]. Stacking alternating layers of thin dielectric materials with different refractive indices can create one-dimensional photonic crystals. Two-dimensional photonic crystals can be fabricated by etching a 2D pattern of holes in a slab of dielectric material or by making rods of dielectric material into a 2D pattern. Three-dimensional photonic crystals, which it is no surprise have proven to be the most difficult to fabricate, have been formed in several ways. One such method used multiple iterations of etching and material deposition to fabricate a "woodpile" structure of silicon rods in air [213]. The designed periodicity in all of these structures is what interacts with the light.

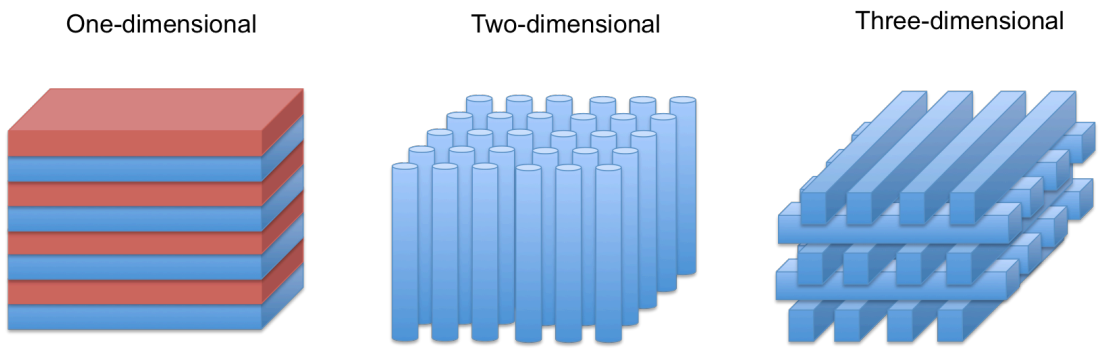

Figure 5.15: Examples of periodic structures in one, two, and three dimensions suitable for use as photonic crystals.

For a one-dimensional photonic crystal, as shown in Figure 5.16, the reflectivity will be highly wavelength dependent for light incident perpendicular to the periodic layers. This high degree of wavelength selectivity is due to the interference between waves that are reflected from each interface as the light propagates through the crystal. When reflections from successive interfaces constructively interfere the structure exhibits a high reflectivity. The wavelength at which this occurs is highly dependent upon the thickness and refractive index of each layer. This is because the phase difference between successive reflected waves is given by $\delta = \frac{2\pi}{\lambda} 2nl$ where l is the layer thickness and n is the refractive index. When the layer thickness, l, is equal to an integer multiple of $\frac{\lambda}{2n}$, the phase difference is 2π and the Bragg criteria is satisfied such that constructive interference occurs.

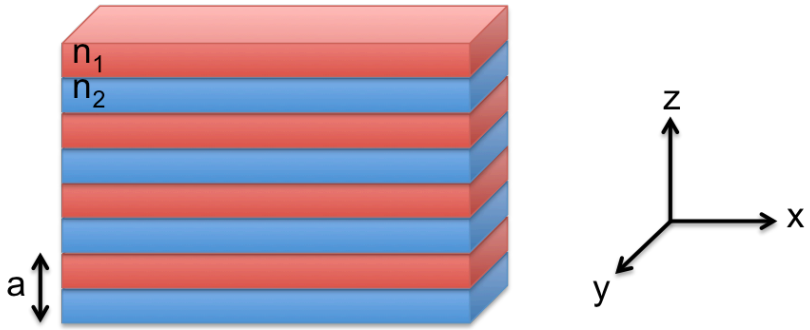

Figure 5.16: One-dimensional photonic crystal formed from alternating layers of material with refractive indices n_1 and n_2. The spatial period of the structure is *a*.

Similar to the bandgap for electrons in crystals, photonic crystals form optical bandgaps. The photonic bandgap in a photonic crystal is the range of energies at which electromagnetic waves are not able to propagate. In the one-dimensional photonic crystal in Figure 5.16, electromagnetic waves that meet the Bragg criteria will be highly reflected from the photonic crystal and therefore will not propagate through it forming the photonic bandgap.

Often 2D photonic crystals designed with a defect in the bandgap are fabricated and have been shown to have large quality factors and small modal volumes [214], [215]. Photonic crystal cavities without defects, based on band edge modes, have also been shown to have large quality factors and have been used for several applications [216]. Band edge modes, as the name suggests, are located at the edge of the photonic bandgap of a photonic crystal. These modes are of interest because at the band edge the group velocity of the propagating states approaches zero. In addition, it has been shown that certain geometric patterns of pillars can confine photons via internal total reflection [216], [217]. Therefore, photons with certain energies inside the photonic crystal can constructively interfere and form band edge modes

There are two types of 2D photonic crystal cavities: two-dimensional array of holes in a dielectric slab and two-dimensional array of dielectric pillars. 2D slab photonic crystals with holes etched into the dielectric material have been fabricated in several materials systems including GaAs and silicon [218]–[220]. ZnO however, is difficult to etch and our aqueous growth technique lends itself well to tall pillar structures. These high aspect ratio pillars made into photonic crystals, which are difficult to form in most material systems using top-down approaches, have the possibility to be used as filters, waveguides, and cavities. Such photonic crystal devices have been fabricated in many types of materials systems [221], [222]. The ability to create such high aspect ratio ZnO pillar photonic crystals using a constrained aqueous growth method is promising for the development of high quality waveguides for low-loss bending of light and filters for careful wavelength selection in devices. In addition, ZnO pillar photonic crystals can also be used to make cavity structures, as simulated later in this chapter. In cavities it is often desirable for the maximum of the mode to couple to an emitter. ZnO has shown potential for use in optical cavities, as it may be possible to implant optically active defects into the material, which can then couple to the cavity [223]. Given the numerous applications of pillar structures, this work focuses on 2D pillar photonic crystals. Several groups have fabricated 2D pillar photonic crystals out of various materials including ZnO [43], [216], [224], [225].

In this section two-dimensional single crystalline ZnO pillar photonic crystals are simulated using FDTD software and fabricated using the aqueous, constrained growth method. Square arrays of ZnO pillars are grown through patterned holes in e-beam PMMA resist as shown in Figure 5.17. The radius of the ZnO pillars as well as the spacing between

the pillars, the pitch, can be easily be modified by changing the radius of the holes patterned in the PMMA and the spacing between the holes respectively.

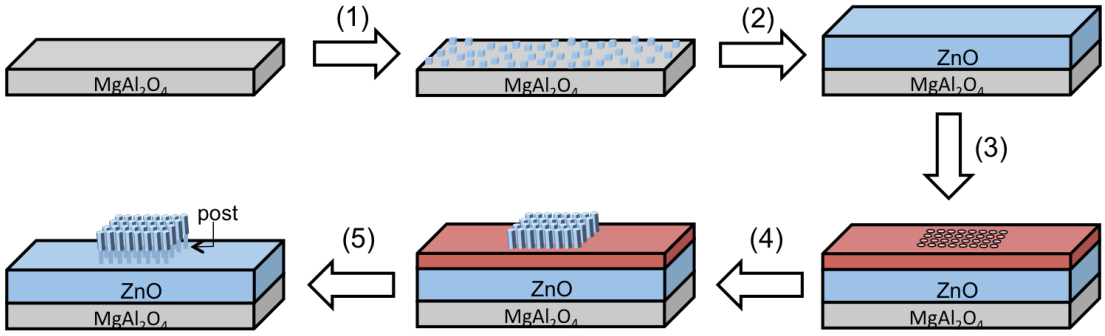

Figure 5.17: Fabrication steps for making ZnO single crystalline pillar photonic crystals. (1) ZnO is nucleated onto cleaned $MgAl_2O_4$ substrates. (2) Base layer of ZnO grown. (3) PMMA resist is spun on the sample and square array of holes is patterned into the resist using e-beam lithography. (4) Sample placed in ZnO growth solution for desired amount of time to form pillars. (5) PMMA is removed from the sample.

The band structure for several ZnO photonic crystals consisting of 50nm-100nm radius pillars each with a pitch of 250nm is shown in Figure 5.18. The band structure for each photonic crystal is calculated using FDTD simulations that assume both infinitely long ZnO pillars and an infinite number of repeating pillars in both the x and y directions. The infinite lateral extent is included in the simulations by use of periodic boundary conditions. The important parameter in these photonic crystals is the ratio of the pillar radius to pitch distance. This radius to pitch value will often be referred to in this work. In Figure 5.18 the radius to pitch (r/a) values are 0.2, 0.24, 0.28, 0.32, 0.36, and 0.4. The y-axis of the band structure plots is given as a normalized frequency because each r/a value produces the same band structure regardless of the actual radius and pitch of the photonic crystal. Changing the radius and pitch values, but keeping the r/a value the same, shifts the wavelength at which the band structure is seen.

In this work only TM modes were simulated and the lowest band edge mode in the M-direction of the crystal was studied. In Figure 5.18 the light lines for air, the spinel ($MgAl_2O_4$) substrate, and ZnO are shown as black, blue, and green lines respectively. A mode will more easily couple to a material if the mode lies above the light line. For all of the band structures in Figure 5.18, the band edge mode of interest (M-direction) is far below the vacuum light line and therefore will not couple to the air above the pillars. In Figure 5.18(a and b) the band edge mode also lies above the light line for the spinel substrate and significant leaking of the mode into the substrate would be expected in these cases. Ideally, the mode should lie above the light line for ZnO and below the light line for spinel so that the mode will be concentrated in the pillar region.

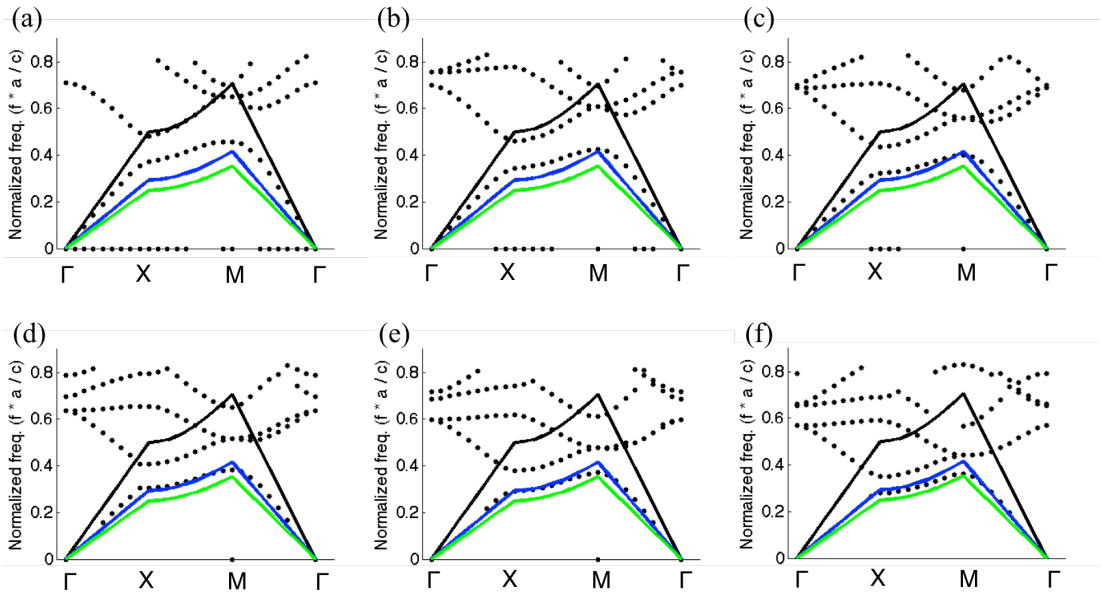

Figure 5.18: Band structure diagrams for 2D ZnO pillar photonic crystals with (a) r=50nm, (b) r=60nm, (c) r=70nm, (d) r=80nm, (e) r=90nm, and (f) r=100nm. The pitch of the pillars in all of the simulations was *a*=250nm. The black, blue, and green lines are the light lines for air, spinel, and ZnO respectively.

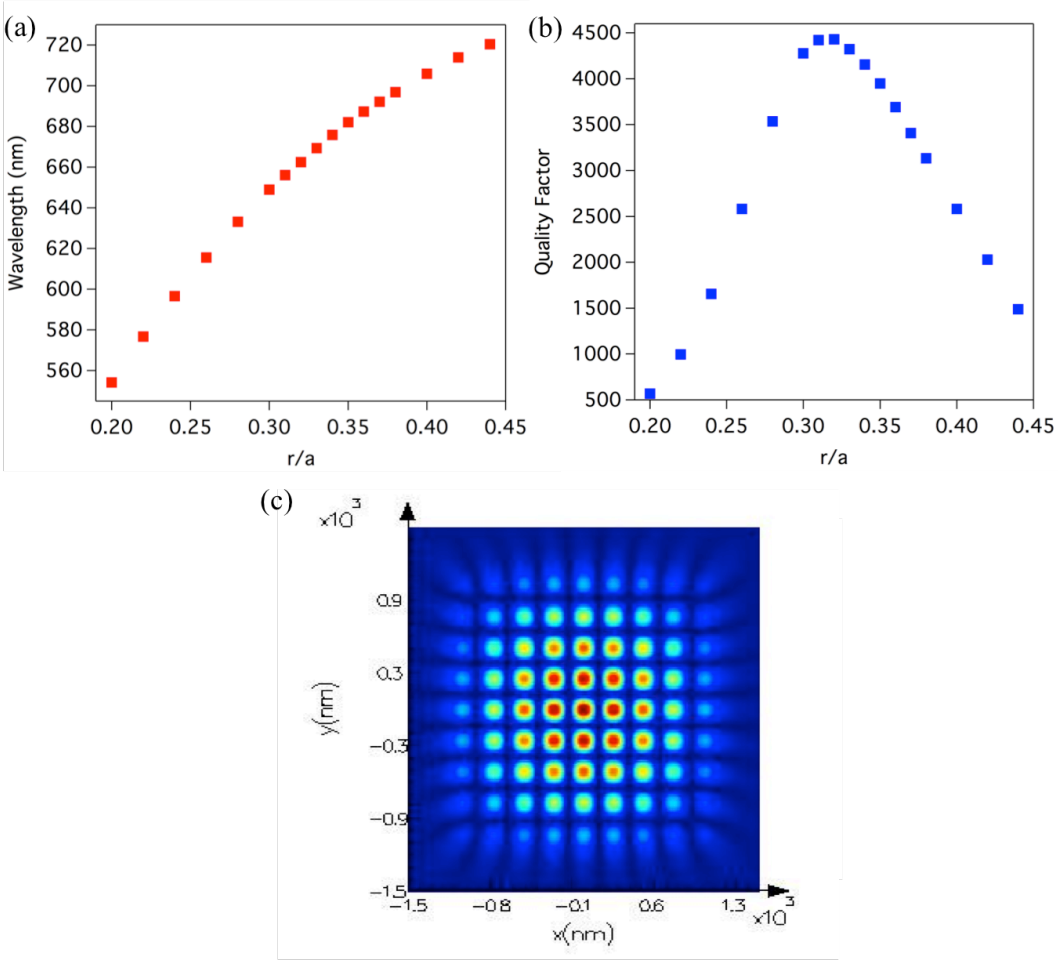

Figure 5.19: 2D FDTD simulations of 9x9 ZnO pillar photonic crystals in air. For all simulations a=250nm. (a) Plot of the wavelength of the mode versus r/a. (b) Plot of the quality factor versus r/a. (c) Plot of the band edge mode profile at λ=662.5nm of a photonic crystal with r=80nm and a=250nm.

Two-dimensional FDTD simulations of a 9x9 square array of circular pillars in air for a range of r/a values are shown in Figure 5.19. For these simulations the pitch was fixed at 250nm. As this is a 2D simulation, the pillars can be thought of being infinitely long. Figure 5.19(a) shows a plot of the wavelength of the band edge mode as the radius of the pillars is varied. A red shift in the wavelength of the mode is observed with increasing r/a values. The quality factor of the mode was calculated for the different photonic crystal arrangements and

can be seen in Figure 5.19(b). For small r/a values (0.2) and large r/a values (0.46) the quality factor is quite low, ~500 and ~1500 respectively. There is however a small range of r/a values centered at about 0.32 where the quality factor is found to be approximately 4500. Figure 5.19(c) shows the mode profile of the band edge mode for the photonic crystal with r=80nm and a=250nm. The band edge mode is spread out over the entirety of the pillars with the strongest intensity in the center of the array and decays towards the edges of the photonic crystal.

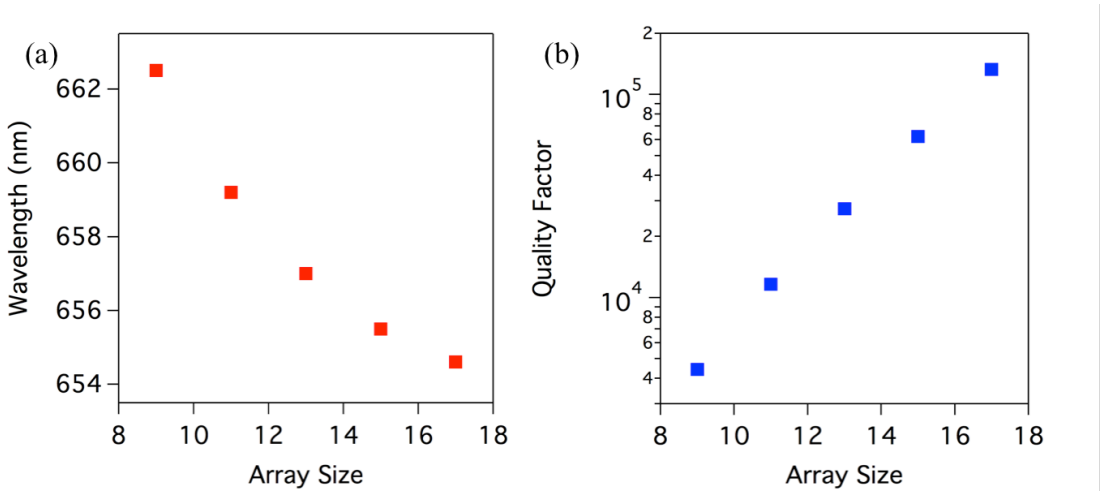

Figure 5.20: 2D FDTD simulations of (a) the wavelength and (b) the quality factor of the band edge mode in ZnO pillar photonic crystals (r=80nm, a=250nm) in air with changing array size.

While the simulations in Figure 5.19 were for a 9x9 array of circular pillars, the effect of increasing the size of the array is shown in Figure 5.20. The photonic crystals simulated in Figure 5.20 had a radius of 80nm and pitch of 250nm. Increasing the size of the array causes a small change in the wavelength at which the band edge mode occurs. More significantly however, is the dramatic increase in the quality factor of the mode with increasing array size. When more pillars are added to the photonic crystal array one can

think of this as adding additional mirrors to a cavity due to the total internal reflection that takes place in the square array pillar photonic crystal. It is therefore expected that increasing the size of the array will lead to light being more easily confined in the photonic crystal resulting in higher quality factors. For a 17x17 array of infinitely tall ZnO pillars, the quality factor was found to be approximately 130,000. Figure 5.21 shows the mode profiles for the 9x9, 13x13, and 17x17 arrays of ZnO pillars. The mode profiles spread out across the array of pillars regardless of how large the array is.

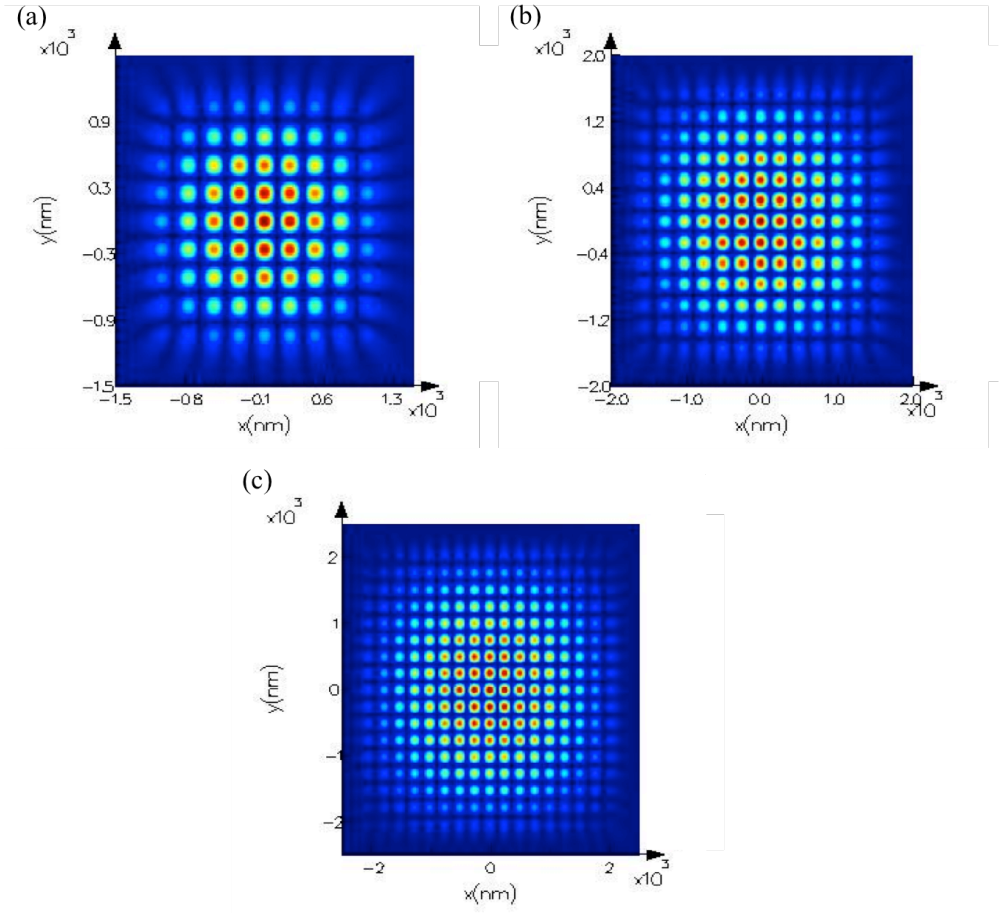

Figure 5.21: Mode profiles of the band edge mode in (a) 9x9, (b) 13x13, and (c) 17x17 arrays of infinitely tall, circular ZnO photonic crystals in air where r=80nm and a=250nm. The mode profiles are at λ=662.5nm, λ=657.0nm, and λ=654.6nm respectively.

The 2D simulations of the ZnO photonic crystals give an idea of the modes and quality factors of the modes that would be expected in the devices. Real devices however, are not infinitely tall and it is therefore more accurate to simulate 3D structures. Figure 5.22 compares the results obtained using 2D, infinitely tall pillars previously shown in Figure 5.19, to 3D fixed aspect ratio pillars. The aspect ratio of a pillar is defined as the height of the pillar divided by its width. For the 3D simulations the aspect ratios of the pillars were fixed at 20 and the pitch was 250nm. The wavelengths and quality factors of the modes for the different r/a values match very well between the 2D and 3D simulations. Therefore, ZnO photonic crystals with pillar aspect ratios of 20 can be accurately simulated using less computationally demanding 2D simulations.

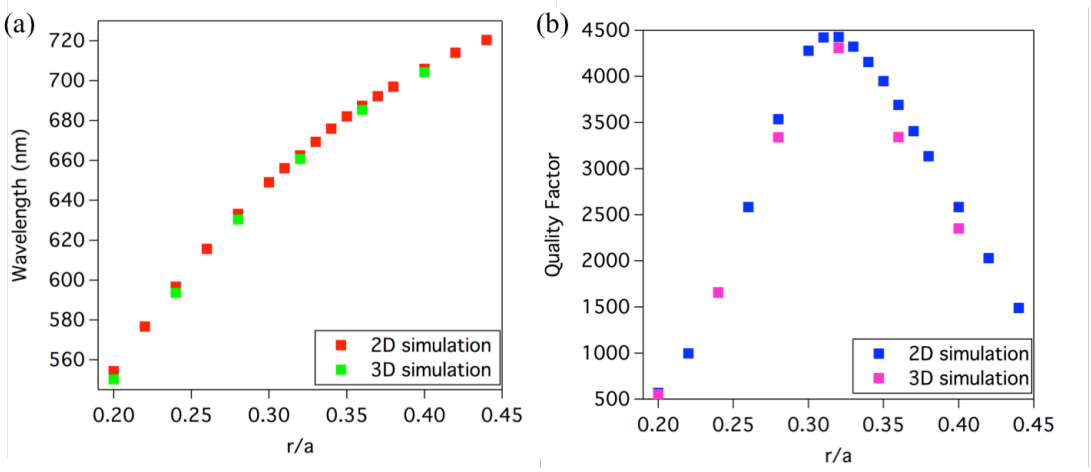

Figure 5.22: Comparison between 2D and 3D FDTD simulations of circular pillar ZnO photonic crystals in air. (a) Plot of the wavelengths versus r/a. (b) Plot of the quality factors versus r/a. All photonic crystals had a pitch of 250nm and pillars in the 3D simulations had fixed aspect ratios of 20.

Top-down fabrication of high aspect ratio pillars is difficult and often leads to structures with non-vertical etch profiles. While the aqueous ZnO growth technique is ideal for the fabrication of high aspect ratio structures, simulations were performed to determine

the aspect ratios of the pillars needed in photonic crystals to achieve cavities with the highest quality factors. Figure 5.23(a) shows the wavelength of the band edge mode in 9x9 arrays of ZnO photonic crystals with pillar aspect ratios ranging from 2 to 20. In photonic crystals with a pitch of 250nm, pillar aspect ratios between 2 and 20 correspond to pillars with heights between 3.2μm and 0.32μm. Figure 5.23(b) shows the corresponding quality factors for the band edge mode in each of the photonic crystals. Photonic crystals containing pillars with aspect ratios of approximately 10 and above have similar mode quality factors to the corresponding 2D infinite pillar photonic crystals simulated. Decreasing the aspect ratio of the pillars in these cavities has a significant effect on both the wavelength of the mode and the quality factor as seen in Figure 5.23. As is clear from Figure 5.23(a), the wavelength of the mode can change by almost 100nm depending on the aspect ratio of the pillars in the photonic cavity. Figure 5.23(b) shows that while photonic crystals containing pillars with aspect ratios between 10 and 20 have quality factors around 4000, photonic crystals with pillars with an aspect ratio of 2 have a quality factor of about 600.

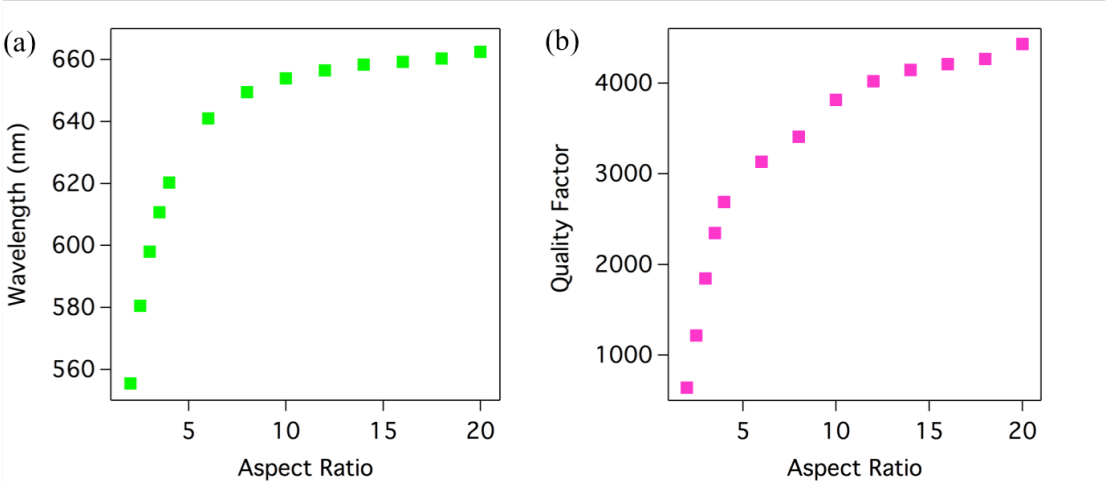

Figure 5.23: FDTD simulations of 9x9 arrays of circular ZnO pillar photonic crystals with aspect ratios ranging from 2 to 20. (a) Plot of the wavelength of the band edge mode versus the aspect ratio of the pillars in the photonic crystal. (b) Plot of the quality factor of the modes versus the aspect ratio of the pillars in the photonic crystal. All photonic crystal pillars had r=80nm and a=250nm (r/a=0.32).

Cross sections of the mode profiles in ZnO pillar photonic crystals with pillar aspect ratios of 20, 14, 8, and 6 are shown in Figure 5.24. In these photonic crystals with r=80nm and a=250nm this corresponds to pillars with heights of 3.2μm, 2.24μm, 1.28μm, and 0.96μm. In the cavities with higher aspect ratio pillars, it is evident from the mode profiles in Figure 5.24 that the mode is contained in the pillars. As the aspect ratio is decreased, the mode begins to leak from both ends of the pillars leading to the lower quality factors. While this series of simulations varied only the aspect ratios, the observed trend of quality factor with aspect ratio also applies to photonic crystals with pillars of other radii and pitches.

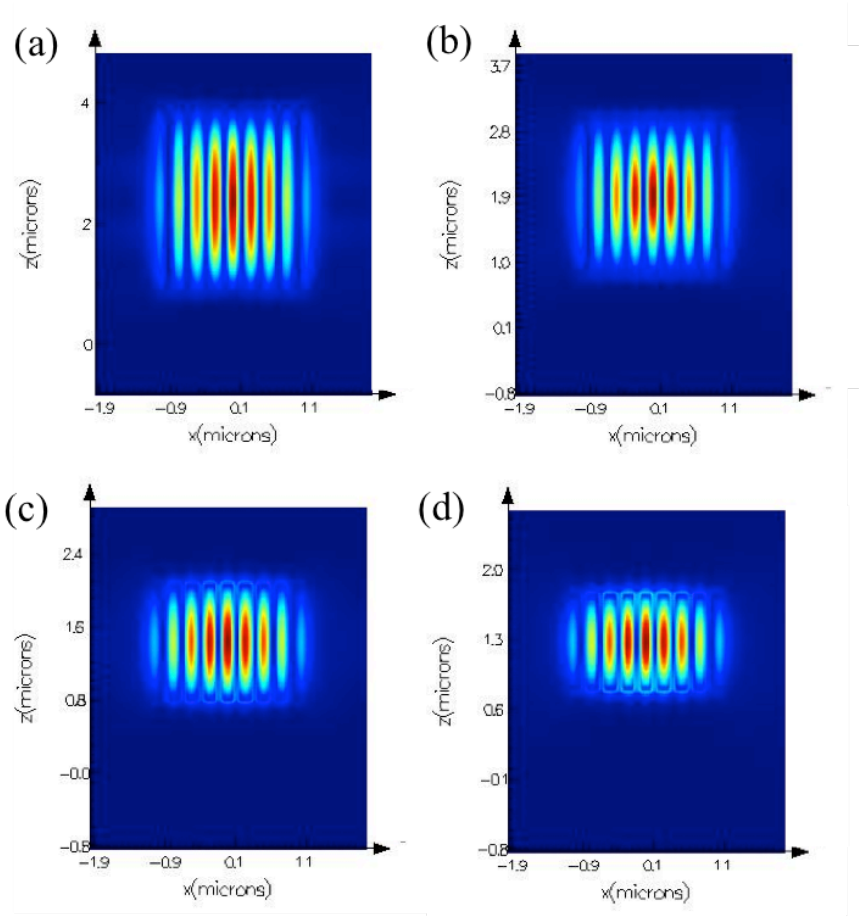

Figure 5.24: Cross-section mode profiles, taken through the center of the device, of circular ZnO pillar photonic crystals with pillar aspect ratios of (a) 20, (b) 14, (c) 8, and (d) 6 at λ=662.5nm, λ=658.4nm, λ=649.5nm, and λ=641.0nm. All of the photonic crystals were 9x9 arrays of 80nm radius pillars with a pitch of 250nm.

The crystalline structure of ZnO leads to growth of predominately hexagonal shapes as seen throughout this chapter. Unconstrained growth of ZnO photonic crystal pillars will therefore also have a hexagonal shape. Three-dimensional simulations of hexagonal ZnO pillar photonic crystals in air with pillar aspect ratios equal to 20 and a pitch of 250nm are shown in Figure 5.25. The radius for hexagonal structures was measured as shown in the inset of Figure 5.25(a). Similar to the circular pillar photonic crystals, a shift in the wavelength of the band edge mode with r/a value is observed. In addition, the quality factor,

as can be seen in Figure 5.25(b), has a maximum value of 4260 for pillars with a radius to pitch of 0.36. Changing the r/a value from 0.36 results in a drop in the quality factor. The wavelength of the mode can however be shifted, while maintaining the high quality factor, by fixing the r/a value to 0.36 and adjusting the absolute radius and pitch values. The quality factors found by simulations for both circular and hexagonal pillar photonic crystals are quite close due to the similar amounts of material making up the pillars in both cases.

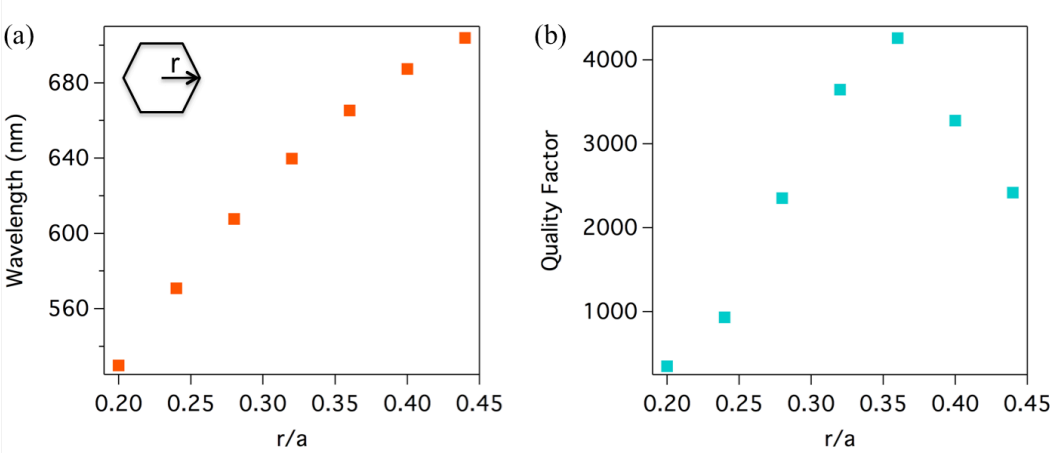

Figure 5.25: FDTD simulations of three-dimensional, hexagonal ZnO pillar photonic crystals in air consisting of 9x9 pillars. Pillar aspect ratios= 20 and a=250nm. (a) Plot of wavelength versus r/a values. The insert shows how the radius was measured for the hexagonal pillars. (b) Plot of the quality factor versus r/a pillar values.

Hexagonal pillar photonic crystal cavities in air were further studied by simulating the change in both the expected wavelength and quality factor for different pillar aspect ratios. Figure 5.26 compares the wavelength and quality factors simulated for circular and hexagonal pillar 9x9 square array cavities with r/a=0.32. The two different shaped pillars show similar trends for both the mode wavelength and quality factor. A dramatic drop in the quality factor for photonic crystals was observed for pillar aspect ratios smaller than 8. The slightly lower wavelength and quality factors for the hexagonal pillars are attributed to the r/a

value of 0.32 used in these simulations, which is ideal for the circular pillars, instead of a r/a value of 0.36, which is ideal for hexagonal pillars.

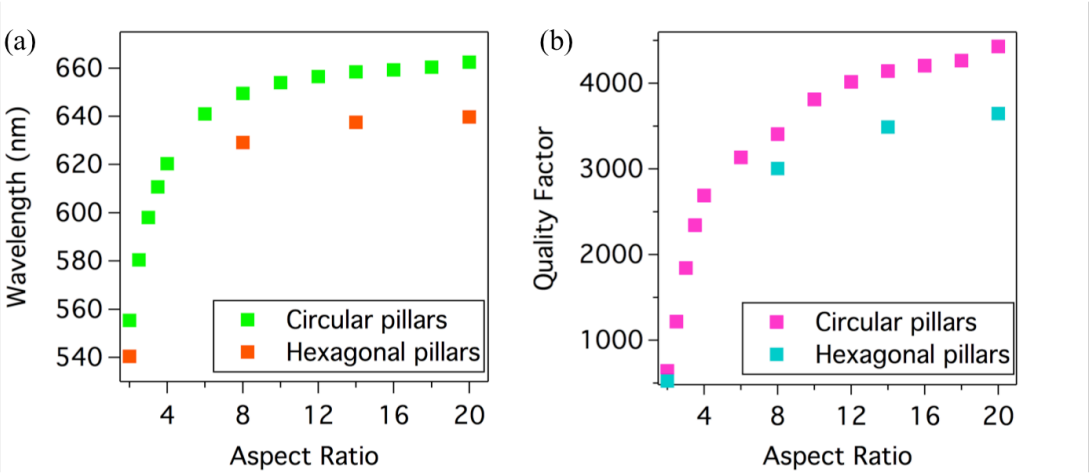

Figure 5.26: FDTD simulations of ZnO photonic crystals consisting of a 9x9 array of pillars with r=80nm and a=250nm. Comparison of the (a) wavelength and (b) quality factors versus pillar aspect ratios for photonic crystals consisting of circular and hexagonal pillars.

The simulations presented so far have all been of photonic crystals surrounded by air. While these simulations give an idea of the cavity behavior they are not entirely realistic, as the pillars making up the photonic crystal need to be grown on a substrate. The substrate used for ZnO growth is spinel ($MgAl_2O_4$) with a refractive index of 1.7. Simulations of photonic crystals consisting of a 9x9 array of circular ZnO pillars, with a=250nm, on a thick spinel substrate are shown in Figure 5.27. A similar shift in the wavelength of the band edge mode versus r/a pillar value is observed as with the photonic crystals suspended entirely in air. The most significant change however, can be seen in Figure 5.27(b). A maximum quality factor of ~2700 is found for a photonic crystal on a spinel substrate compared to a maximum quality factor of ~4300 for a photonic crystal suspended in air. The r/a value at which this largest quality factor in the devices occurs also shifts from 0.32 for pillars in air to 0.36 when the pillars are on a spinel substrate. A more accurate comparison is to look at the

simulated quality factor for a fixed r/a value in both cases. Throughout the remainder of this chapter, all photonic crystals consisting of circular pillars will have r=90nm and a=250nm (r/a=0.36), as this was found to be the optimal ratio for the devices on a substrate. The quality factors of the circular pillar photonic crystals in air and on spinel, with r/a=0.36, are ~3400 and ~2700 respectively.

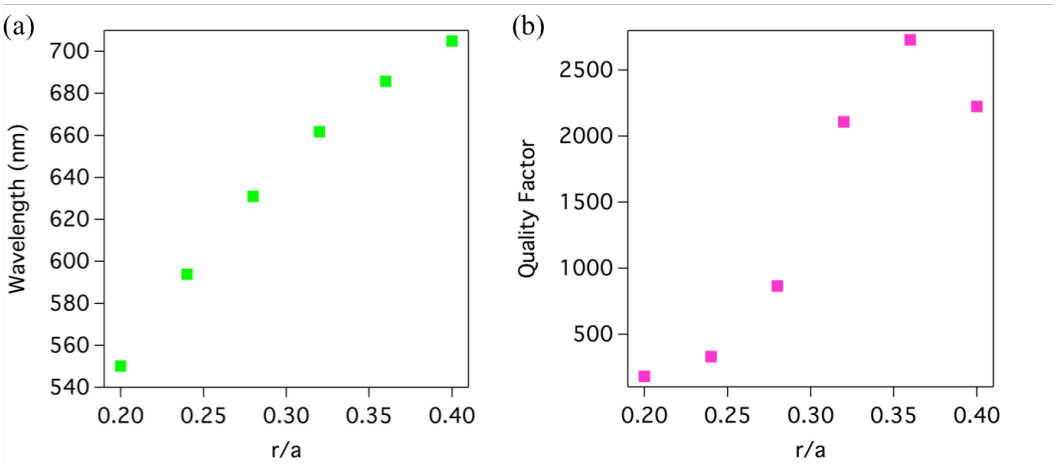

Figure 5.27: FDTD simulations of three-dimensional, circular ZnO pillar photonic crystals on a thick spinel substrate consisting of 9x9 pillars. Pillar aspect ratios= 20 and a=250nm. Plots of (a) wavelength and (b) quality factor versus r/a pillar values.

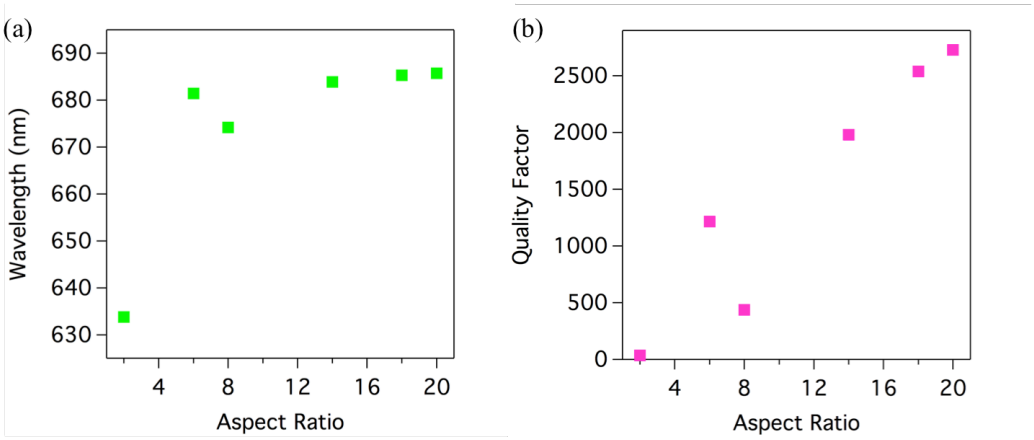

Figure 5.28: FDTD simulations of ZnO photonic crystals on spinel consisting of a 9x9 array of circular pillars with r=90nm and a=250nm. Plot of (a) the wavelength and (b) the quality factor versus pillar aspect ratios for the photonic crystals.

The aspect ratio of the circular pillars forming the photonic crystals on spinel substrates was varied to study the effect on the band edge mode wavelength and quality factor, as shown in Figure 5.28. In Figure 5.28(a) it can be seen that the wavelength at which the mode in the photonic crystal occurs stays relatively the same as the aspect ratio of the pillars is varied. Only at the smallest aspect ratio simulated is there a significant (~50nm) change in the band edge mode wavelength. As can be seen in Figure 5.28(b), the quality factor of the mode however, decreases as the aspect ratio of the pillars forming the photonic crystal decreases. Photonic crystals consisting of pillars with aspect ratios of 20 have quality factors of ~2700, while photonic crystals consisting of pillars with an aspect ratios of 6 have a quality factor of ~1200.

Mode profiles of the x-z cross-sections of the photonic crystals are shown in Figure 5.29 with pillar aspect ratios of 20, 14, and 6, corresponding to pillar heights in this specific case of 3.6μm, 2.52μm, and 1.08μm respectively. In all of the mode profiles, leaking of the mode into the spinel substrate is observed, as is expected given the decrease in the quality factor for photonic crystals on spinel. Photonic crystals formed of pillars with smaller aspect ratios show more leakage of the mode into the spinel substrate than pillars with larger aspect ratios. It is therefore important for photonic crystals grown on spinel substrates to have pillars with as large aspect ratios as possible to observe the most well-confined modes.

Growth of ZnO structures directly onto spinel ($MgAl_2O_4$) substrates has proven to be quite difficult. Therefore, a thick base layer of single crystalline ZnO is grown on top of the spinel substrate to aid in device growth. Results from simulations of circular pillar photonic crystals (r=90nm, a=250nm, and aspect ratio=20) with different ZnO base layer thicknesses between 2μm and 50nm are shown in Figure 5.30. Changing the thickness of the base layer

has little effect on the wavelength at which the mode occurs. In addition, the quality factor of photonic crystals consisting of pillars on a base layer of ZnO is found to stay the same, between about 650-750 for most ZnO base layer thickness. Only when the base layer is 50nm thick does quality factor increase to ~1800.

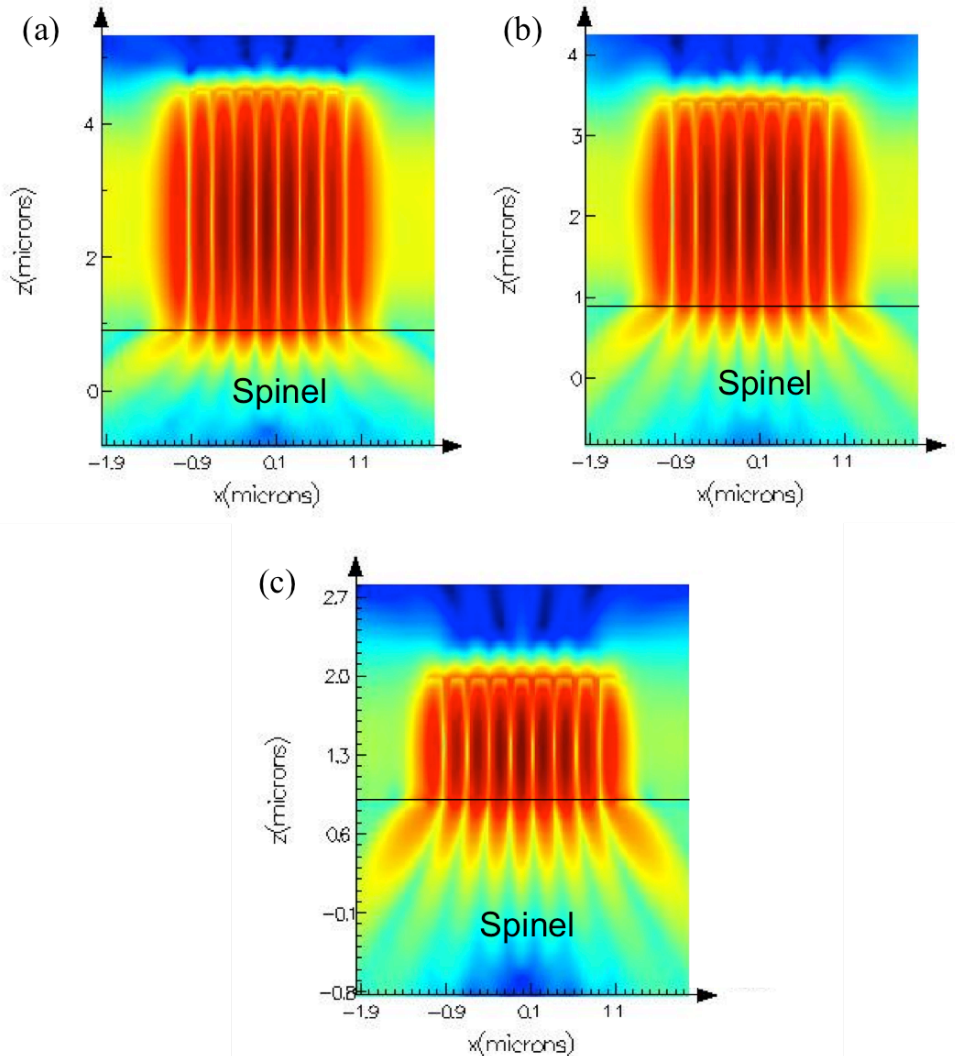

Figure 5.29: Cross-section mode profiles, taken through the center of the device, of circular ZnO pillar photonic crystals on a thick spinel substrate with pillar aspect ratios of (a) 20, (b) 14, and (c) 6 at λ=685.7nm, λ=683.9nm, and λ=681.4nm respectively. All of the photonic crystals were 9x9 arrays of 90nm radius pillars with a pitch of 250nm. The black line indicates the upper boundary of the spinel substrate.

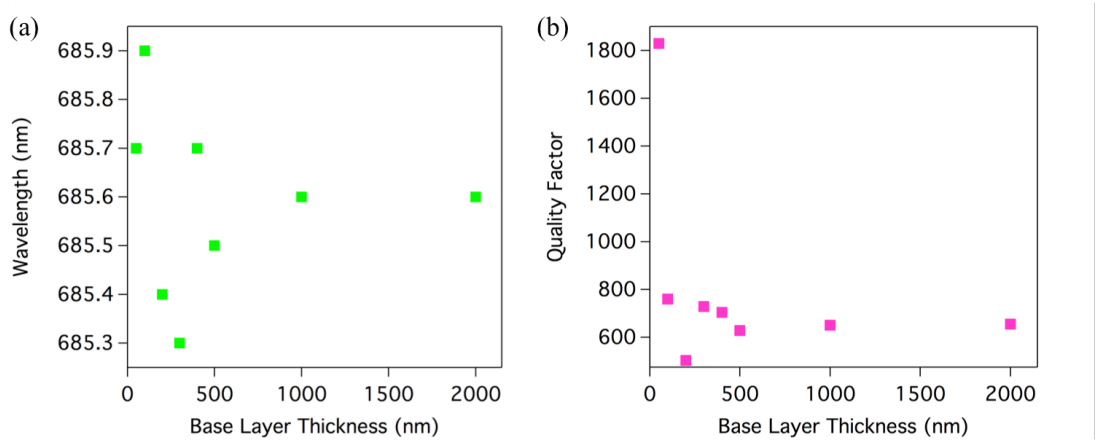

Figure 5.30: FDTD simulations of three-dimensional, circular ZnO pillar photonic crystals on a ZnO base layer on top of a thick spinel substrate. Plots of (a) wavelength and (b) quality factor versus ZnO base layer thickness. Photonic crystals consist of 9x9 array of pillars with pillar radius= 90nm and pitch= 250nm.

To further investigate the effect of growing the ZnO pillars directly on the ZnO base layer, cross-section photonic crystal mode profiles were simulated for ZnO base layer thicknesses of 2μm and 50nm, as shown in Figure 5.31. The photonic crystals in both cases are identical. Significant leaking of the mode into the ZnO base layer is apparent for both base layer thicknesses. When the base layer is 2μm thick, shown in Figure 5.31(a), most of the mode leaks directly into the ZnO base layer region and very little into the spinel substrate. In Figure 5.31(b) where the base layer is only 50nm thick, the mode leaks into the thin base layer as well as the spinel substrate. This case more closely approximates the scenario where the pillars are placed directly onto the spinel substrate and therefore, as is observed, the quality factor is higher. Placing the photonic crystal structure directly onto the ZnO base layer dramatically reduces the quality factor. Even on a 50nm thick base layer, the quality factor is reduced by a third compared to the case of a photonic crystal placed directly on spinel.

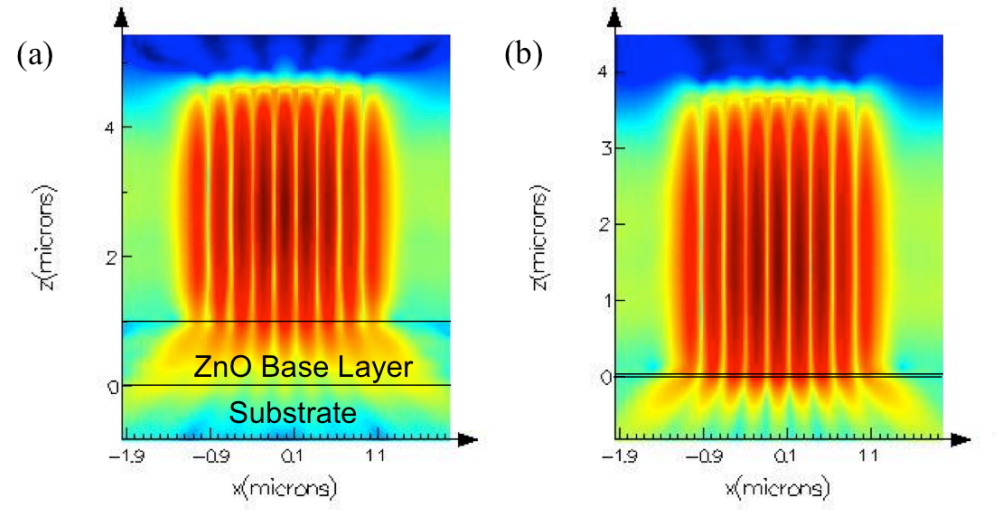

Figure 5.31: ZnO photonic crystal (r=90nm, a=250nm, aspect ratio=20, and 9x9 array of pillars) cross-sections showing mode profiles for pillars grown on a (a) 2μm and (b) 50nm ZnO base layer. The cross section is taken through the center of the device. The base layer is simulated on top of a thick spinel substrate. ZnO base layer and spinel substrate regions are denoted with the black lines.

The fabrication of 50nm ZnO base layers using our aqueous growth method is not possible and therefore, alternative methods to increase the quality factors of the devices are needed. Increasing the number of pillars in the photonic crystal array was previously shown to increase the quality factor of the device. Only a small improvement in the quality factor is observed in photonic crystals consisting of more pillars as shown in Figure 5.32. Even when the pillar array size is increased to as high as 18x18, the quality factor of the simulated photonic crystal is ~850. Therefore, fabricating ZnO pillar photonic crystals directly on the ZnO base layer is not a viable option for a high quality factor ZnO cavity.

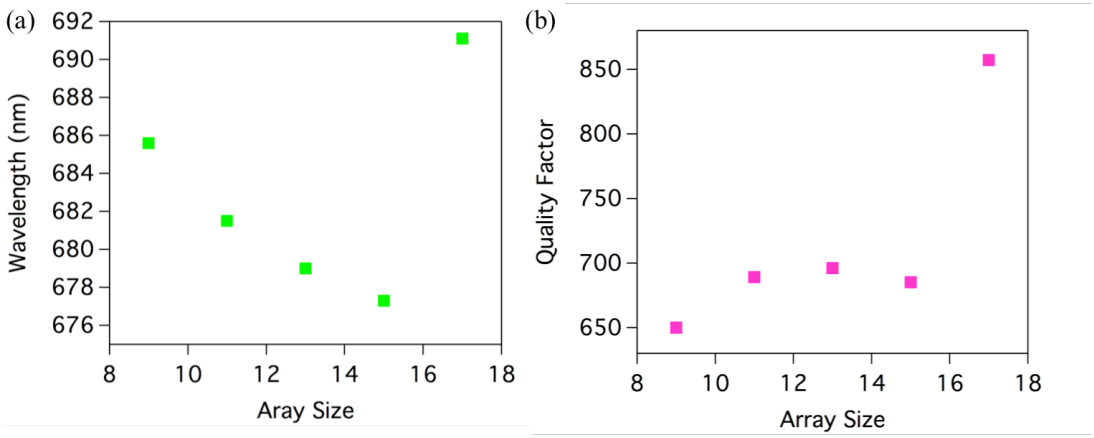

Figure 5.32: FDTD simulations of the (a) wavelength and (b) quality factor of three-dimensional circular pillar photonic crystals of different array sizes. All photonic crystals consisted of pillars with r=90nm, a=250nm, and aspect ratio=20.

One of the main advantages of our growth technique for the fabrication of photonic crystals is the ability to constrain the ZnO growth for a region and then allow the material to grow unconstrained. Pillars grown directly on the ZnO base layer are not ideal for photonic crystals as seen in Figure 5.30 and Figure 5.31. If however, the constrained growth region forms a post for the ZnO pillars, as shown in Figure 5.33, much higher quality ZnO photonic crystals are possible.

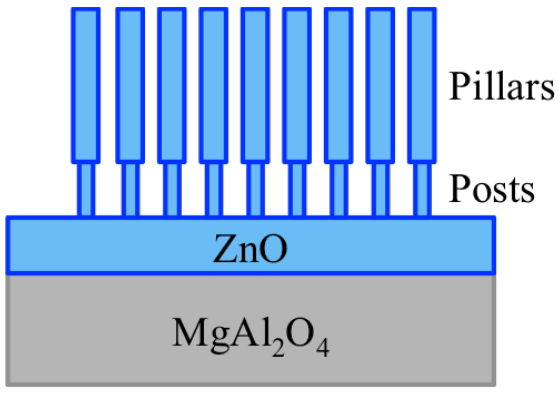

Figure 5.33: Schematic drawing from the side of a ZnO photonic crystal with each pillar of the crystal on a ZnO post. The posts are on top of a ZnO base layer and spinel substrate.

Figure 5.34 shows the simulated quality factors for ZnO circular pillar photonic crystal cavities with different post radii. A 1μm thick base layer of ZnO on top of a thick layer of spinel was used as the substrate. The circular posts had radii between 20nm and 90nm, heights of 500nm, and a pitch of 250nm. The circular pillars had radii of 90nm, a pitch of 250nm, and aspect ratios equal to 20. The simulated quality factors (~3400) of the photonic crystal remain relatively unchanged for devices with post radii between 20nm and 70nm. In addition, these quality factors are the same as those measured for circular pillars in air, indicating that placing the pillars on posts allows for devices with the best quality factors possible. Increasing the post radius to 80nm causes a slight decrease in the quality factor to ~2900 however, this is still greater than the quality factors simulated for pillar photonic crystal cavities on spinel or ZnO base layers. The large decrease in the quality factor of the photonic crystal with post radii equal to 90nm, which is also the pillar radii, is due to the fact that the simulation is of a photonic crystal directly on a base layer.

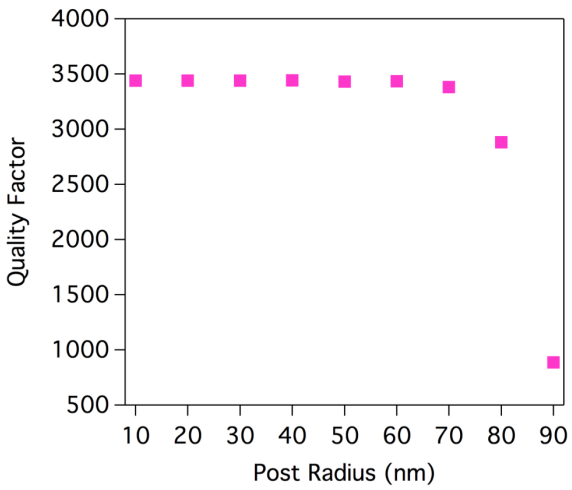

Figure 5.34: FDTD simulations of the quality factor of ZnO pillar photonic crystals on ZnO posts with different post radii. The circular posts were 500nm tall and with a pitch of 250nm. The pillars were circular with r=90nm, a=250nm, and aspect ratio=20. The substrate for the simulations was a 1μm thick base layer of ZnO on top of a thick layer of spinel.

Cross-section mode profiles in the x-z direction through the center of the ZnO pillar photonic crystals are shown in Figure 5.35 for post radii equal to 30nm, 50nm, 70nm, and 80nm. The pillar, post, base layer, and spinel substrate layer are indicated on each mode profile image. In Figure 5.35(a) and Figure 5.35(b) where the post radii are 30nm and 50nm respectively, the band edge mode is highly confined to the pillar region. When the post radius is equal to 70nm, as seen in Figure 5.35(c), some of the mode is beginning to leak into the post regions of the structure. Increasing the post radius further to 80nm, as shown in Figure 5.35(d), causes significant leaking of the mode into the ZnO posts and base layer, therefore causing the decrease in quality factor observed. These simulations indicate that high quality factor ZnO photonic crystals can be fabricated by placing the pillars on posts. In addition, the difference in the radius between the posts and pillars can be as small as 10nm to 20nm to still have a photonic crystal with a well-confined band edge mode.

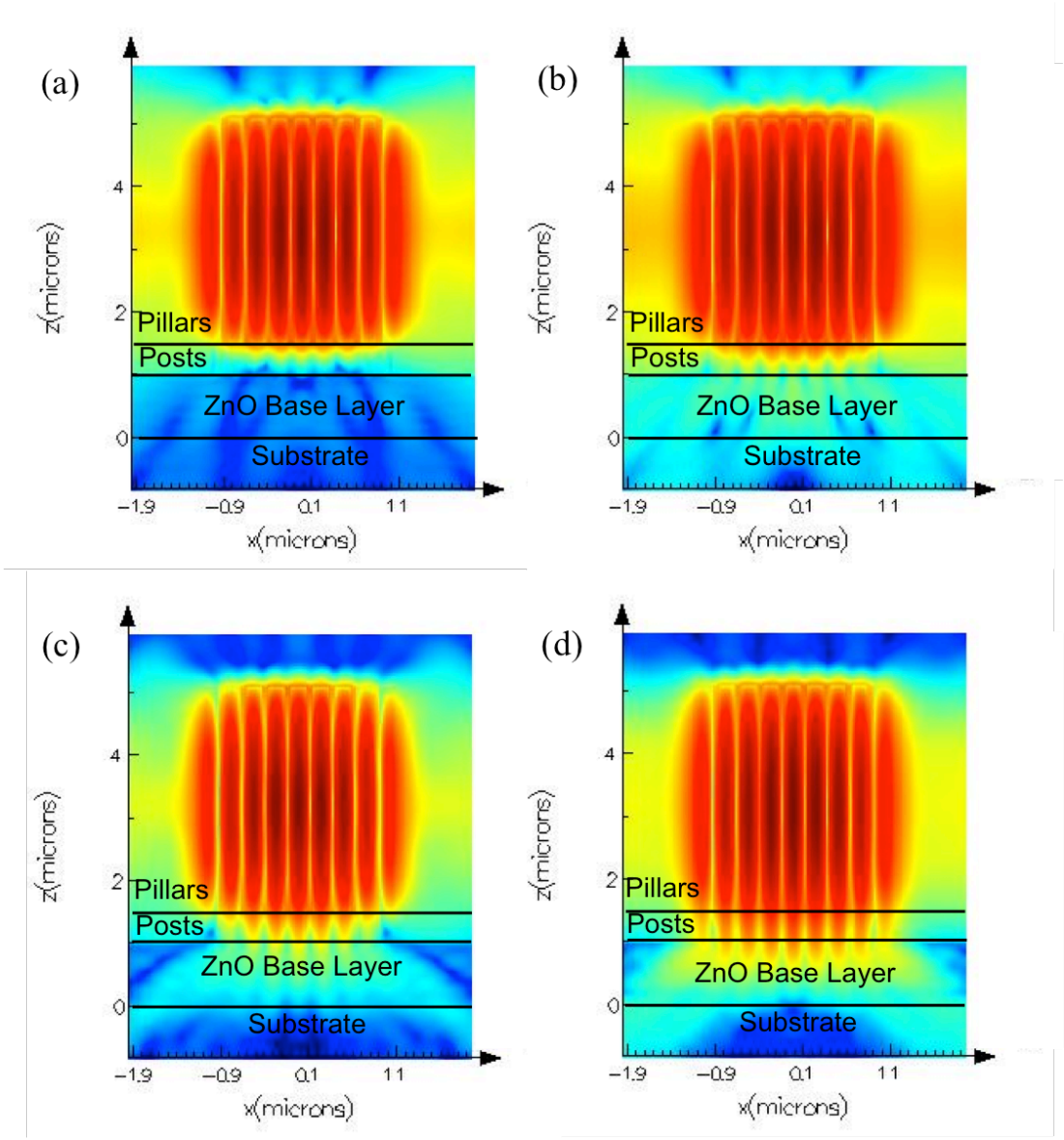

Figure 5.35: FDTD ZnO photonic crystal cross-section mode profiles at λ=685.6nm for 9x9 array of pillars grown on posts with (a) post radius=30nm, (b) post radius=50nm, (c) post radius=70nm, and (d) post radius=90nm. The cross section is taken through the center of the device. The ZnO pillars have r=90nm, a=250nm, and aspect ratio=20. The ZnO posts are 500nm tall with a=250nm. The posts are on a 1μm thick base layer of ZnO on top of a thick layer of spinel. ZnO pillars, posts, base layers and spinel substrate regions are denoted with the black lines and labeled.

Most of the structures grown throughout this chapter are hexagonal due to the crystalline symmetry of the ZnO material. Therefore, the photonic crystals grown, which will presented later in this chapter, have constrained posts regions, which are circular, and unconstrained pillars, which are hexagonal. Similar simulations to those shown in Figure 5.34 were done for hexagonal pillars rather than circular pillars. The results are presented in Figure 5.36 and show a similar trend to that seen for the circular pillars. The quality factor for hexagonal pillars in air with r=90nm, a=250nm, and aspect ratios=20 was previously found to be ~4260. Simulations of hexagonal pillar photonic crystals on posts with radii up to 60nm showed very similar quality factors. Increasing the post radius to 70nm decreased the quality factor by approximately 15% to ~3650, which is still higher than that for ZnO pillars directly on the base layer or on the spinel substrate. Quality factors for the ZnO photonic crystals on posts that are similar to those in air are possible because the post region of the structures has a different effective refractive index than the pillar region. This difference in the refractive indices isolates the mode in the pillar region for structures where there is as small as a 10nm difference between the post and pillar radii.

The hexagonal ZnO pillar photonic crystals were further characterized by changing the aspect ratio of the pillars and the height of the posts. Figure 5.37 shows the quality factors for photonic crystals consisting of hexagonal pillars with different aspect ratios. In these simulations the pillar radius was fixed at 90nm and the height of the pillar was varied between 3.6μm and 0.36μm. Photonic crystals with hexagonal pillars with larger aspect ratios, above 10, showed only small differences in quality factors. As the hexagonal pillar aspect ratio was decreased below 10, a dramatic drop in the quality factor was observed.

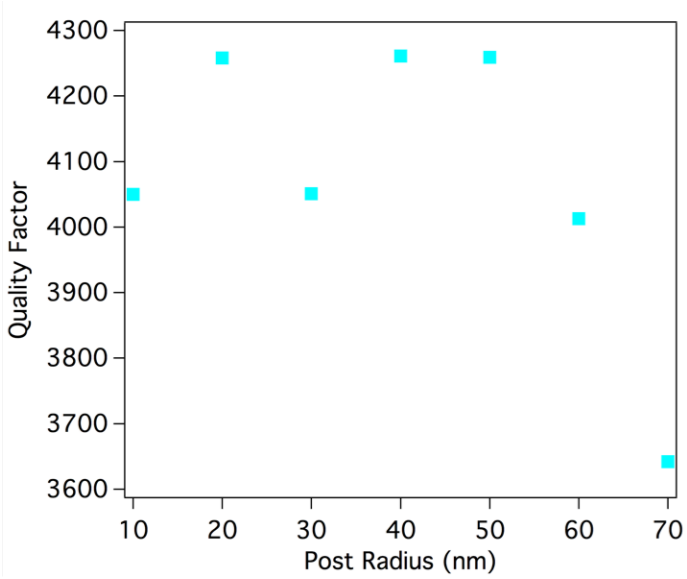

Figure 5.36: FDTD simulation of the quality factor of ZnO hexagonal pillar photonic crystals on ZnO posts with different post radii. The circular posts were 500nm tall and with a pitch of 250nm. The pillars were hexagonal with r=90nm, a=250nm, and aspect ratio=20. The substrate for the simulations was a 1μm thick base layer of ZnO on top of a thick layer of spinel.

Lastly, the post height was varied between 50nm and 500nm as shown in Figure 5.38. The quality factor of the band edge mode in the photonic crystal, which consists of a 9x9 array of hexagonal pillars, decreases as the post radius decreases and the pillars are brought closer to the ZnO base layer. It can be seen that for post heights of 400nm and above for the structures simulated in Figure 5.38 that the quality factor begins to level off at the value simulated for the photonic crystals in air. The quality factors for photonic crystal structures with post heights of 500nm, 200nm, and 50nm are approximately 4000, 3200, and 1400 respectively.

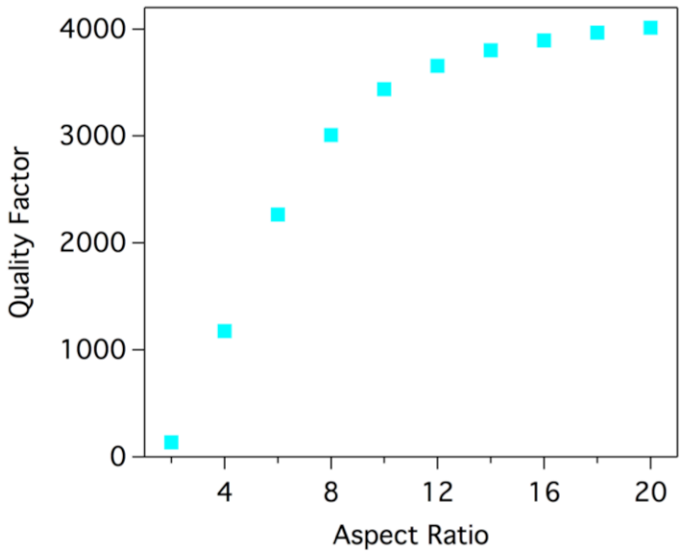

Figure 5.37: FDTD simulation of the quality factor of ZnO hexagonal pillar photonic crystals on ZnO posts with different pillar aspect ratios. The circular posts were 500nm tall with r= 90nm and a= 250nm. The pillars were hexagonal with r=90nm and a=250nm. The substrate was a 1μm thick base layer of ZnO on top of a thick layer of spinel.

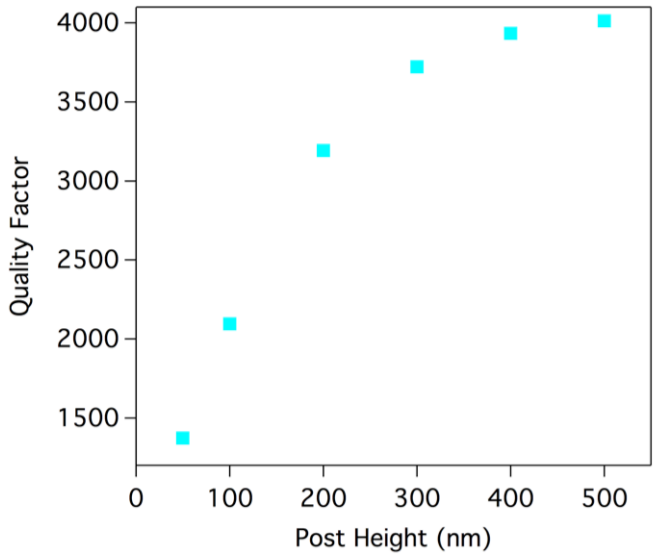

Figure 5.38: FDTD simulation of the quality factor of ZnO hexagonal pillar photonic crystals on ZnO posts with different post heights. The circular posts had r= 90nm and a= 250nm. The pillars were hexagonal with r=90nm, a=250nm, and aspect ratios=20. The substrate was a 1μm thick base layer of ZnO on top of a thick layer of spinel.

All of the simulations in this chapter have led to a detailed understanding of the optimal size, shape, and structure for ZnO photonic crystals consisting of square arrays of pillars. Keeping in mind the aqueous growth method used to fabricate ZnO structures, the optimal design for the photonic crystals is to grow them on posts. By doing so the optical modes are highly confined to the pillar regions and high quality factor devices have been simulated. In addition if the pillars and posts have sufficiently different radii, quality factors similar to those simulated with the devices in air are seen.

ZnO pillar photonic crystals have been fabricated using the aqueous growth method detailed in Chapter 2.4. Precise patterning of the PMMA molds, in which the post regions of the photonic crystal structures will grow, is made possible by using e-beam lithography. Two different growth solutions were used to fabricate the photonic crystals, one with citrate which created short pillars on the ZnO base layer and one without citrate which created tall pillars on posts.

The first growth solution consisted of 0.2g of zinc nitrate hexahydrate, 0.05 g of sodium citrate tribasic dehydrate, 1.25mL of 15M ammonium hydroxide, and 24mL of deionized water. A variety of photonic crystals were grown for 1 hour and 50 minutes from mold openings with different radii and pitches. The photonic crystals grown using this growth solution with citrate resulted in structures a few hundred nanometers taller than the PMMA resist as can be seen in Figure 5.39. To try and fabricate taller structures another sample was grown for a longer time however, the overgrown ZnO fused together. Therefore, the growth solution with citrate is ideal for creating pillar photonic crystals directly on a substrate. Currently, structures can only be grown on a base layer of ZnO but previously shown simulations indicated that such devices would have very low quality factors. In the

future, it may be possible to fabricate ZnO pillars directly on the spinel layer, which would increase the quality factor. In addition, it was found that spinning additional layers of PMMA onto the samples resulted in molds as tall as 1μm. Growth of ZnO pillar photonic crystals through these taller molds would result in pillars with higher aspect ratios and thus higher quality factors.

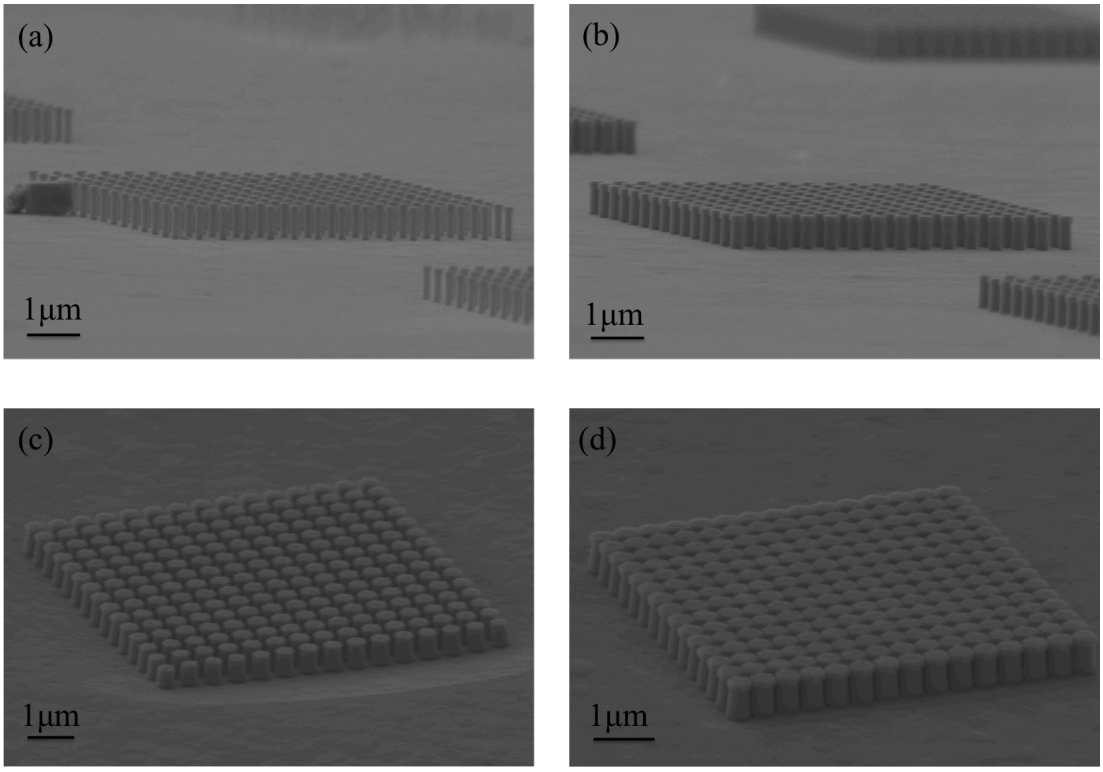

Figure 5.39: SEM images of ZnO photonic crystals grown for 1 hour and 50 minutes through molds with (a) r=50nm and a=500nm, (b) r=90nm and a=500nm, (c) r=150nm and a=550nm, and (d) r=150nm and a=450nm. All photonic crystals are grown on a thick base layer of ZnO and spinel substrate. (a) and (b) are at a 5° tilt and (c) and (d) are at a 25° tilt.

The second growth solution consisted of 0.2g of zinc nitrate hexahydrate, 1.25mL of 15M ammonium hydroxide, and 24mL of deionized water. Figure 5.40 shows several SEM images of photonic crystals grown for 1 hour 30 minutes and 1 hour 45 minutes through molds with holes of different radii and pitches. In contrast to the photonic crystals grown in

Figure 5.39, these photonic crystals are significantly taller due to the removal of the sodium citrate from the growth solution. In addition, the removal of sodium citrate results in slightly tapered ZnO pillars, as the vertical growth is much faster than the horizontal growth. Circular post regions, on which the hexagonal pillars grow from, as well as pillars with aspect ratios as high as 20:1, can be seen in Figure 5.40(c) and Figure 5.40(d). This figure also shows the ability to fabricate ZnO pillar photonic crystals with a range of r/a values on clearly defined posts.

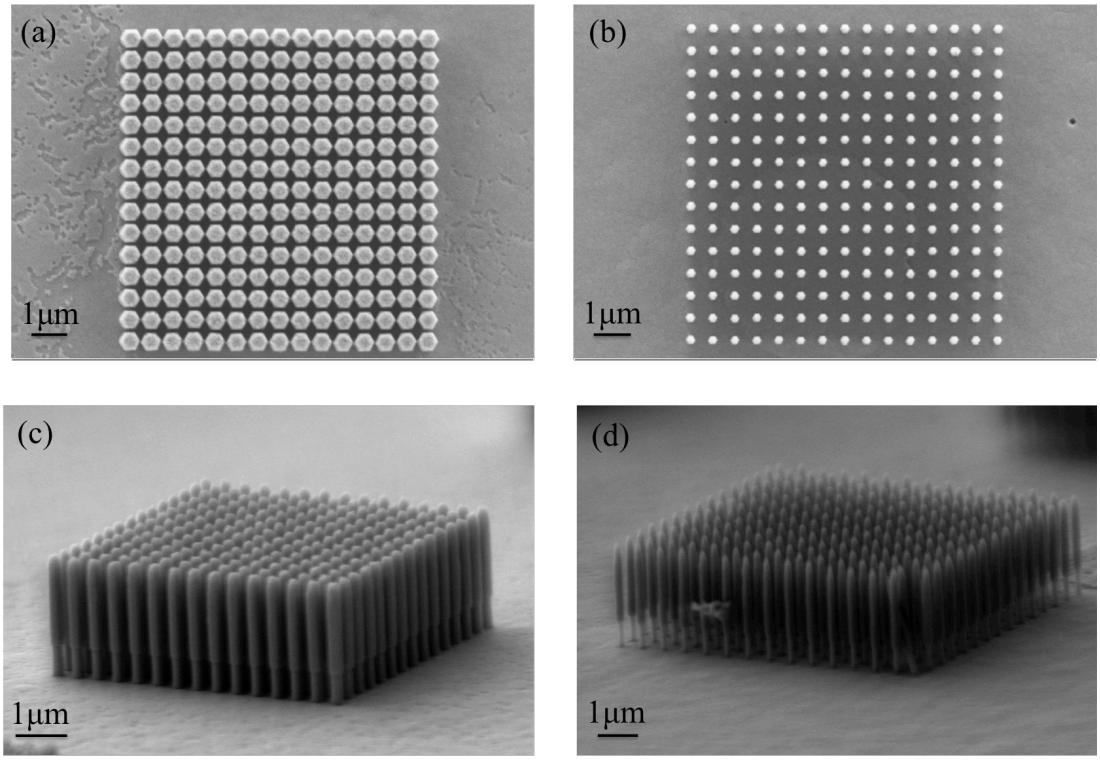

Figure 5.40: Top-down SEM images of ZnO photonic crystals grown for 1 hour and 30 minutes without citrate through molds with (a) r=210nm and a=600nm and (b) r=70nm and a=600nm. SEM images taken at a 15° tilt of ZnO photonic crystals grown for 1 hour and 45 minutes without citrate through molds with (c) r=90nm and a=450nm, and (d) r=70nm and a=600nm. All photonic crystals are grown on a thick base layer of ZnO and spinel substrate.

Bottom-up growth of single crystalline ZnO pillar photonic cavities have been demonstrated in Figure 5.39 and Figure 5.40. The aqueous growth technique is an ideal

method for fabricating such structures, as it allows for control over the size, spacing, and aspect ratio of the pillars in the photonic crystal without the use of etching. This process results in vertical, crystallographically smooth sidewalls that are ideal for photonic applications. Band edge modes and quality factors of photonic crystals made from square arrays of pillars have been simulated. A promising future avenue of research would be to extend this work to fabricate devices with parameters optimized for photonic devices. This could be achieved through careful optimization of the growth solution and conditions to create photonic crystals with the appropriate ratio of radius to pitch and aspect ratio. There are many applications, such as waveguides, filters, and cavities, where the ability to fabricate high aspect ratio pillars and pillar photonic crystals is advantageous. While it has proven difficult to create high aspect ratio pillars using top-down approaches, the constrained aqueous growth methods demonstrated here overcome this fabrication limitation and are ideal for fabricating high quality devices

Chapter 6

Single Crystal ZnO Formed Epitaxially on Single Crystal Gold

6.1 Introduction and Motivation

The interface between metal and oxide or metal and semiconductor can play a critical role in the performance of electrical, plasmonic, and optical devices [226]–[229]. The ability to form an epitaxial relationship between a metal and an oxide opens the door for better electrical contacts in devices [230], enhanced plasmonic interactions at the material interface [231], [232], and the advancement of catalysts [233], [234]. In optical devices, metal-oxide interfaces are important for both the electrical injection of carriers into devices as well as for the possibility for enhanced light extraction from the device. Most metal-oxide interfaces are formed using vapor phase deposition techniques, which often result in polycrystalline materials with non-epitaxial relationships. These techniques have limitations such as the incorporation of containments at the interface and alloying of the metal with the material on which it is deposited.

The field of material interfaces has been well explored over the past several decades and has led to numerous findings and advancements. Much of the work to date has focused

on interfaces between two different semiconductors or oxide materials. This research on material interfaces has been motivated by the desire to grow heterostructures and/or deposit semiconductor layers on various substrate materials to create novel devices. Previous work has concentrated on depositing materials on nearly lattice-matched substrates or using a transitional buffer layer between materials with greater differences in their lattice constants in an attempt to create higher quality materials and minimize strain induced dislocations. Thin layers of lattice-mismatched or strained materials, below a 'critical layer thickness' can grow without the creation of defects [235], [236]. Such careful control of the growth of strained or buffer layers general require techniques such as molecular beam epitaxy, where each atomic layer of deposited material can be precisely controlled.

ZnO has been epitaxially grown on several near lattice-matched substrates including gallium nitride [52] and silicon carbide [67], where the lattice mismatch is 1.9% and 5.5% respectively. In addition, ZnO has been epitaxially grown using metalorganic chemical vapor deposition on sapphire which has a larger lattice mismatch of ~16.7% [67], [237]. While these semiconductor-semiconductor interfaces have many uses in heterostructure devices, metal-semiconductor interfaces also have a wide range of applications. Traditionally, metals are deposited on semiconductors to make electrical contacts where the interface between the materials plays an important role in determining the contact resistance. In semiconductor optoelectronic devices, metals are used to inject carriers into an optically active device or to act as a nanoantenna to enhance plasmonic effects where again the semiconductor-metal interfaces are important. The quality of the metal-semiconductor interface is therefore critical in determining the quality of the performance of the device, however, it is only in rare instances that an epitaxial metal-on-semiconductor material system

is used [238]. In those instances, the metal layer is grown epitaxially on the semiconductor. In this chapter, the low temperature, aqueous, epitaxial growth of single crystalline ZnO on single crystalline gold microplates is investigated [129]. It is demonstrated that smooth, continuous films of ZnO can epitaxially be grown on large gold microplates with a dominant epitaxial relationship of ZnO $[1\bar{1}00](0002) \parallel$ Au $[2\bar{1}\bar{1}](111)$. This relationship between the ZnO and gold has no rotation between the close packed lattices of the two materials.

In contrast to studies investigating semiconductor-semiconductor interfaces of materials with different lattice constants where the material is gradually transitioned from one to the other to avoid abrupt lattice changes, the growth of semiconductors on metals are not always possible using the same techniques. ZnO and gold have both different lattice constants and crystal structures. The crystalline structure of ZnO is typically hexagonal wurtzite with lattice constants a = b = 0.3250nm and c = 0.5207nm. The crystalline structure of gold, on the other hand, is a face-centered cubic (FCC) structure with a lattice constant a = 0.4079. The lattice mismatch between the two materials for the close-packed planes is calculated using Equation 6.1 and found to be 12.7%.

$$(a_{ZnO}\text{-}a_{Au}\frac{\sqrt{2}}{2})/(a_{Au}\frac{\sqrt{2}}{2}) = 12.7\% \quad (6.1)$$

One would think that due to this lattice mismatch between ZnO and gold that it would be a challenge to create epitaxial interfaces between these two materials. Results in this chapter, however, demonstrate a simple and powerful method for the epitaxial growth of single crystalline ZnO on single crystalline Au.

Previous work studying ZnO-Au interfaces has relied upon low temperature deposition techniques to achieve good interfaces between the materials due to differences in the thermal expansion coefficients of ZnO and gold [239]. The thermal expansion

coefficients for ZnO and gold are 6.5 x 10^{-6} (/°K) [52] and 14.0 x 10^{-6} (/°K) [240] respectively. Many deposition and growth techniques of ZnO are not suitable for creating epitaxial interfaces on gold as they rely on high temperature methods. There have, however, been a few reports of the epitaxial growth of ZnO on gold. One such report shows that ZnO nanopillars have been epitaxially electrodeposited on several orientations of single crystalline gold substrates [241], [242]. In addition to epitaxial interfaces between the ZnO and gold, smooth films of ZnO are desirable for many optoelectronic applications such as current spreading layers in light emitting diode devices [138]. In previous reports, smooth, continuous epitaxial films of ZnO on Au have been difficult to achieve. In this work, large single crystalline gold microplates are created using a single step thermolysis technique [243], [244] onto which thick layers of single crystalline ZnO are nucleated and grown by the low temperature aqueous growth method utilized throughout this work. Some of the advantages of this low temperature aqueous growth method on gold microplates are that the growth method doesn't require an electrical bias, which was needed for electro-deposition of ZnO [241], [242], and that large, smooth films of ZnO are created due to the coalescence of ZnO rods during the growth. In addition, the large gold microplates can be grown on any substrate as long as that substrate does not react with the growth solution and can withstand the 130°C fabrication process temperature. All of these advantages make the aqueous epitaxial growth of single crystalline ZnO on single crystalline gold an exciting and important development for the creation of novel devices and structures.

6.2 Experimental Methods

This work focuses on growing and characterizing ZnO-Au interfaces by combining the ZnO aqueous growth method used throughout this thesis with large gold microplates grown via the method detailed in [243], [244], as shown in Figure 6.1. This method involves the growth of Au microplates on silicon substrates by thermolysis of a $(AuCl_4)^-$-tetraoctylammonium bromide (TOAB) complex in air [243], [244]. In order to perform this gold microplate synthesis technique, 3.2mL of 25mM hydrogen tetrachloroaurate(III) hydrate in deionized water was mixed with 8mL of 50mM tetraoctylammonium bromide (TOAB) in toluene. The solution was continuously stirred using a magnetic stir bar and then the top part of the solution, consisting of a Au-TOAB complex in toluene, was pipetted off and placed in a separate vial. Following this, the silicon substrates were placed on a 130°C hotplate where the Au-TOAB complex in toluene was drop-cast onto the substrates. The samples were left on the hotplate for 24 to 48 hours, depending on how the gold plate formation was progressing, and then thoroughly rinsed in toluene and dried with nitrogen. Gold plates formed were either triangular or hexagonal, and the top surfaces of these microplates were found to be atomically smooth making them ideal for the growth of smooth ZnO films.

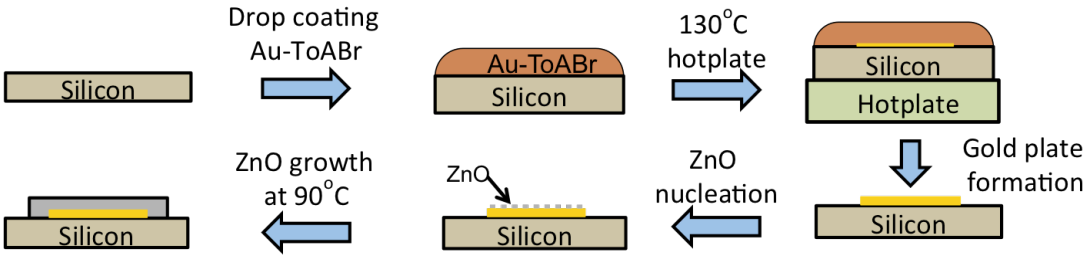

Figure 6.1: Fabrication process for epitaxial growth of single crystalline ZnO on single crystalline gold microplates. Gold microplates are formed using a single step thermolysis technique. ZnO is grown on top of the gold microplates using a low temperature aqueous growth method.

The ZnO was grown on the Au microplates using the aqueous solution based growth detailed in Chapter 2 [65], [75], [138]. This method is a two-step nucleation and growth process where ZnO is first nucleated on the substrate and then subsequently grown such that the nucleated islands of ZnO coalesce into uniform single crystalline films. All gold microplate substrates were first cleaned in an Anatech 106 oxygen plasma barrel asher for 1 minute to remove any organics on the surface. Two different ZnO nucleation methods, either microwave or oven heating, were used in this work to study the different ZnO film morphologies. The first nucleation method involved placing the sample, consisting of the silicon with gold microplates on it, upside down in a Teflon container consisting of a solution of 0.2g zinc nitrate hexahydrate, 1.25mL of 15M ammonium hydroxide, and 24mL of deionized water. The top was then tightly closed on the Teflon container and the vessel was placed in a microwave oven (GE model JES738WJ02) for 25 seconds. Microwave heating produces a rapid change in the temperature of the solution, therefore causing a supersaturation to occur. The second nucleation method involved the same growth solution and container except it was placed in a 90°C conventional oven for at least 1.5 hours. Following the nucleation in both cases, the containers were removed from either the microwave or oven and the samples were thoroughly rinsed with deionized water and dried with nitrogen. For each sample either the microwave nucleation or oven nucleation method was used.

Regardless of which nucleation method was used, the growth stage was performed by placing the nucleated sample upside down in a Teflon container consisting of 0.2g of zinc nitrate hexahydrate, 1.25mL of 15M ammonium hydroxide, 24mL of deionized water, and 0.05g of sodium citrate tribasic dehydrate. The container was tightly sealed and placed in a

90°C conventional oven for between 4 hours and 24 hours depending on the thickness of ZnO desired. Following the growth, the container was removed from the oven and the sample was carefully rinsed with deionized water and dried with nitrogen.

To investigate the ZnO at the interface with the gold microplate, a flip-press process was used to invert the ZnO-gold plate structures as shown in Figure 6.2. This flip-press process involved spin coating a silicon substrate with AZ 5214E (Clariant) photoresist at 2000rpm for 30s. The silicon with photoresist on it was then soft-baked at 100°C for 1min, which resulted in an approximately 2μm thick layer of resist. The ZnO-gold structures on the other silicon substrate were flipped upside down and pressed into the silicon substrate with photoresist on it. To ensure even pressure on the sandwiched structure a heavy block was placed on top. The sandwiched structure was then heated to 130°C, which is above the glass transition temperature of the photoresist [245], and held at that temperature for 30 minutes before being cooled to room temperature. Once the sample was completely cooled, the two pieces of silicon were separated and some of the microplate structures remained stuck in the photoresist. After the flip-press process, the gold was completely removed using a selective chemical wet etch, Au etchant Type TFA (Transene Company). The sample was left in the gold etch for between 10 minutes and 60 minutes depending on the thickness of the gold plate. Study of the now exposed ZnO allows for the detailed investigation of the ZnO material at the interface.

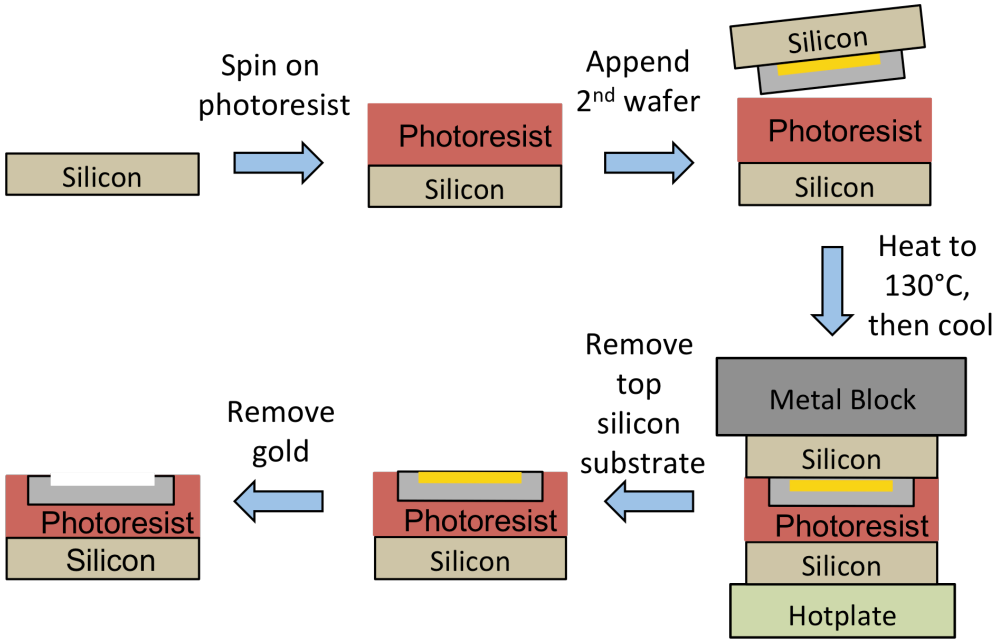

Figure 6.2: Flip-press process for investigation of ZnO material at ZnO-gold interface.

A thorough investigation of the ZnO at this interface layer was performed using several techniques. Scanning electron microscopy (SEM) was used to image the top surfaces of structures. It was done using a Supra55VP field emission SEM (Carl Zeiss AG, Germany). This SEM was also used for electron backscatter diffraction (EBSD) measurements to investigate the crystalline orientation of the ZnO and Au as well as the material quality. An Asylum MFP-3D atomic force microscope (AFM) was used to measure surface roughness of the various materials studied. Optical measurements were performed using the 325nm (HeCd) laser in the LabRAM ARAMIS photoluminescence system (HORIBA Scientific, Japan) described in Chapter 3. Transmission electron microscopy (TEM) was used to further investigate and confirm the epitaxial relationship between the ZnO and Au. A "lift-out" method performed using a Zeiss NVision 40 focused ion beam (FIB) system was employed to fabricate cross-sectional samples needed for TEM

measurements. The TEM measurements were done on a JOEL-2100 at 200kV. A Zeiss Libra 200 monochromatic, Cs-corrected transmission electron microscope at 200kV (Cs-corrected to approximately -1μm) was used to obtain the HRTEM micrograph.

6.3 Results and Discussions

The first step in the investigation of the epitaxial growth of single crystalline zinc oxide on the single crystalline microplates was to study the effects of the two different nucleation methods. As described in the previous section, both microwave and conventional oven nucleation techniques were used on different samples. Figure 6.3 shows both drawings as well as SEM images of the resulting nucleation layers using both methods. ZnO is grown using the before mentioned aqueous growth method by the slow increase in temperature resulting in the decrease in the solubility of zinc species in the solution [74], [75]. Figure 6.3(a) shows a SEM image of a gold microplate used as the substrate for ZnO nucleation and growth. The gold microplate is atomically flat with well-defined edges. The microwave nucleation technique caused a rapid temperature change of the growth solution up to approximately 95°C. This change in temperature resulted the nucleation of a dense ZnO seed layer on the gold microplates as shown in Figure 6.3(c). In addition to nucleation on the gold plates, some ZnO nucleation also occurred on the silicon wafer. The ZnO seed layer, as depicted in Figure 6.3(b) and shown in Figure 6.3(c), is made up of many hexagonal faceted pillar structures covering the gold microplate.

Oven nucleation of the ZnO is shown in Figure 6.3(d) and Figure 6.3(e). The oven nucleation increases the temperature of the solution much more slowly, over the course of 1.5 hours, than the microwave nucleation technique. In this case, randomly dispersed ZnO

crystallites were observed sparsely covering the Au microplate. While some of the ZnO crystallites were up to 1μm tall, many granular ZnO particles were seen across the surface of the gold. It has previously been shown that it is possible to grow ZnO nanowires on metal films, such as gold, without the use of a seed layer [246]. If the sample was left in the oven for a longer period of time it is believed that similar nanowire structures would have been observed. The large variation in the height of the ZnO nucleated on the gold microplates using the conventional oven technique is attributed to some of the ZnO islands starting to grow at an earlier time than others. Therefore, the two different nucleation techniques, while both resulting in ZnO nucleation on the Au microplates, produced very different seed layers.

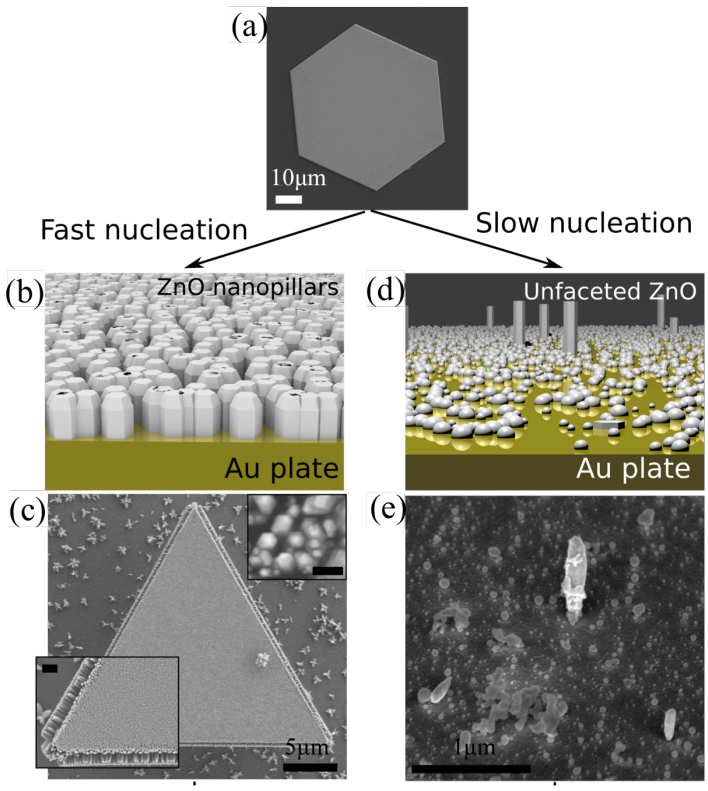

Figure 6.3: ZnO aqueous nucleation on single crystalline gold microplates using two different speed nucleation techniques, which controlled the growth kinetics. (a) SEM image of the single crystalline microplate. (b) Schematic of ZnO nucleated on the gold microplate using the microwave nucleation technique showing the densely packed, hexagonally faceted pillar structures. (c) SEM image of ZnO seed layer on Au microplate formed using microwave nucleation. The bottom left and top right inserts show high magnification images of the ZnO seed layer at the corner of the microplate and middle of the microplate respectively. The scale bar for the bottom left insert is 1μm and the scale bar for the top right insert is 200nm. (d) Schematic of ZnO nucleated on the gold microplate using oven nucleation technique showing the sparse ZnO seed layer of varying height. (e) SEM image taken at a 45° angle of the ZnO seed layer on the Au microplate formed using oven nucleation. [129]

Following nucleation, a growth step was done in a 90°C conventional oven to create ZnO films on top of the gold microplates. Figure 6.4(a) and Figure 6.4(c) show schematic drawings of the ZnO layer grown after microwave nucleation and oven nucleation, respectively. Figure 6.4(b) and Figure 6.4(d) show the corresponding SEM images taken of top surface of the ZnO film on the Au microplates. For the case where microwave nucleation was used to create the seed layer followed by aqueous growth in a conventional oven, a smooth, flat ZnO film is observed on top of the Au. The individual ZnO structures formed during the nucleation coalesced during the growth stage. The root mean square roughness of the ZnO film was measured used AFM and found to be 7nm.

When oven nucleation was performed before the growth step, the ZnO film was found to be rough and faceted as shown in Figure 6.4(d). In this case, each of the nucleated islands, which were all different heights, grew together forming a film of ZnO with very distinctive hexagonal grains. In addition, these large, hexagonal grains were also at various heights causing the overall film to be rough. Interestingly, the epitaxial relationship between the ZnO and the gold is, however, observed in these films, as each of the hexagonal grains is oriented in the same direction. The ZnO that grew on the silicon substrate didn't show this alignment of the grains.

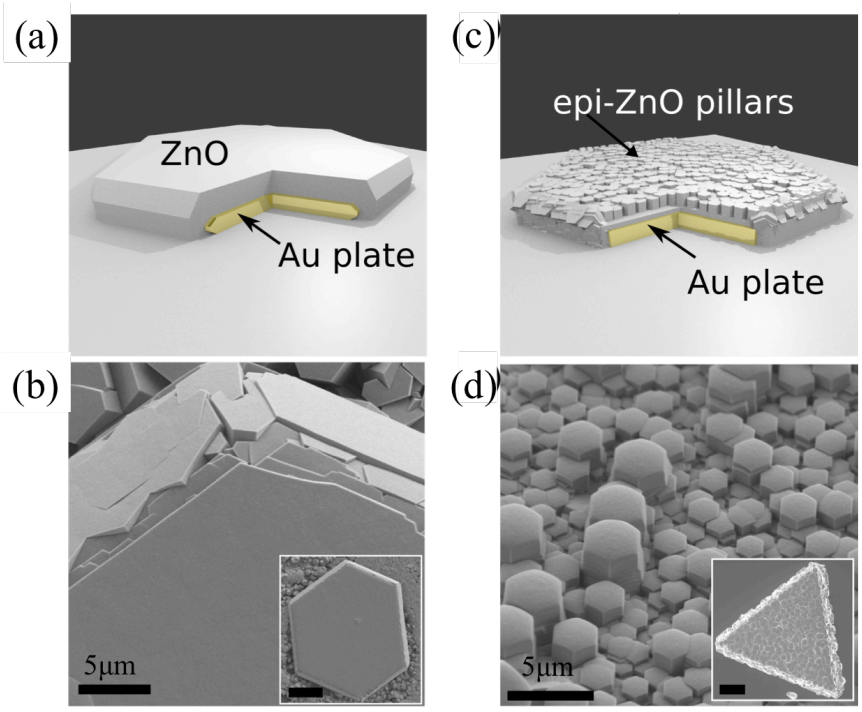

Figure 6.4: Film morphology of the ZnO layer grown on gold after microwave nucleation (left column) and after oven nucleation (right column). (a) Schematic of the smooth, flat ZnO grown on the Au microplate after microwave nucleation and then growth. (b) SEM image of the smooth, flat ZnO grown on the gold microplate after the microwave nucleation step. The insert shows the entire microplate with ZnO grown on it. The scale bar is equal to 40μm. (c) Schematic of the rough, faceted ZnO grown on the Au microplate after oven nucleation and then growth. (d) SEM image taken at a 45° angle of the rough, faceted ZnO grown on the gold microplate after the oven nucleation step. The insert shows the entire microplate with ZnO grown on it. The scale bar is equal to 20μm. [129]

As the ZnO growth on the gold microplates covered all sides of the microplates, focused ion beam milling was used to accurately measure the thickness of the ZnO films. ZnO films grown on gold microplates, which were nucleated using the fast microwave technique, were measured to be approximately 3μm as shown in Figure 6.5(a). Films grown after the oven nucleation step were found to be approximately 10μm as shown in Figure 6.5(b). Identical growth solutions were used in both cases and therefore the total volume of ZnO grown should be equivalent. The difference in the thickness of the ZnO grown on the gold microplates is due to the substantial nucleation and growth of ZnO on the silicon substrate for the microwave nucleated sample. The sample nucleated in the oven and then grown had very minimal growth on the silicon substrate. Nucleation of ZnO only on the metal has been previously observed in the literature [246]. Therefore, it makes sense that when the ZnO only grows on the Au microplate the film thickness will be larger.

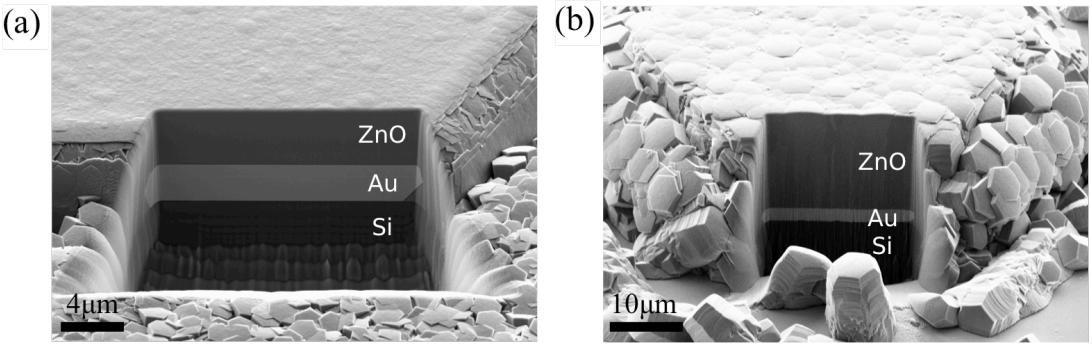

Figure 6.5: Focused ion beam cross-section images of ZnO grown on gold microplates. (a) ZnO grown on gold using fast, microwave nucleation method. ZnO film thickness is approximately 3μm. (b) ZnO grown on gold using slow, oven nucleation method. ZnO film thickness is approximately 10μm. [129]

To investigate the ZnO material directly on top of the gold plate, the flip press process shown in Figure 6.2 was used. Figure 6.6(a) shows an SEM image of one of the flipped plates after the gold plate has been etched away. The specific sample shown in

Figure 6.6(a) was nucleated using the fast nucleation technique and then subsequently grown however, films fabricated using the slow nucleation method were also flipped and investigated. More detailed SEM images of the ZnO at the ZnO/Au interface are shown in Figure 6.6(b) and Figure 6.6(d) for the fast and slow nucleation respectively. In addition, atomic force microscopy, shown in Figure 6.6(c) and Figure 6.6(e), was used to measure the roughness of the ZnO film at the interface. The ZnO material at the ZnO-Au interface when nucleated quickly had a root-mean-squared (RMS) roughness of approximately 50nm while the RMS roughness of the material nucleated slowly was approximately 4nm.

The ZnO film produced using the fast nucleation technique and growth is more porous than the film nucleated slowly. During the fast nucleation, many hexagonal ZnO nanopillars with about the same height are formed on the gold plate. When ZnO growth occurs, it may be difficult for the Zn species to diffuse to the bottom of the nucleated pillars due to the high density of the pillars on the gold plate. As a consequence during the ZnO growth, the ZnO is not able to coalesce near the bottom of the nucleated layer leading to the porous material. In the case of the slowly nucleated film, the ZnO material is able to fully coalesce at the ZnO/Au interface because the nucleation layer is much less dense. The growth solution is able to diffuse to the ZnO/Au interface and the nucleated ZnO coalesces into a smooth film. It can be seen in Figure 6.6(d) that there appear to be several large grains in the ZnO film. These grains are not found to correspond to any specific crystalline direction and are believed to be a result of disturbances in the growth solution during the long nucleation time. For example, it is possible that precipitates settled onto the surface of the gold plate during the nucleation or that the gold plate undergoes some deformation, which

causes the grains to appear. The exact cause of the grains at the ZnO/Au surface for the slowly nucleated film is still being investigated.

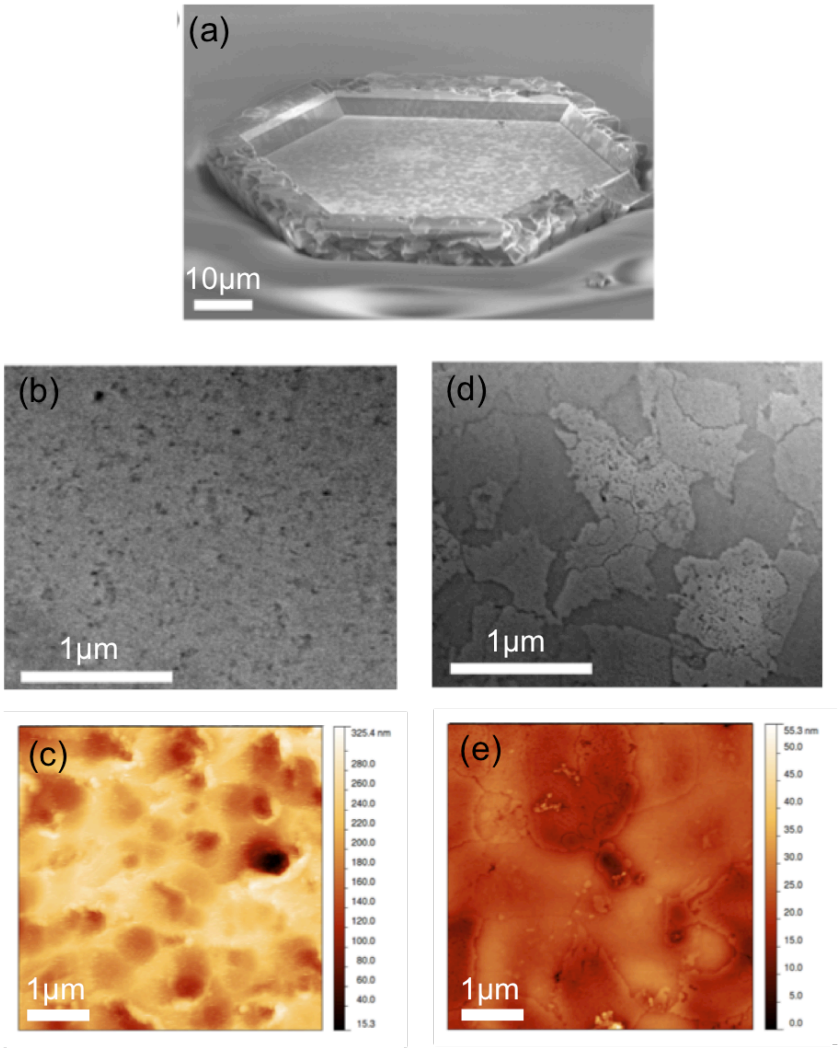

Figure 6.6: SEM and AFM images of the ZnO on gold microplates after the removal of the gold plate. (a) SEM image of the entire flipped structure showing the ZnO material that was at the interface with the gold. (b) Detailed SEM image of the ZnO material at the interface formed using the fast nucleation technique. (c) AFM image of the ZnO at the interface formed using the fast nucleation technique. The rms roughness is 50nm. (d) Detailed SEM image of the ZnO material at the interface formed using the slow nucleation technique. (c) AFM image of the ZnO at the interface formed using the slow nucleation technique. The rms roughness is 4nm. [129]

Electron backscatter diffraction was used to study the crystal orientations of the ZnO film and gold plate and infer an epitaxial relationship between the two materials. The sample shown in Figure 6.7 was nucleated using the fast nucleation technique and then subsequently grown however, EBSD measurements, not shown here, were also performed on samples fabricated using the slow nucleation technique and gave similar results. Figure 6.7(a) shows the inverse pole figure map for the gold microplate. It is clear from this map that the gold microplate is single crystalline with no evidence of grain boundaries. In addition, the top surface of the gold plate is oriented in the (111) direction. Figure 6.7(b) shows the inverse pole figure map for the gold plate after the nucleation and growth of ZnO. Again the material is found to be single crystalline and the top surface of the ZnO is oriented in the (0001) direction.

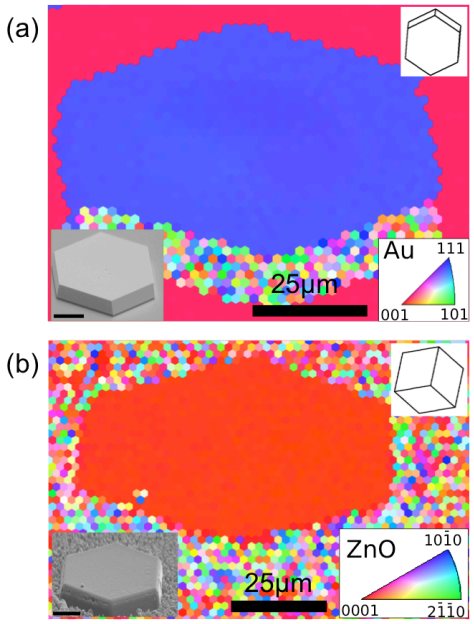

Figure 6.7: EBSD measurements performed on a gold microplate before and after ZnO growth. (a) EBSD IPF map of a single crystal gold microplate. (b) EBSD IPF map of ZnO grown on the same gold microplate. The upper right inset for both (a) and (b) show the unit cell of the gold microplate. The lower left insert shows the SEM image of the structure EBSD was performed on in both cases. [129]

Angular characterization was performed using electron backscatter diffraction for numerous points across the plate as shown in Figure 6.8. The tight distributions in the pole figures for both the gold plate and the ZnO film confirm that the materials are single crystalline. In addition, the relative misorientation in the ZnO and gold is found to be negligible and no large angle grain boundaries are observed. As can be seen in the histogram of angular point-to-point misorientation in Figure 6.8, the distribution of the crystallographic directions observed for the gold plate appears to be smaller than that for the ZnO film. Only about 3% of the points measured on the ZnO film had a missorientaion larger than the ~2° resolution of the EBSD measurement. Therefore, small angle grain boundaries are found in the ZnO material.

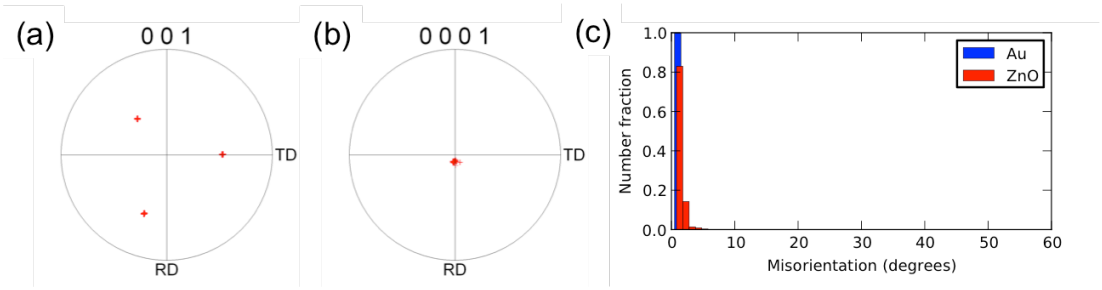

Figure 6.8: Electron backscatter diffraction angular characterization of a gold microplate and the ZnO film. (a) Pole figure of a gold microplate. (b) Pole figure of the ZnO film. (c) Distribution of point-to-point angular misorientation of ZnO and gold. [129]

The two EBSD measurements shown in Figure 6.7 were slightly rotated with respect to each other. After the rotation was accounted for, a comparison of the unit cells for the gold microplate and ZnO film, shown as insets in Figure 6.7(a) and Figure 6.7(b) respectively, revealed an epitaxial relationship across a large area. From the EBSD data the epitaxial relationship ZnO $[1\bar{1}00](0002) \parallel$ Au $[2\bar{1}\bar{1}](111)$ is inferred. Due to the low

angular resolution of the EBSD measurement, transmission electron microscopy was used to confirm the epitaxial relationship between the two materials.

Mor Baram, a now former postdoc in Professor David Clarke's laboratory, performed the TEM measurements presented here to further investigate the epitaxial relationship between the ZnO and gold. These measurements are detailed in [129] and show conclusively that two epitaxial relationships are observed between ZnO and gold. A sample for the TEM measurements, shown in Figure 6.9, was made using focused ion beam milling. A columnar microstructure is observed in the bright field TEM image of the ZnO on gold sample indicating that the material originally grew from small islands of material before coalescing into a film. The roughness observed on the top surface of the ZnO material in Figure 6.9 is due to the material thinning necessary for TEM sample preparation.

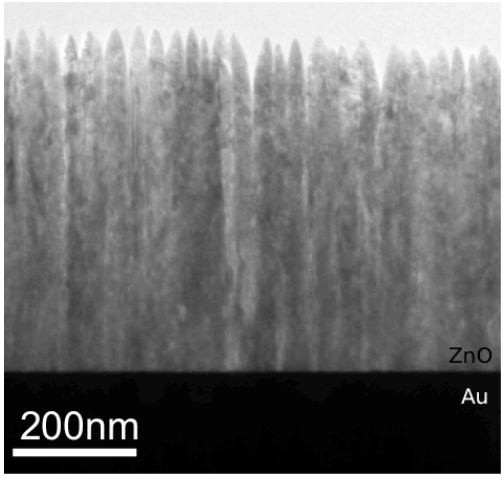

Figure 6.9: Bright field TEM image of a cross-section of the ZnO on gold structure showing the interface between the two materials. The appearance of column structures indicates that the ZnO originally grew from islands of material. The top surface roughness of the ZnO is due to the thinning of the material during sample preparation. [129]

Selected area electron diffraction (SAED) was used to index the planes present in the cross-sectional TEM image at the interface as shown in Figure 6.10(a). The lines in the

SAED images are due to camera artifacts and can be ignored. The left most image is the SAED for ZnO near the ZnO/Au interface, the middle image is the SAED for the ZnO/Au interface, and the right most image is the SAED for Au near the interface.

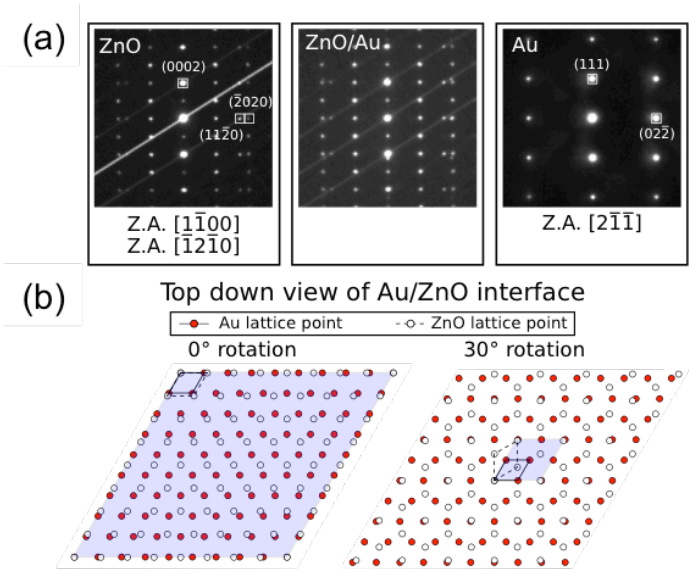

Figure 6.10: Selected area electron diffraction (SAED) and cross-sectional TEM confirmation of the epitaxial relationship between ZnO and gold. (a) SAED of (left) ZnO, (middle) ZnO and gold, and (right) gold near the interface. (b) Drawing of the 2D projection of the close-packed planes of Au (111) and ZnO (0001) at the interface. The solid line is the unit cell for gold and the dashed line is the unit cell for ZnO. Two epitaxial relationships are observed which correspond to (left) no lattice rotation and (right) a 30° lattice rotation about the [0001] axis with respect to the (111)[111] gold lattice. [129]

Two zone axes are observed in the SAED images shown in Figure 6.10(a) indicating that two orientations of ZnO are epitaxial with the Au microplate at the interface measured. The first epitaxial relationship measured is ZnO $[1\bar{1}00](0002) \parallel$ Au $[2\bar{1}\bar{1}](111)$, which corresponds to no rotation between the two close packed lattices as shown in the left part of Figure 6.10(b). The other epitaxial relationship found is ZnO $[\bar{1}2\bar{1}0](0002) \parallel$ Au $[2\bar{1}\bar{1}](111)$, which corresponds to a 30° lattice rotation about the [0001] axis with respect to the (111)[111] gold lattice as shown in the right part of Figure

6.10(b). It was determined using the strength of the SAED signal reflections from $[1\bar{1}00]$ and $[\bar{1}2\bar{1}0]$ ZnO that the preferred and dominant epitaxial crystal orientation is ZnO $[1\bar{1}00](0002) \parallel$ Au $[2\bar{1}\bar{1}](111)$ as the $[1\bar{1}00]$ reflections of ZnO were much stronger.

Lastly, photoluminescence spectroscopy, shown in Figure 6.11, was done to further investigate the quality of ZnO epitaxially grown on the gold microplates. The data shown in Figure 6.11 is from a ZnO film for which a fast nucleation step was used followed by ZnO growth. Similar to results shown in Chapter 3, the initially grown ZnO shows photoluminescence at higher energies (lower wavelengths) than would be expected. Two peaks can be resolved in the band edge peak of the spectra at 3.5eV and 3.28eV. The sample was then annealed on a hotplate at 250°C for 30 minutes followed by at 300°C for 30 minutes. The photoluminescence spectrum after being annealed was shifted to lower energies (~3.26eV) and appears more asymmetric. In addition, the intensity of the band edge peak increases after being annealed. The change in the photoluminescence spectrum with heating of the ZnO is attributed to the release of water from the material. Since an aqueous growth is used, it is likely that some residual water remains in the film after growth. Once the defects are removed from the ZnO by heating, a large UV band edge peak is observed, which is characteristic of high quality ZnO. The small defect band centered around 2.06eV or 600nm remains unchanged after the annealing of the ZnO films and the wavy pattern in the defect band of the photoluminescence spectra is due to thin film interference.

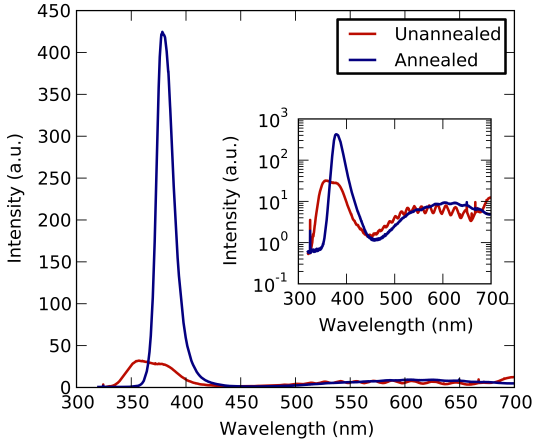

Figure 6.11: Photoluminescence spectroscopy of ZnO film grown on gold microplate before and after being annealed. A step anneal on a hotplate of 30 minutes at 250°C followed by 30 minutes at 300°C was used. The insert is a log-linear plot of the two spectra where thin film interference is observed in the defect bands. [129]

6.4 Conclusions

The ability to integrate metals and semiconductors is essential for the creation and performance of many high quality devices. In this chapter single crystalline ZnO is epitaxially grown on Au microplates and the quality of the interface and the materials are studied. Altering the speed of nucleation can control the morphology of both the top surface of the ZnO as well as the ZnO at the ZnO/Au interface. The epitaxial relationship between the ZnO and Au was first studied using EBSD, which confirmed that both materials were single crystalline. In addition, small angle grain boundaries were measured in the ZnO film. As the EBSD measurement had low resolution, the epitaxial relationship of the materials was further studied using TEM. TEM revealed that there are two epitaxial relationships between ZnO and Au however, the most prominent relationship is ZnO $[1\bar{1}00](0002) \parallel$ Au $[2\bar{1}\bar{1}](111)$. This is the first reported low temperature, aqueous,

epitaxial growth of ZnO on gold [129]. The ability to epitaxially grow a semiconductor on a metal opens the door for many new and improved electrical, optical, and plasmonic devices. For example, a high quality metal-semiconductor interface promises more reliable, better-controlled electrical transmission across that interface, as well as a better-controlled reflectivity at the metal-semiconductor interface. In addition, being able to create an epitaxial interface between ZnO and Au is advantageous as one looks ahead at possibly electrically injecting many of the ZnO optical structures shown throughout this thesis. Overall, the epitaxial growth of ZnO on gold is important for both the continued investigations of the ZnO material as well as for the fabrication of novel ZnO devices.

Chapter 7

Conclusion

This thesis has demonstrated the ability to grow high quality single crystalline ZnO using a bottom-up aqueous growth method. The quality of the material was investigated, and the potential to create intricate three-dimensional structures was explored. By growing ZnO through molds of various sizes and shapes, an understanding of how the material grows and the types of structures possible has been determined. Several different devices have been fabricated, demonstrating promising steps towards the realization of high quality single crystalline ZnO optoelectronic devices. In addition, the first demonstration of the low temperature, aqueous, epitaxial growth of ZnO on single crystalline gold plates is presented. This opens the door to many new and improved wide bandgap optoelectronic devices.

7.1 Experimental Results Summary

The experimental results begin in Chapter 3 with a detailed investigation into the quality of aqueously grown single crystalline ZnO. Photoluminescence of the as-grown ZnO shows the presence of additional energy levels in the material that are most likely caused by

the aqueous growth method used. While the exact cause of the additional energy levels is still under investigation, it is believed that strain due to the lattice mismatch with the substrate is a contributing factor. To explore this further, the effects of annealing aqueously grown ZnO films are investigated. Upon heating, cracking of the grown layer is observed, resulting in a reduction in the magnitude of the strain throughout the ZnO material. Comparison of optical measurements before and after annealing show that after the growth-induced strain is relieved the aqueously grown ZnO emits photoluminescence that closely resembles that of commercially purchased ZnO samples. This confirms the high quality of the aqueously grown material. Interestingly, it was also found that annealing the sample affected the photoconductivity of the aqueously grown material. Before heating, the as-grown ZnO had a large persistent photoconductivity that was not observed after the thermally induced cracking of the aqueously grown ZnO or in the commercially purchased ZnO. It is therefore believed that thermal treatment of aqueously grown ZnO produces high quality single crystalline material. This is a promising result as it allows for easy, low temperature growth of high quality wide bandgap material that can be used to fabricate a variety of optoelectronic devices.

In Chapter 4, experiments creating intricate three-dimensional structures using selective aqueous growth through pre-patterned molds are presented. Photolithography and electron beam lithography are used to fabricate molds in a layer of PMMA resist, through which ZnO is grown. Significantly, it is observed that the ZnO conforms exactly to the molded region however, once the material reaches the top of the mold, the ZnO grows unconstrained and typically forms hexagonal structures. Furthermore, control of the size and shape of the ZnO structures produced with this method has been achieved via variation of the

mold size and shape, concentration of the growth solution, and growth time. The potential for this method to produce high quality photonic devices is evidenced by the advantageous crystalline properties of the resulting structures. The bottom-up fabrication technique presented in this work has been shown to produce structures with vertical sidewalls, crystallographic facets, and well-defined undercuts, all of which are difficult to achieve using most other fabrication methods. Electron backscatter diffraction allowed for the detailed investigation into the orientation of the crystalline planes of ZnO with respect to the base layer and the orientation of the mold. As expected, the orientation of the mold patterns relative to the crystalline planes of the ZnO strongly influence the resulting structures, with the highest quality structures resulting from cases where there was alignment. The ability to fabricate complex three-dimensional structures in a controllable way is an import step towards bottom-up device fabrication in ZnO.

With a detailed understanding of how the ZnO grows and what structures are possible, three different types of devices are fabricated and simulated in Chapter 5. These devices include microdisk resonators, ring structures, and pillar photonic crystals. The fast growth rate of the vertical c-plane of ZnO was a challenge in fabricating both the microdisk resonators and ring structures, as the thickness of these devices typically needs to be on the order of the wavelength of light. This work has made some progress towards the mitigation of this problem via manipulation of the growth aspect ratios by including sodium citrate. This is a promising avenue for future work into using the bottom-up aqueous method for creating photonic devices. The ring structures fabricated show a 30° rotation between the inside and outside facets of the structures. This has been seen previously in GaN however; this is the first experimental observation in ZnO.

The last devices fabricated and simulated in Chapter 5 were pillar photonic crystal structures. These devices are promising not only for use as cavities but also for use as waveguides and filters. Unlike for the case of resonators discussed above, it is often desirable to create pillars with very high aspect ratios. This makes the aqueous growth method used in this work ideal for creating pillar structures. Photonic crystals with aspect ratios as high as 20:1 and various r/a values were fabricated. Even though the ZnO pillars are grown on a base layer of ZnO, the post region, determined by the mold grown through, creates a region with a different effective refractive index and allows for optical isolation of light in the ZnO pillars. Simulations of the quality factors of band edge modes in such ZnO pillar photonic crystals on posts were found to be similar to those for identical pillar photonic crystals with no posts or substrate. This is an exciting and promising discovery and opens the door for the creation of single crystalline ZnO filters, waveguides, and photonic crystal cavities.

Lastly, Chapter 6 details the fabrication and investigation of the low temperature epitaxial growth of ZnO on single crystalline gold microplates. To date, ZnO has been grown epitaxially on several materials including $MgAl_2O_4$ and GaN, amongst others, but the epitaxial growth of smooth continuous films on metals has not been reported. Two different nucleation methods were used to alter the growth kinetics of the ZnO. The fast nucleation and then growth produced smooth top surfaces of the ZnO while the slow nucleation and then growth produced a more rough material due to the larger variation in the height of the nucleated ZnO pillars. A flip process was used to remove the ZnO-Au structures from the substrate so that the gold could be removed and the ZnO at the interface could be studied. The fast nucleation resulted in a material with a greater roughness than the slow nucleation

did. It was determined using electron backscatter diffraction and transmission electron microscopy that an epitaxial relationship between ZnO and Au exists. TEM measurements revealed that there are actually two epitaxial relationships however, the relationship with no rotation between the close packed planes of ZnO and Au was found to be the most prominent. The low temperature, epitaxial growth of single crystalline ZnO on Au is important for many device applications.

Overall, the work presented in this thesis demonstrates the potential for using aqueous growth techniques for the bottom-up fabrication of ZnO devices. A detailed study of the quality of the ZnO grown by this method, as well as the types of structures and devices that are possible, are presented. In addition to creating high quality three-dimensional ZnO structures, epitaxial interfaces between ZnO and single crystalline gold are also realized using the same aqueous growth approach. Such interfaces are a promising avenue for future study as they have the potential to increase the efficiency of electrical injection and light out-coupling in optoelectronic devices. With the increasing interest in using wide bandgap semiconductors for a range of optoelectronic applications, much attention has been focused on developing a way of integrating such materials into semiconductor technology. This work represents a major step towards the development of ZnO devices, and the bottom-up aqueous growth method used throughout this thesis shows significant promise for integrating these structures with existing materials systems. Promising avenues for extending this work include the development of optically active photonic crystals and the exploration of electrical injection and plasmonic effects in devices epitaxially grown on gold.

References

[1] G. E. Moore, "Cramming more components onto integrated circuits," *Electronics*, vol. 38, no. 8, 1965.

[2] S. C. Lin and K. Banerjee, "Cool chips: Opportunities and implications for power and thermal management," *IEEE Trans. Electron Devices*, vol. 55, no. 1, pp. 245–255, 2008.

[3] S. Assefa, S. Shank, W. Green, M. Khater, E. Kiewra, C. Reinholm, S. Kamlapurkar, C. Schow, F. Horst, H. Pan, T. Topuria, P. Rice, D. M. Gill, J. Rosenberg, and T. Barwicz, "A 90nm CMOS Integrated Nano-Photonics Technology for 25Gbs WDM Optical Communications Applications," in *IEEE International Electron Devices Meeting*, 2012.

[4] G. J. Sullivan, M. Y. Chen, J. A. Higgins, J. W. Yang, Q. Chen, R. L. Pierson, and B. T. McDermott, "High-power 10-GHz operation of AlGaN HFET's on insulating SiC," *IEEE Electron Device Lett.*, vol. 19, no. 6, pp. 198–200, 1998.

[5] R. Triboulet, V. Munoz-Sanjose, R. Tena-Zaera, M. Martinez-Tomas, and S. Hassani, "Zinc Oxide - A Material for Micro and Optoelectronic Applications," in *Zinc Oxide - A Material for Micro and Optoelectronic Applications*, N. Nickel and E. Terukov, Eds. Dordrecht, The Netherlands: Springer, 2005, pp. 3–14.

[6] R. J. Collins and D. A. Kleinman, "Infrared reflectivity of zinc oxide," *J. Phys. Chem. Solids*, vol. 11, no. 3–4, pp. 190–194, 1959.

[7] R. R. Reeber, "Lattice parameters of ZnO from 4.2° to 296°K," *J. Appl. Phys.*, vol. 41, no. 13, pp. 5063–5066, 1970.

[8] R. B. Heller, J. McGannon, and A. H. Weber, "Precision determination of the lattice constants of zinc oxide," *J. Appl. Phys.*, vol. 21, no. 12, pp. 1283–1284, 1950.

[9] Y. S. Park and J. R. Schneider, "Index of refraction of ZnO," *J. Appl. Phys.*, vol. 39, no. 7, pp. 3049–3052, 1968.

[10] J. Bao, M. A. Zimmler, F. Capasso, X. Wang, and Z. F. Ren, "Broadband ZnO single-nanowire light-emitting diode," *Nano Lett.*, vol. 6, no. 8, pp. 1719–1722, 2006.

[11] G. T. Du, W. F. Liu, J. M. Bian, L. Z. Hu, H. W. Liang, X. S. Wang, A. M. Liu, and T. P. Yang, "Room temperature defect related electroluminescence from ZnO homojunctions grown by ultrasonic spray pyrolysis," *Appl. Phys. Lett.*, vol. 89, no. 5, pp. 50–53, 2006.

[12] S. Masuda, K. Kitamura, Y. Okumura, S. Miyatake, H. Tabata, and T. Kawai, "Transparent thin film transistors using ZnO as an active channel layer and their electrical properties," *J. Appl. Phys.*, vol. 93, no. 3, pp. 1624–1630, 2003.

[13] R. L. Huffman, "ZnO-channel thin-film transistors: Channel mobility," *J. Appl. Phys.*, vol. 95, no. 10, pp. 5813–5819, 2004.

[14] U. Özgür, Y. I. Alivov, C. Liu, A. Teke, M. A. Reshchikov, S. Doğan, V. Avrutin, S.-J. Cho, and H. Morkoç, "A comprehensive review of ZnO materials and devices," *J. Appl. Phys.*, vol. 98, no. 4, p. 041301, 2005.

[15] A. Janotti and C. G. Van de Walle, "Fundamentals of zinc oxide as a semiconductor," *Reports Prog. Phys.*, vol. 72, no. 12, p. 126501, Dec. 2009.

[16] E. Ohshima, H. Ogino, I. Niikura, K. Maeda, M. Sato, M. Ito, and T. Fukuda, "Growth of the 2-in-size bulk ZnO single crystals by the hydrothermal method," *J. Cryst. Growth*, vol. 260, pp. 166–170, 2004.

[17] X. J. Ning, F. R. Chien, P. Pirouz, J. W. Yang, and M. A. Khan, "Growth defects in GaN films on sapphire: The probable origin of threading dislocations," *J. Mater. Res.*, vol. 11, no. 03, pp. 580–592, 1996.

[18] C. Bundesmann, R. Schmidt-Grund, and M. Schubert, "Optical Properties of ZnO and Related Compounds," in *Transparent Conductive Zinc Oxide: Basics and Applications in Thin Film Solar Cells*, K. Ellmer, A. Klein, and B. Rech, Eds. Berlin, Germany: Springer, 2008, pp. 79–124.

[19] A. Teke, Ü. Özgür, S. Doğan, X. Gu, H. Morkoç, B. Nemeth, J. Nause, and H. Everitt, "Excitonic fine structure and recombination dynamics in single-crystalline ZnO," *Phys. Rev. B*, vol. 70, no. 19, p. 195207, Nov. 2004.

[20] C. H. Park, S. B. Zhang, and S.-H. Wei, "Origin of p-type doping difficulty in ZnO: The impurity perspective," *Phys. Rev. B*, vol. 66, no. 7, pp. 1–3, 2002.

[21] T. M. Barnes, K. Olson, and C. A. Wolden, "On the formation and stability of p-type conductivity in nitrogen-doped zinc oxide," *Appl. Phys. Lett.*, vol. 86, no. 11, pp. 1–3, 2005.

[22] T. Minami, H. Nanto, and S. Takata, " Highly Conductive and Transparent Aluminum Doped Zinc Oxide Thin Films Prepared by RF Magnetron Sputtering ," *Jpn. J. Appl. Phys.*, vol. 23, no. Part 2, No. 1, pp. L280–L282, 1984.

[23] S. Major, A. Banerjee, and K. L. Chopra, "Highly transparent and conducting indium-doped zinc oxide films by spray pyrolysis," *Thin Solid Films*, vol. 108, no. 3, pp. 333–340, 1983.

[24] L. Schmidt-Mende and J. L. Macmanus-Driscoll, “ZnO - nanostructures, defects, and devices,” *Mater. Today*, vol. 10, no. 5, pp. 40–48, 2007.

[25] Z. L. Wang, “Zinc oxide nanostructures: growth, properties and applications,” *J. Phys. Condens. Matter*, vol. 16, no. 25, pp. R829–R858, Jun. 2004.

[26] X. Wu, A. Yamilov, X. Liu, S. Li, V. P. Dravid, R. P. H. Chang, and H. Cao, “Ultraviolet photonic crystal laser,” *Appl. Phys. Lett.*, vol. 85, no. 17, pp. 3657–3659, 2004.

[27] S. W. Pang, “Effects of ion species and adsorbed gas on dry etching induced damage in GaAs,” *J. Vac. Sci. Technol. B Microelectron. Nanom. Struct.*, vol. 3, no. 1, pp. 398–401, 1985.

[28] J.-M. Lee, K.-M. Chang, S.-W. Kim, C. Huh, I.-H. Lee, and S.-J. Park, “Dry etch damage in n-type GaN and its recovery by treatment with an N2 plasma,” *J. Appl. Phys.*, vol. 87, no. 11, pp. 7667–7670, 2000.

[29] C. Kittel, *Introduction to Solid State Physics*. Wiley, 2004.

[30] J. R. Hook and H. E. Hall, *Solid State Physics*, 2nd ed. Wiley, 1995.

[31] C.-T. S. C.-T. Sah, R. N. Noyce, and W. Shockley, “Carrier Generation and Recombination in P-N Junctions and P-N Junction Characteristics,” *Proc. IRE*, vol. 45, no. 9, 1957.

[32] F. S. Ujager, S. M. H. Zaidi, and U. Younis, “A review of semiconductor lasers for optical communications,” *High-Capacity Opt. Networks Enabling Technol. (HONET), 2010*, pp. 107–111, 2010.

[33] R. J. Xie and N. Hirosaki, “Silicon-based oxynitride and nitride phosphors for white LEDs-A review,” *Sci. Technol. Adv. Mater.*, vol. 8, no. 7–8, pp. 588–600, 2007.

[34] D. A. B. Miller, “Optical interconnects to silicon CMOS,” *Device Res. Conf. Conf. Dig. (Cat. No.01TH8561)*, vol. 6, no. 6, pp. 1312–1317, 2001.

[35] J. D. Joannopoulos, S. G. Johnson, J. N. Winn, and R. D. Meade, *Photonic Crystals Molding the Flow of Light*, 2nd ed. Princeton University Press, 2008.

[36] I. Moerman, P. P. Van Daele, and P. M. Demeester, “A review on fabrication technologies for the monolithic integration of tapers with III-V semiconductor devices,” *IEEE J. Sel. Top. Quantum Electron.*, vol. 3, no. 6, pp. 1308–1320, 1997.

[37] D. Delbeke, R. Bockstaele, P. Bienstman, R. Baets, and H. Benisty, “High-Efficiency Semiconductor Resonant-Cavity Light-Emitting Diodes : A Review,” *IEEE J. Sel. Top. Quantum Electron.*, vol. 8, no. 2, pp. 189–206, 2002.

[38] K. D. Choquette, K. L. Lear, R. P. Schneider, K. M. Geib, J. J. Figiel, and R. Hull, "Fabrication and performance of selectively oxidized vertical-cavity lasers," *IEEE Photonics Technol. Lett.*, vol. 7, no. 11, pp. 1237–1239, 1995.

[39] I. Aharonovich, A. Woolf, K. J. Russell, T. Zhu, N. Niu, M. J. Kappers, R. a. Oliver, and E. L. Hu, "Low threshold, room-temperature microdisk lasers in the blue spectral range," *Appl. Phys. Lett.*, vol. 103, 2013.

[40] O. Painter, "Two-Dimensional Photonic Band-Gap Defect Mode Laser," *Science (80-.).*, vol. 284, pp. 1819–1821, 1999.

[41] K. Hennessy, A. Badolato, M. Winger, D. Gerace, M. Atature, S. Gulde, S. Falt, E. L. Hu, and A. Imamoglu, "Quantum nature of a strongly-coupled single quantum dot-cavity system," *Nature*, vol. 445, pp. 896–899, 2007.

[42] E. C. Nelson, N. L. Dias, K. P. Bassett, S. N. Dunham, V. Verma, M. Miyake, P. Wiltzius, J. A. Rogers, J. J. Coleman, X. Li, and P. V Braun, "Epitaxial growth of three-dimensionally architectured optoelectronic devices.," *Nat. Mater.*, vol. 10, no. 9, pp. 676–81, Sep. 2011.

[43] A. C. Scofield, S. H. Kim, J. N. Shapiro, A. Lin, B. Liang, A. Scherer, and D. L. Huffaker, "Bottom-up photonic crystal lasers," *Nano Lett.*, vol. 11, pp. 5387–5390, 2011.

[44] I. Aharonovich, J. C. Lee, A. P. Magyar, D. O. Bracher, and E. L. Hu, "Bottom-up engineering of diamond micro- and nano-structures," *Laser Photon. Rev.*, vol. 5, pp. L61–L65, Jul. 2013.

[45] D. J. Gargas, M. C. Moore, A. Ni, S.-W. Chang, Z. Zhang, S.-L. Chuang, and P. Yang, "Whispering gallery mode lasing from zinc oxide hexagonal nanodisks.," *ACS Nano*, vol. 4, no. 6, pp. 3270–3276, Jun. 2010.

[46] G. Zhang, K. Tateno, H. Gotoh, and H. Nakano, "Parallel-aligned GaAs nanowires with 110 orientation laterally grown on [311]B substrates via the gold-catalyzed vapor-liquid-solid mode.," *Nanotechnology*, vol. 21, no. 9, p. 095607, 2010.

[47] M. H. Huang, S. Mao, H. Feick, H. Yan, Y. Wu, H. Kind, E. Weber, R. Russo, and P. Yang, "Room-temperature ultraviolet nanowire nanolasers.," *Science*, vol. 292, no. 5523, pp. 1897–1899, 2001.

[48] S. Murad, M. Rahman, N. Johnson, S. Thoms, S. P. Beaumont, and C. D. W. Wilkinson, "Dry etching damage in III–V semiconductors," *J. Vac. Sci. Technol. B Microelectron. Nanom. Struct.*, vol. 14, no. 6, p. 3658, Nov. 1996.

[49] J. S. Park, H. J. Park, Y. B. Hahn, G.-C. Yi, and A. Yoshikawa, "Dry etching of ZnO films and plasma-induced damage to optical properties," *J. Vac. Sci. Technol. B Microelectron. Nanom. Struct.*, vol. 21, no. 2, pp. 800–803, 2003.

[50] E. D. Haberer, R. Sharma, C. Meier, A. R. Stonas, S. Nakamura, S. P. DenBaars, and E. L. Hu, "Free-standing, optically pumped, GaN/InGaN microdisk lasers fabricated by photoelectrochemical etching," *Appl. Phys. Lett.*, vol. 85, no. 22, pp. 5179–5181, 2004.

[51] J. C. Lee, A. P. Magyar, D. O. Bracher, I. Aharonovich, and E. L. Hu, "Fabrication of thin diamond membranes for photonic applications," *Diam. Relat. Mater.*, vol. 33, pp. 45–48, Mar. 2013.

[52] R. D. Vispute, V. Talyansky, S. Choopun, R. P. Sharma, T. Venkatesan, M. He, X. Tang, J. B. Halpern, M. G. Spencer, Y. X. Li, L. G. Salamanca-Riba, A. A. Iliadis, and K. A. Jones, "Heteroepitaxy of ZnO on GaN and its implications for fabrication of hybrid optoelectronic devices," *Appl. Phys. Lett.*, vol. 73, no. 1998, pp. 348–350, 1998.

[53] C. Czekalla, T. Nobis, A. Rahm, B. Cao, J. Zúñiga-Pérez, C. Sturm, R. Schmidt-Grund, M. Lorenz, and M. Grundmann, "Whispering gallery modes in zinc oxide micro- and nanowires," *Phys. Status Solidi*, vol. 247, no. 6, pp. 1282–1293, 2010.

[54] B. Monemar, P. P. Paskov, J. P. Bergman, A. A. Toropov, T. V. Shubina, T. Malinauskas, and A. Usui, "Recombination of free and bound excitons in GaN," *Phys. Status Solidi Basic Res.*, vol. 245, no. 9, pp. 1723–1740, 2008.

[55] Y. Chen, S. Hong, H. Ko, M. Nakajima, T. Yao, and Y. Segawa, "Plasma-assisted molecular-beam epitaxy of ZnO epilayers on atomically flat MgAl2O4(111) substrates," *Appl. Phys. Lett.*, vol. 76, no. 111, pp. 245–247, 2000.

[56] I. Akasaki, H. Amano, S. Sota, H. Sakai, and T. Tanaka, "Stimulated Emission by Current Injection from an AlGaN/GaN/GaInN Quantum Well," *Jpn. J. Appl. Phys.*, vol. 34, pp. L1517–L1519, 1995.

[57] S. Nakamura, M. Senoh, S.-I. Nagahama, N. Iwasa, T. Yamada, T. Matsushita, Y. Sugimoto, and H. Kiyoku, "Room-temperature continuous-wave operation of InGaN multi-quantum-well-structure laser diodes," *Appl. Phys. Lett.*, vol. 96, no. 26, pp. 4056–4058, 1996.

[58] S. J. Pearton, J. C. Zolper, R. J. Shul, and F. Ren, "GaN: Processing, defects, and devices," *J. Appl. Phys.*, vol. 86, no. 1, pp. 1–78, 1999.

[59] T. Sugahara, H. Sato, M. Hao, Y. Naoi, S. Kurai, S. Tottori, K. Yamashita, K. Nishino, L. T. Romano, and S. Sakai, "Direct Evidence that Dislocations are Non-

Radiative Recombination Centers in GaN," *Jpn. J. Appl. Phys.*, vol. 37, pp. L398–L400, 1998.

[60] V. L. Solozhenko, O. O. Kurakevych, P. S. Sokolov, and A. N. Baranov, "Kinetics of the wurtzite-to-rock-salt phase transformation in ZnO at high pressure," *J. Phys. Chem. A*, vol. 115, no. 17, pp. 4354–4358, 2011.

[61] A. N. Baranov, P. S. Sokolov, V. A. Tafeenko, C. Lathe, Y. V. Zubavichus, A. A. Veligzhanin, M. V. Chukichev, and V. L. Solozhenko, "Nanocrystallinity as a route to metastable phases: Rock salt ZnO," *Chem. Mater.*, vol. 25, no. 9, pp. 1775–1782, 2013.

[62] D. Vanmaekelbergh and L. K. van Vugt, "ZnO nanowire lasers.," *Nanoscale*, vol. 3, no. 7, pp. 2783–800, Jul. 2011.

[63] C. Klingshirn, "ZnO: material, physics and applications.," *Chemphyschem*, vol. 8, no. 6, pp. 782–803, Apr. 2007.

[64] N. J. Nicholas, W. Ducker, and G. V Franks, "Differential etching of ZnO native planes under basic conditions.," *Langmuir*, vol. 28, no. 13, pp. 5633–41, Apr. 2012.

[65] D. Andeen, L. Loeffler, N. Padture, and F. F. Lange, "Crystal chemistry of epitaxial ZnO on (111) MgAl2O4 produced by hydrothermal synthesis," *J. Cryst. Growth*, vol. 259, no. 1–2, pp. 103–109, Nov. 2003.

[66] P. Chul-Hong, "First-Principles Study of the Surface Energy and Atom Cohesion of Wurtzite ZnO and ZnS - Implications for Nanostructure Formation," *J. Korean Phys. Soc.*, vol. 56, no. 12, pp. 498–502, 2010.

[67] M. A. L. Johnson, S. Fujita, W. H. Rowland, W. C. Hughes, J. W. Cook, and J. F. Schetzina, "MBE Growth and Properties of ZnO on Saphire and SiC Substrates," *J. Electron. Mater.*, vol. 25, pp. 855–862, 1996.

[68] J. G. E. Gardeniers, Z. M. Rittersma, and G. J. Burger, "Preferred orientation and piezoelectricity in sputtered ZnO films," *J. Appl. Phys.*, vol. 83, no. 12, pp. 7844–7854, 1998.

[69] P. Fons, K. Iwata, S. Niki, A. Yamada, and K. Matsubara, "Growth of high-quality epitaxial ZnO films on α-Al2O3," *J. Cryst. Growth*, vol. 201, pp. 627–632, 1999.

[70] Y. Liu, C. R. Gorla, S. Liang, N. Emanetoglu, Y. Lu, H. Shen, and M. Wraback, "Ultraviolet detectors based on epitaxial ZnO films grown by MOCVD," *J. Electron. Mater.*, vol. 29, no. 1, pp. 69–74, 2000.

[71] J. Cembrero, A. Elmanouni, B. Hartiti, M. Mollar, and B. Marí, "Nanocolumnar ZnO films for photovoltaic applications," *Thin Solid Films*, vol. 451–452, pp. 198–202, 2004.

[72] H. C. Cheng, C. F. Chen, and C. C. Lee, "Thin-film transistors with active layers of zinc oxide (ZnO) fabricated by low-temperature chemical bath method," *Thin Solid Films*, vol. 498, no. 1–2, pp. 142–145, 2006.

[73] J. Kim and D. Andeen, "Hydrothermal Growth of Periodic, Single-Crystal ZnO Microrods and Microtunnels," *Adv. Mater.*, vol. 18, pp. 2453–2457, 2006.

[74] J. J. Richardson and F. F. Lange, "Controlling Low Temperature Aqueous Synthesis of ZnO. 1. Thermodynamic Analysis," *Cryst. Growth Des.*, vol. 9, no. 6, pp. 2570–2575, 2009.

[75] J. J. Richardson and F. F. Lange, "Rapid synthesis of epitaxial ZnO films from aqueous solution using microwave heating," *J. Mater. Chem.*, vol. 21, no. 6, pp. 1859–1865, 2011.

[76] Y. Chen, D. M. Bagnall, H. Koh, K. Park, K. Hiraga, and Z. Zhu, "Plasma assisted molecular beam epitaxy of ZnO on c -plane sapphire : Growth and characterization," *J. Appl. Phys.*, vol. 84, no. 1998, pp. 3912–3918, 1998.

[77] D. Andeen, J. H. Kim, F. F. Lange, G. K. L. Goh, and S. Tripathy, "Lateral Epitaxial Overgrowth of ZnO in Water at 90 °C," *Adv. Funct. Mater.*, vol. 16, no. 6, pp. 799–804, Apr. 2006.

[78] L. E. Greene, M. Law, D. H. Tan, M. Montano, J. Goldberger, G. Somorjai, and P. Yang, "General route to vertical ZnO nanowire arrays using textured ZnO seeds," *Nano Lett.*, vol. 5, no. 7, pp. 1231–1236, 2005.

[79] M. Law, L. E. Greene, J. C. Johnson, R. Saykally, and P. Yang, "Nanowire dye-sensitized solar cells.," *Nat. Mater.*, vol. 4, no. 6, pp. 455–459, 2005.

[80] K. Govender, D. Boyle, and P. Kenway, "Understanding the factors that govern the deposition and morphology of thin films of ZnO from aqueous solution," *J. Mater. Chem.*, vol. 14, pp. 2575–2591, 2004.

[81] Z. R. Tian, J. A. Voigt, J. Liu, B. McKenzie, M. J. McDermott, M. A. Rodriguez, H. Konishi, and H. Xu, "Complex and oriented ZnO nanostructures.," *Nat. Mater.*, vol. 2, no. 12, pp. 821–6, Dec. 2003.

[82] N. J. Nicholas, G. V Franks, and W. A. Ducker, "Selective adsorption to particular crystal faces of ZnO.," *Langmuir*, vol. 28, no. 18, pp. 7189–96, May 2012.

[83] S. Cho, J.-W. Jang, S.-H. Jung, B. R. Lee, E. Oh, and K.-H. Lee, "Precursor effects of citric acid and citrates on ZnO crystal formation.," *Langmuir*, vol. 25, no. 6, pp. 3825–31, Apr. 2009.

[84] A. Janotti and C. G. Van de Walle, "Native point defects in ZnO," *Phys. Rev. B*, vol. 76, no. 16, p. 165202, Oct. 2007.

[85] A. F. Kohan, G. Ceder, D. Morgan, and C. G. Van de Walle, "First-principles study of native point defects in ZnO," *Phys. Rev. B*, vol. 61, no. 22, pp. 15019–15027, 2000.

[86] C. G. Van De Walle, "Defect analysis and engineering in ZnO," *Phys. B Condens. Matter*, vol. 308–310, pp. 899–903, 2001.

[87] M. Willander, O. Nur, J. R. Sadaf, M. I. Qadir, S. Zaman, A. Zainelabdin, N. Bano, and I. Hussain, "Luminescence from Zinc Oxide Nanostructures and Polymers and their Hybrid Devices," *Materials (Basel).*, vol. 3, no. 4, pp. 2643–2667, Apr. 2010.

[88] M. Liu, A. H. Kitai, and P. Mascher, "Point defects and luminescence centres in zinc oxide and zinc oxide doped with manganese," *J. Lumin.*, vol. 54, no. 1, pp. 35–42, 1992.

[89] K. Vanheusden, C. H. Seager, W. L. Warren, D. R. Tallant, and J. A. Voigt, "Correlation between photoluminescence and oxygen vacancies in ZnO phosphors," *Appl. Phys. Lett.*, vol. 403, no. 1996, pp. 403–405, 1995.

[90] P. H. Kasai, "Electron spin resonance studies of donors and acceptors in ZnO," *Phys. Rev.*, vol. 130, no. 3, pp. 989–995, 1963.

[91] H.-J. Egelhaaf and D. Oelkrug, "Luminescence and nonradiative deactivation of excited states involving oxygen defect centers in polycrystalline ZnO," *J. Cryst. Growth*, vol. 161, no. 1–4, pp. 190–194, 1996.

[92] H. J. Vink, "The Origin of the Fluorescence in Self-Activated ZnS, CdS, and ZnO," *J. Chem. Phys.*, vol. 22, no. 2, pp. 250–252, 1954.

[93] D. C. Reynolds, D. C. Look, B. Jogai, and H. Morkoç, "Similarities in the bandedge and deep-centre photoluminescence mechanisms of ZnO and GaN," *Solid State Commun.*, vol. 101, no. 9, pp. 643–646, 1997.

[94] R. Dingle, "Luminescent transitions associated with divalent copper impurities and the green emission from semiconducting zinc oxide," *Phys. Rev. Lett.*, vol. 23, no. 11, pp. 579–581, 1969.

[95] W. Lehmann, "Zinc Oxide and Zinc-Cadmium Oxide Phosphors," *J. Electrochem. Soc.*, vol. 115, no. 5, pp. 538–540, 1968.

[96] O. F. Schirmer and D. Zwingel, "The Yellow Luminescence of Zinc Oxide," *Solid State Commun.*, vol. 8, pp. 1559–1563, 1970.

[97] D. Li, Y. H. Leung, A. B. Djurišić, Z. T. Liu, M. H. Xie, S. L. Shi, S. J. Xu, and W. K. Chan, "Different origins of visible luminescence in ZnO nanostructures fabricated by the chemical and evaporation methods," *Appl. Phys. Lett.*, vol. 85, no. 9, pp. 1601–1603, 2004.

[98] A. B. Djurišić, Y. H. Leung, K. H. Tam, Y. F. Hsu, L. Ding, W. K. Ge, Y. C. Zhong, K. S. Wong, W. K. Chan, H. L. Tam, K. W. Cheah, W. M. Kwok, and D. L. Phillips, "Defect emissions in ZnO nanostructures," *Nanotechnology*, vol. 18, no. 9, p. 095702, Mar. 2007.

[99] D. G. Thomas and J. J. Lander, "Donor in Zinc Oxide," *J. Chem. Phys.*, vol. 25, no. 6, pp. 1136–1142, 1954.

[100] A. R. Hutson, "Hall effect studies of doped zinc Oxide single crystals," *Phys. Rev.*, vol. 108, no. 2, pp. 222–230, 1957.

[101] D. Look, J. Hemsky, and J. Sizelove, "Residual Native Shallow Donor in ZnO," *Phys. Rev. Lett.*, vol. 82, no. 12, pp. 2552–2555, 1999.

[102] C. G. Van De Walle, "Hydrogen as a cause of doping in zinc oxide," *Phys. Rev. Lett.*, vol. 85, no. 5, pp. 1012–1015, 2000.

[103] D. M. Hofmann, A. Hofstaetter, F. Leiter, H. Zhou, F. Henecker, B. K. Meyer, S. B. Orlinskii, J. Schmidt, and P. G. Baranov, "Hydrogen: a relevant shallow donor in zinc oxide.," *Phys. Rev. Lett.*, vol. 88, no. 4, p. 045504, 2002.

[104] J. I. Pankove and N. M. Johnson, "Hydrogen in Semiconductors," in *Semiconductors and Semimetals*, Vol. 34., Academic Press, Boston, 1991.

[105] S. F. J. Cox, E. A. Davis, S. P. Cottrell, P. J. C. King, J. S. Lord, J. M. Gil, H. V. Alberto, R. C. Vilao, J. P. Duarte, N. A. De Campos, A. Weidinger, R. L. Lichti, and S. J. C. Irvine, "Experimental confirmation of the predicted shallow donor hydrogen state in zinc oxide," *Phys. Rev. Lett.*, vol. 86, no. 12, pp. 2601–2604, 2001.

[106] Y. M. Strzhemechny, H. L. Mosbacker, D. C. Look, D. C. Reynolds, C. W. Litton, N. Y. Garces, N. C. Giles, L. E. Halliburton, S. Niki, and L. J. Brillson, "Remote hydrogen plasma processing of ZnO single crystal surfaces," *Appl. Phys. Lett.*, vol. 84, no. 14, pp. 2545–2547, 2004.

[107] J. J. Richardson, G. K. L. Goh, H. Q. Le, L.-L. Liew, F. F. Lange, and S. P. DenBaars, "Thermally Induced Pore Formation in Epitaxial ZnO Films Grown from Low Temperature Aqueous Solution," *Cryst. Growth Des.*, vol. 11, no. 8, pp. 3558–3563, 2011.

[108] N. Saito, H. Haneda, T. Sekiguchi, T. Ishigaki, and K. Koumoto, "Effect of Postdeposition Annealing on Luminescence from Zinc Oxide Patterns Prepared by the Electroless Deposition Process," *J. Electrochem. Soc.*, 2004.

[109] F. Maldonado and A. Stashans, "Al-doped ZnO: Electronic, electrical and structural properties," *J. Phys. Chem. Solids*, vol. 71, no. 5, pp. 784–787, 2010.

[110] Z. Ben Ayadi, L. El Mir, K. Djessas, and S. Alaya, "Electrical and optical properties of aluminum-doped zinc oxide sputtered from an aerogel nanopowder target," *Nanotechnology*, vol. 18, no. 44, p. 445702, 2007.

[111] V. Bhosle, A. Tiwari, and J. Narayan, "Electrical properties of transparent and conducting Ga doped ZnO," *J. Appl. Phys.*, vol. 100, p. 033713, 2006.

[112] H. J. Ko, Y. F. Chen, S. K. Hong, H. Wenisch, T. Yao, and D. C. Look, "Ga-doped ZnO films grown on GaN templates by plasma-assisted molecular-beam epitaxy," *Appl. Phys. Lett.*, vol. 77, no. 23, pp. 3761–3763, 2000.

[113] R. Biswal, A. Maldonado, J. Vega-Pérez, D. R. Acosta, and M. D. L. L. Olvera, "Indium doped zinc oxide thin films deposited by ultrasonic chemical spray technique, starting from zinc acetylacetonate and indium chloride," *Materials (Basel).*, vol. 7, no. 7, pp. 5038–5046, 2014.

[114] F. Wang, J. H. Seo, Z. Li, A. V. Kvit, Z. Ma, and X. Wang, "Cl-doped ZnO nanowires with metallic conductivity and their application for high-performance photoelectrochemical electrodes," *ACS Appl. Mater. Interfaces*, vol. 6, no. 2, pp. 1288–1293, 2014.

[115] Y. Z. Zheng, X. Tao, Q. Hou, D. T. Wang, W. L. Zhou, and J. F. Chen, "Iodine-doped ZnO nanocrystalline aggregates for improved dye-sensitized solar cells," *Chem. Mater.*, vol. 23, no. 1, pp. 3–5, 2011.

[116] S. Vunnam, K. Ankireddy, J. Kellar, and W. Cross, "Highly transparent and conductive Al-doped ZnO nanoparticulate thin films using direct write processing.," *Nanotechnology*, vol. 25, no. 19, p. 195301, 2014.

[117] Z. Q. Fang, B. Claflin, D. C. Look, L. L. Kerr, and X. Li, "Electron and hole traps in N-doped ZnO grown on p -type Si by metalorganic chemical vapor deposition," *J. Appl. Phys.*, vol. 102, no. 2, pp. 1–6, 2007.

[118] Y. Ryu, S. Zhu, D. Look, and J. Wrobel, "Synthesis of p-type ZnO films," *J. Cryst. Growth*, vol. 216, pp. 330–334, 2000.

[119] D. C. Look, G. M. Renlund, R. H. Burgener, and J. R. Sizelove, "As-doped p-type ZnO produced by an evaporation/sputtering process," *Appl. Phys. Lett.*, vol. 85, no. 22, pp. 5269–5271, 2004.

[120] V. Vaithianathan, B.-T. Lee, C.-H. Chang, K. Asokan, and S. S. Kim, "Characterization of As-doped, p-type ZnO by x-ray absorption near-edge structure spectroscopy," *Appl. Phys. Lett.*, vol. 88, no. 11, p. 112103, 2006.

[121] S. Jang, J. J. Chen, B. S. Kang, F. Ren, D. P. Norton, S. J. Pearton, J. Lopata, and W. S. Hobson, "Formation of p-n homojunctions in n-ZnO bulk single crystals by diffusion from a Zn 3P 2 source," *Appl. Phys. Lett.*, vol. 87, no. 22, pp. 1–3, 2005.

[122] L. J. Mandalapu, Z. Yang, F. X. Xiu, D. T. Zhao, and J. L. Liu, "Homojunction photodiodes based on Sb-doped p-type ZnO for ultraviolet detection," *Appl. Phys. Lett.*, vol. 88, no. 9, pp. 1–4, 2006.

[123] J. G. Lu, Y. Z. Zhang, Z. Z. Ye, Y. J. Zeng, H. P. He, L. P. Zhu, J. Y. Huang, L. Wang, J. Yuan, B. H. Zhao, and X. H. Li, "Control of p- and n-type conductivities in Li-doped ZnO thin films," *Appl. Phys. Lett.*, vol. 89, no. 11, pp. 2004–2007, 2006.

[124] A. B. Djurisić and Y. H. Leung, "Optical properties of ZnO nanostructures.," *Small*, vol. 2, no. 8–9, pp. 944–61, Aug. 2006.

[125] A. B. Djurišić, W. C. H. Choy, V. A. L. Roy, Y. H. Leung, C. Y. Kwong, K. W. Cheah, T. K. Gundu Rao, W. K. Chan, H. Fei Lui, and C. Surya, "Photoluminescence and Electron Paramagnetic Resonance of ZnO Tetrapod Structures," *Adv. Funct. Mater.*, vol. 14, no. 9, pp. 856–864, Sep. 2004.

[126] P. A. Rodnyi and I. V. Khodyuk, "Optical and luminescence properties of zinc oxide (Review)," *Opt. Spectrosc.*, vol. 111, no. 5, pp. 776–785, Dec. 2011.

[127] D. C. Reynolds, D. C. Look, B. Jogai, J. E. Van Nostrand, R. Jones, J. Jenny, A. Directorate, and W. A. F. Base, "Source of the yellow luminescence band in GaN grown by gas-source molecular beam epitaxy and the green luminescence band in single crystal ZnO," vol. 106, no. 10, pp. 701–704, 1998.

[128] V. Srikant and D. R. Clarke, "On the optical band gap of zinc oxide," *J. Appl. Phys.*, vol. 83, no. 10, pp. 5447–5451, 1998.

[129] J. H. Joo, K. J. Greenberg, M. Baram, D. R. Clarke, and E. L. Hu, "Aqueous Epitaxial Growth of ZnO on Single Crystalline Au Microplates," *Cryst. Growth Des.*, vol. 13, no. 3, pp. 986–991, Mar. 2013.

[130] B. K. Meyer, H. Alves, D. M. Hofmann, W. Kriegseis, D. Forster, F. Bertram, J. Christen, A. Hoffmann, M. Straßburg, M. Dworzak, U. Haboeck, and A. V. Rodina, "Bound exciton and donor–acceptor pair recombinations in ZnO," *Phys. Status Solidi*, vol. 241, no. 2, pp. 231–260, Feb. 2004.

[131] D. C. Look, "Recent advances in ZnO materials and devices," *Mater. Sci. Eng. B*, vol. 80, pp. 383–387, Mar. 2001.

[132] D. G. Thomas, “The Exciton Spectrum of Zinc Oxide,” *J. Phys. Chem. Solids*, vol. 15, pp. 86–96, 1960.

[133] E. Mallet, P. Disseix, D. Lagarde, M. Mihailovic, F. Réveret, T. V. Shubina, and J. Leymarie, “Accurate determination of homogeneous and inhomogeneous excitonic broadening in ZnO by linear and nonlinear spectroscopies,” *Phys. Rev. B*, vol. 87, no. 16, p. 161202, Apr. 2013.

[134] S. Margueron and D. R. Clarke, “The high temperature photoluminescence and optical absorption of undoped ZnO single crystals and thin films,” *J. Appl. Phys.*, vol. 116, no. 19, p. 193101, Nov. 2014.

[135] R. Hauschild, H. Priller, M. Decker, J. Brückner, H. Kalt, and C. Klingshirn, “Temperature dependent band gap and homogeneous line broadening of the exciton emission in ZnO,” *Phys. Status Solidi*, vol. 3, no. 4, pp. 976–979, Mar. 2006.

[136] X.-B. Chen, J. Huso, J. L. Morrison, and L. Bergman, “The properties of ZnO photoluminescence at and above room temperature,” *J. Appl. Phys.*, vol. 102, no. 11, p. 116105, 2007.

[137] J. J. Richardson, D. Estrada, S. P. DenBaars, C. J. Hawker, and L. M. Campos, “A facile route to patterned epitaxial ZnO nanostructures by soft lithography,” *J. Mater. Chem.*, vol. 21, no. 38, p. 14417, 2011.

[138] D. B. Thompson, J. J. Richardson, S. P. DenBaars, and F. F. Lange, “Light Emitting Diodes with ZnO Current Spreading Layers Deposited from a Low Temperature Aqueous Solution,” *Appl. Phys. Express*, vol. 2, p. 042101, Mar. 2009.

[139] K. H. Tam, C. K. Cheung, Y. H. Leung, A. B. Djuris, S. Fung, W. M. Kwok, W. K. Chan, D. L. Phillips, L. Ding, and W. K. Ge, “Defects in ZnO Nanorods Prepared by a Hydrothermal Method,” *J. Phys. Chem B*, pp. 20865–20871, 2006.

[140] X. L. Wu, G. G. Siu, C. L. Fu, and H. C. Ong, “Photoluminescence and cathodoluminescence studies of stoichiometric and oxygen-deficient ZnO films,” *Appl. Phys. Lett.*, vol. 78, no. 16, p. 2285, 2001.

[141] B. Lin, Z. Fu, and Y. Jia, “Green luminescent center in undoped zinc oxide films deposited on silicon substrates,” *Appl. Phys. Lett.*, vol. 79, no. 7, pp. 943–945, 2001.

[142] B. J. Jin, S. H. Bae, S. Y. Lee, and S. Im, “Effects of native defects on optical and electrical properties of ZnO prepared by pulsed laser deposition,” *Mater. Sci. Eng. B*, vol. 71, pp. 301–305, Feb. 2000.

[143] C. F. Klingshirn, A. Waag, A. Hoffmann, and J. Geurts, *Zinc Oxide: From Fundamental Properties Towards Novel Applications*. Springer, 2010.

[144] J. Schubert, O. Trithaveesak, A. Petraru, C. L. Jia, R. Uecker, P. Reiche, and D. G. Schlom, "Structural and optical properties of epitaxial BaTiO3 thin films grown on GdScO3(110)," *Appl. Phys. Lett.*, vol. 82, no. 20, pp. 3460–3462, 2003.

[145] K. Ozawa and K. Mase, "Angle-resolved photoelectron spectroscopy study of hydrogen adsorption on ZnO($10-10)," *Phys. Status Solidi*, vol. 207, no. 2, pp. 277–281, Feb. 2010.

[146] R. Laiho, Y. P. Stepanov, M. P. Vlasenko, and L. S. Vlasenko, "Persistent photoconductivity of ZnO," *Phys. B Condens. Matter*, vol. 404, no. 23–24, pp. 4787–4790, Dec. 2009.

[147] D. Cammi and C. Ronning, "Persistent Photoconductivity in ZnO Nanowires in Different Atmospheres," *Adv. Condens. Matter Phys.*, vol. 2014, pp. 1–5, 2014.

[148] S. Hullavarad, N. Hullavarad, D. Look, and B. Claflin, "Persistent Photoconductivity Studies in Nanostructured ZnO UV Sensors.," *Nanoscale Res. Lett.*, vol. 4, no. 12, pp. 1421–7, Jan. 2009.

[149] H.-H. Nahm, C. H. Park, and Y.-S. Kim, "Bistability of hydrogen in ZnO: origin of doping limit and persistent photoconductivity.," *Nature*, vol. 4, pp. 1–5, Jan. 2014.

[150] R. L. Hoffman, B. J. Norris, and J. F. Wager, "ZnO-based transparent thin-film transistors," *Appl. Phys. Lett.*, vol. 82, no. 5, pp. 733–735, 2003.

[151] R. R. Li, P. D. Dapkus, M. E. Thompson, W. G. Jeong, C. Harrison, P. M. Chaikin, R. A. Register, and D. H. Adamson, "Dense arrays of ordered GaAs nanostructures by selective area growth on substrates patterned by block copolymer lithography," *Appl. Phys. Lett.*, vol. 76, no. 13, pp. 1689–1691, 2000.

[152] Y.-J. Kim, C.-H. Lee, Y. J. Hong, G.-C. Yi, S. S. Kim, and H. Cheong, "Controlled selective growth of ZnO nanorod and microrod arrays on Si substrates by a wet chemical method," *Appl. Phys. Lett.*, vol. 89, no. 16, p. 163128, 2006.

[153] H. P. Sun, X. Q. Pan, X. L. Du, Z. X. Mei, Z. Q. Zeng, and Q. K. Xue, "Microstructure and crystal defects in epitaxial ZnO film grown on Ga modified (0001) sapphire surface," *Appl. Phys. Lett.*, vol. 85, no. 19, pp. 4385–4387, 2004.

[154] A. Krost, J. Christen, N. Oleynik, A. Dadgar, S. Deiter, J. Bläsing, A. Krtschil, D. Forster, F. Bertram, and A. Diez, "Ostwald ripening and flattening of epitaxial ZnO layers during in situ annealing in metalorganic vapor phase epitaxy," *Appl. Phys. Lett.*, vol. 85, no. 9, pp. 1496–1498, 2004.

[155] Y. Cui, G. Du, Y. Zhang, H. Zhu, and B. Zhang, "Growth of ZnO(002) and ZnO(100) films on GaAs substrates by MOCVD," *J. Cryst. Growth*, vol. 282, pp. 389–393, Sep. 2005.

[156] G. P. Li, L. Jiang, S. J. Wang, X. W. Sun, X. Chen, and T. Wu, "Buffer-Layer-Assisted Epitaxial Growth of Perfectly Aligned Oxide Nanorod Arrays in Solution," *Cryst. Growth Des.*, vol. 11, no. 11, pp. 4885–4891, Nov. 2011.

[157] S. I. Wright and M. M. Nowell, "EBSD Image Quality Mapping," *Microsc. Microanal.*, vol. 12, no. 1, pp. 72–84, 2006.

[158] T. L. Sounart, J. Liu, J. A. Voigt, M. Huo, E. D. Spoerke, and B. Mckenzie, "Secondary Nucleation and Growth of ZnO," *J. Am. Chem. Soc.*, vol. 129, no. 6, pp. 15786–15793, 2007.

[159] K. C. Kao and G. A. Hockham, "Dielectric-fibre surface waveguides for optical frequencies," *Proc. Inst. Electr. Eng.*, vol. 113, pp. 1151–1158, 1966.

[160] K. C. Kao and T. W. Davies, "Spectrophotometric studies of ultra low loss optical glasses. I. Single beam method.," *J. Sci. Instrum.*, vol. 1, pp. 1063–1072, 1968.

[161] M. W. Jones and K. C. Kao, "Spectrophotometric studies of ultra low loss optical glasses II: double beam method," *J. Phys. E.*, vol. 2, pp. 331–335, 1969.

[162] C. R. Wright and K. C. Kao, "Spectrophotometric studies of ultra low loss optical glasses lll: ellipsometric determination of surface reflectances," *J. Phys. E.*, vol. 2, pp. 579–583, 1969.

[163] R. N. Hall, G. E. Fenner, J. D. Kingsley, T. J. Soltys, and R. O. Carlson, "Coherent light emission from GaAs junctions," *Phys. Rev. Lett.*, vol. 9, no. 9, pp. 366–368, 1962.

[164] N. Holonyak and S. F. Bevacqua, "Coherent (visible) light emission from Ga(As1-xPx) junctions," *Appl. Phys. Lett.*, vol. 1, no. 4, pp. 82–83, 1962.

[165] M. I. Nathan, W. P. Dumke, G. Burns, F. H. Dill, and G. Lasher, "Stimulated emission of radiation from GaAs p-n junctions," *Appl. Phys. Lett.*, vol. 1, no. 1962, pp. 62–64, 1962.

[166] M. Gershenzon and R. M. Mikulyak, "Light emission from forward biased p-n junctions in gallium phosphide," *Solid. State. Electron.*, vol. 5, pp. 313–329, 1962.

[167] J. N. Shive, "Semiconductor photoelectric device," 1953.

[168] F. Xia, T. Mueller, Y.-M. Lin, A. Valdes-Garcia, and P. Avouris, "Ultrafast graphene photodetector," *Nat. Nanotechnol.*, vol. 4, no. 12, pp. 839–843, 2009.

[169] Z. Huang, J. E. Carey, M. Liu, X. Guo, E. Mazur, and J. C. Campbell, "Microstructured silicon photodetector," *Appl. Phys. Lett.*, vol. 89, pp. 14–17, 2006.

[170] H. C. Liu, C. Y. Song, A. J. SpringThorpe, and J. C. Cao, "Terahertz quantum-well photodetector," *Appl. Phys. Lett.*, vol. 84, pp. 4068–4070, 2004.

[171] T. H. Maiman, "Stimulated Optical Radiation in Ruby," *Nature*, vol. 187, pp. 493–494, 1960.

[172] T. Y. Fan and R. L. Byer, "Diode Laser-Pumped Solid-State Lasers," *IEEE J. Quantum Electron.*, vol. 24, no. 6, pp. 895–912, 1988.

[173] W. F. Krupke, "Ytterbium solid-state lasers - the first decade," *IEEE J. Sel. Top. Quantum Electron.*, vol. 6, no. 6, pp. 1287–1296, 2000.

[174] M. Mahlingam, "Thermal management in semiconductor device packaging," *Proc. IEEE*, vol. 73, no. 9, pp. 1396–1404, 1985.

[175] D. J. Frank, "Power- constrained CMOS scaling limits," *IBM J. Res. Dev.*, vol. 46, no. 2, pp. 235–244, 2002.

[176] S. Borkar, "Design challenges of technology scaling," *IEEE Micro*, vol. 19, pp. 23–29, 1999.

[177] Wgsimon, "Transistor Count and Moore's Law," *Wikipedia*, 2011. [Online]. Available: http://commons.wikimedia.org/wiki/File:Transistor_Count_and_Moore%27s_Law_-_2011.svg. [Accessed: 03-Jan-2015].

[178] D. James, "Intel Ivy Bridge unveiled - The first commercial tri-gate, high-k, metal-gate CPU," *Proc. Cust. Integr. Circuits Conf.*, pp. 5–8, 2012.

[179] S. Damaraju, V. George, S. Jahagirdar, T. Khondker, R. Milstrey, S. Sarkar, S. Siers, I. Stolero, and A. Subbiah, "A 22nm IA Multi-CPU and GPU System-on-Chip," in *2012 IEEE International Solid-State Circuits Conference*, 2012, vol. 44, no. 4, pp. 56–57.

[180] Y.-M. Lin, A. Valdes-Garcia, S.-J. Han, D. Farmer, I. Meric, Y. Sun, Y. Wu, C. Dimitrakopoulos, A. Grill, P. Avouris, and K. Jenkins, "Wafer-Scale Graphene Integrated Circuit," *Science (80-.).*, vol. 332, no. June, pp. 1294–1298, 2011.

[181] S.-J. Han, A. V. Garcia, S. Oida, K. A. Jenkins, and W. Haensch, "Graphene radio frequency receiver integrated circuit.," *Nat. Commun.*, vol. 5, p. 3086, 2014.

[182] S. Assefa, F. Xia, W. M. J. Green, C. L. Schow, A. V. Rylyakov, and Y. A. Vlasov, "CMOS-integrated optical receivers for on-chip interconnects," *IEEE J. Sel. Top. Quantum Electron.*, vol. 16, no. 5, pp. 1376–1385, 2010.

[183] K. J. Vahala, "Optical microcavities," *Nature*, vol. 424, pp. 839–846, 2003.

[184] V. Lefèvre-Seguin and S. Haroche, “Towards cavity-QED experiments with silica microspheres,” *Mater. Sci. Eng. B*, vol. 48, pp. 53–58, 1997.

[185] D. W. Vernooy, V. S. Ilchenko, H. Mabuchi, E. W. Streed, and H. J. Kimble, “High-Q measurements of fused-silica microspheres in the near infrared.,” *Opt. Lett.*, vol. 23, no. 4, pp. 247–249, 1998.

[186] M. L. Gorodetsky, A. A. Savchenkov, and V. S. Ilchenko, “Ultimate Q of optical microsphere resonators.,” *Opt. Lett.*, vol. 21, no. 7, pp. 453–455, 1996.

[187] B. Gayral, J.-M. Gérard, A. Lemaître, C. Dupuis, L. Manin, and J. L. Pelouard, “High-Q wet-etched GaAs microdisks containing InAs quantum boxes,” *Appl. Phys. Lett.*, vol. 75, no. 1999, pp. 1908–1910, 1999.

[188] V. Sandoghdar, F. Treussart, J. Hare, V. Lefèvre-Seguin, J. Raimond, and S. Haroche, “Very low threshold whispering-gallery-mode microsphere laser,” *Phys. Rev. A*, vol. 54, no. 3, pp. R1777–R1780, 1996.

[189] S. L. McCall, A. F. J. Levi, R. E. Slusher, S. J. Pearton, and R. A. Logan, “Whispering-gallery mode microdisk lasers,” *Appl. Phys. Lett.*, vol. 60, no. 1992, pp. 289–291, 1992.

[190] E. Krioukov, J. Greve, and C. Otto, “Performance of integrated optical microcavities for refractive index and fluorescence sensing,” *Sensors Actuators, B Chem.*, vol. 90, pp. 58–67, 2003.

[191] E. Krioukov, D. J. W. Klunder, A. Driessen, J. Greve, and C. Otto, “Sensor based on an integrated optical microcavity.,” *Opt. Lett.*, vol. 27, no. 7, pp. 512–514, 2002.

[192] M. A. Pooley, D. J. P. Ellis, R. B. Patel, a. J. Bennett, K. H. a Chan, I. Farrer, D. a. Ritchie, and a. J. Shields, “Controlled-NOT gate operating with single photons,” *Appl. Phys. Lett.*, vol. 100, p. 211103, 2012.

[193] A. Schwagmann, S. Kalliakos, D. J. P. Ellis, I. Farrer, J. P. Griffiths, G. a C. Jones, D. A. Ritchie, and A. J. Shields, “In-plane single-photon emission from a L3 cavity coupled to a photonic crystal waveguide.,” *Opt. Express*, vol. 20, no. 27, pp. 28614–24, 2012.

[194] A. C. Tamboli, E. D. Haberer, R. Sharma, K. H. Lee, S. Nakamura, and E. L. Hu, “Room-temperature continuous-wave lasing in GaN/InGaN microdisks,” *Nat. Photonics*, vol. 1, pp. 61–64, 2007.

[195] A. Woolf, “Low-threshold indium gallium nitride quantum dot microcavity lasers,” Harvard University, 2014.

[196] J. C. Lee, I. Aharonovich, A. P. Magyar, F. Rol, and E. L. Hu, "Coupling of silicon-vacancy centers to a single crystal diamond cavity," *Opt. Express*, vol. 20, no. 8, pp. 8891–8897, 2012.

[197] U. Mohideen, W. S. Hobson, S. J. Pearton, F. Ren, and R. E. Slusher, "GaAs/AlGaAs microdisk lasers," *Appl. Phys. Lett.*, vol. 64, no. 1994, pp. 1911–1913, 1994.

[198] M. Soltani, S. Yegnanarayanan, and A. Adibi, "Ultra-high Q planar silicon microdisk resonators for chip-scale silicon photonics.," *Opt. Express*, vol. 15, no. 8, pp. 4694–704, Apr. 2007.

[199] R. Chen, B. Ling, X. W. Sun, and H. D. Sun, "Room temperature excitonic whispering gallery mode lasing from high-quality hexagonal ZnO microdisks.," *Adv. Mater.*, vol. 23, no. 19, pp. 2199–204, May 2011.

[200] K. K. M. Wang, S. H. Hahn, J. S. Kim, J. S. Chung, E. J. Kim, "Solvent controlled crystallization of zinc oxide nano(micro) disks.pdf," *J. Cryst. Growth*, vol. 310, pp. 1213–1219, 2008.

[201] D. Yu, Y. Chen, B. Li, X. Chen, M. Zhang, F. Zhao, and S. Ren, "Structural and lasing characteristics of ultrathin hexagonal ZnO nanodisks grown vertically on silicon-on-insulator substrates," *Appl. Phys. Lett.*, vol. 91, no. 9, p. 091116, 2007.

[202] J. Dai, C. X. Xu, X. W. Sun, and X. H. Zhang, "Exciton-polariton microphotoluminescence and lasing from ZnO whispering-gallery mode microcavities," *Appl. Phys. Lett.*, vol. 98, no. 16, p. 161110, 2011.

[203] G. Dai, Y. Zhang, R. Liu, Q. Wan, Q. Zhang, A. Pan, and B. Zou, "Visible whispering-gallery modes in ZnO microwires with varied cross sections," *J. Appl. Phys.*, vol. 110, no. 2011, p. 033101, 2011.

[204] C. Czekalla, C. Sturm, R. Schmidt-Grund, B. Cao, M. Lorenz, and M. Grundmann, "Whispering gallery mode lasing in zinc oxide microwires," *Appl. Phys. Lett.*, vol. 92, p. 241102, 2008.

[205] T. Nobis, E. M. Kaidashev, A. Rahm, M. Lorenz, and M. Grundmann, "Whispering gallery modes in nanosized dielectric resonators with hexagonal cross section," *Phys. Rev. Lett.*, vol. 93, no. 10, p. 103903, 2004.

[206] Q. Xu and M. Lipson, "All-optical logic based on silicon micro-ring resonators.," *Opt. Express*, vol. 15, no. 3, pp. 924–929, 2007.

[207] P. P. Absil, J. V Hryniewicz, B. E. Little, P. S. Cho, R. A. Wilson, L. G. Joneckis, and P. T. Ho, "Wavelength conversion in GaAs micro-ring resonators.," *Opt. Lett.*, vol. 25, no. 8, pp. 554–556, 2000.

[208] D. G. Rabus, Z. Bian, and A. Shakouri, "A GaInAsP-InP double-ring resonator coupled laser," *IEEE Photonics Technol. Lett.*, vol. 17, no. 9, pp. 1770–1772, 2005.

[209] Y. Sun and X. Fan, "Optical ring resonators for biochemical and chemical sensing," *Anal. Bioanal. Chem.*, vol. 399, pp. 205–211, 2011.

[210] P. Rabiei, W. H. Steier, C. Zhang, and L. R. Dalton, "Polymer micro-ring filters and modulators," *J. Light. Technol.*, vol. 20, no. 11, pp. 1968–1975, 2002.

[211] S. Suzuki, Y. Hatakeyama, Y. Kokubun, and S. T. Chu, "Precise control of wavelength channel spacing of microring resonator add-drop filter array," *J. Light. Technol.*, vol. 20, no. 4, pp. 745–750, 2002.

[212] V. Jindal and F. Shahedipour-Sandvik, "Theoretical prediction of GaN nanostructure equilibrium and nonequilibrium shapes," *J. Appl. Phys.*, vol. 106, p. 083115, 2009.

[213] S. Y. Lin, J. G. Fleming, D. L. Hetherington, B. K. Smith, R. Biswas, K. M. Ho, M. M. Sigalas, W. Zubrzycki, S. R. Kurtz, and J. Bur, "A three-dimensional photonic crystal operating at infrared wavelengths," *Nature*, vol. 394, pp. 251–253, 1998.

[214] Y. Akahane, T. Asano, and B. Song, "High- Q photonic nanocavity in a two-dimensional photonic crystal," *Nature*, vol. 425, pp. 944–947, 2003.

[215] K. Srinivasan and O. Painter, "Momentum space design of high-Q photonic crystal optical cavities.," *Opt. Express*, vol. 10, no. 15, pp. 670–684, 2002.

[216] T. Xu, N. Zhu, M. Y.-C. Xu, L. Wosinski, J. S. Aitchison, and H. E. Ruda, "A pillar-array based two-dimensional photonic crystal microcavity," *Appl. Phys. Lett.*, vol. 94, p. 241110, 2009.

[217] T. Xu, S. Yang, S. V. Nair, and H. E. Ruda, "Confined modes in finite-size photonic crystals," *Phys. Rev. B - Condens. Matter Mater. Phys.*, vol. 72, p. 045126, 2005.

[218] M. Loncar, T. Doll, J. Vuckovic, and A. Scherer, "Design and fabrication of silicon photonic crystal optical waveguides," *J. Light. Technol.*, vol. 18, no. 10, pp. 1402–1411, 2000.

[219] M. Notomi, T. Tanabe, A. Shinya, E. Kuramochi, and H. Taniyama, "On-Chip All-Optical Switching and Memory by Silicon Photonic Crystal Nanocavities," *Adv. Opt. Technol.*, vol. 2008, pp. 1–10, 2008.

[220] E. Chow, S. Y. Lin, S. G. Johnson, P. R. Villeneuve, J. D. Joannopoulos, J. R. Wendt, G. A. Vawter, W. Zubrzycki, H. Hou, and A. Alleman, "Three-dimensional control of light in a two-dimensional photonic crystal slab.," *Nature*, vol. 407, pp. 983–6, 2000.

[221] D. Mascoli, D. Gerace, and L. C. Andreani, "Q-factor optimization for TM-like modes in pillar-based photonic crystal cavities with planar slot waveguides," *Photonics Nanostructures - Fundam. Appl.*, vol. 9, no. 1, pp. 63–69, 2011.

[222] T. Zijlstra, E. Van der Drift, M. J. A. de Dood, E. Snoeks, and A. Polman, "Fabrication of two-dimensional photonic crystal waveguides for 1.5 μm in silicon by deep anisotropic dry etching," *J. Vac. Sci. Technol. B Microelectron. Nanom. Struct.*, vol. 17, no. 6, pp. 2734–2739, 1999.

[223] J. R. Weber, W. F. Koehl, J. B. Varley, A. Janotti, B. B. Buckley, C. G. Van de Walle, and D. D. Awschalom, "Quantum computing with defects.," *Proc. Natl. Acad. Sci. U. S. A.*, vol. 107, no. 19, pp. 8513–8518, 2010.

[224] M. Matsuu, S. Shimada, K. Masuya, S. Hirano, and M. Kuwabara, "Formation of Periodically Ordered Zinc Oxide Nanopillars in Aqueous Solution: An Approach to Photonic Crystals at Visible Wavelengths," *Adv. Mater.*, vol. 18, no. 12, pp. 1617–1621, Jun. 2006.

[225] J. Cui and U. Gibson, "Low-temperature fabrication of single-crystal ZnO nanopillar photonic bandgap structures," vol. 155302, 2007.

[226] R. T. Tung, "Schottky barrier height—do we really understand what we measure?," *J. Vac. Sci. Technol. B Microelectron. Nanom. Struct.*, vol. 11, pp. 1546–1552, 1993.

[227] K. J. Russell, T.-L. Liu, S. Cui, and E. L. Hu, "Large spontaneous emission enhancement in plasmonic nanocavities," *Nat. Photonics*, vol. 6, no. July, pp. 459–462, 2012.

[228] Y.-J. Lu, J. Kim, H.-Y. Chen, C. Wu, N. Dabidian, C. E. Sanders, C.-Y. Wang, M.-Y. Lu, B.-H. Li, X. Qiu, W.-H. Chang, L.-J. Chen, G. Shvets, C.-K. Shih, and S. Gwo, "Plasmonic Nanolaser Using Epitaxially Grown Silver Film," *Science (80-.).*, vol. 337, pp. 450–453, 2012.

[229] M. W. Knight, H. Sobhani, P. Nordlander, and N. J. Halas, "Photodetection with Active Optical Antennas," *Science (80-.).*, vol. 332, pp. 702–704, 2011.

[230] K. Ip, G. T. Thaler, H. Yang, S. Y. Han, Y. Li, D. P. Norton, S. J. Pearton, S. Jang, and F. Ren, "Contacts to ZnO," *J. Cryst. Growth*, vol. 287, pp. 149–156, 2006.

[231] M. Gwon, E. Lee, D.-W. Kim, K.-J. Yee, M. J. Lee, and Y. S. Kim, "Surface-plasmon-enhanced visible-light emission of ZnO/Ag grating structures.," *Opt. Express*, vol. 19, no. 7, pp. 5895–5901, 2011.

[232] B. . J. Lawrie, R. Mu, and R. F. Haglund, "Selective Purcell enhancement of defect emission in ZnO thin films," *Opt. Lett.*, vol. 37, pp. 1538–1540, 2012.

[233] P. Kundu, N. Singhania, G. Madras, and N. Ravishankar, "ZnO–Au nanohybrids by rapid microwave-assisted synthesis for CO oxidation," *Dalt. Trans.*, vol. 41, pp. 8762–8766, 2012.

[234] P. Li, Z. Wei, T. Wu, Q. Peng, and Y. Li, "Au-ZnO hybrid nanopyramids and their photocatalytic properties," *J. Am. Chem. Soc.*, vol. 133, pp. 5660–5663, 2011.

[235] H. A. Herman and H. Sitter, *Molecular beam epitaxy: Fundamentals and current status*. Springer, 1989.

[236] D. Leonard, M. Krishnamurthy, C. M. Reaves, S. P. Denbaars, and P. M. Petroff, "Direct formation of quantum-sized dots from uniform coherent islands of InGaAs on GaAs surfaces," *Appl. Phys. Lett.*, vol. 63, no. 23, pp. 3203–3205, 1993.

[237] C. Gorla and N. Emanetoglu, "Structural, optical, and surface acoustic wave properties of epitaxial ZnO films grown on (01-12) sapphire by metalorganic chemical vapor deposition," *J. Appl. Phys.*, vol. 85, pp. 2595–2602, 1999.

[238] J. De Boeck, W. Van Roy, V. Motsnyi, Z. Liu, K. Dessein, and G. Borghs, "Hybrid epitaxial structures for spintronics," *Thin Solid Films*, vol. 412, pp. 3–13, 2002.

[239] Y. Yoshino, K. Inoue, M. Takeuchi, and K. Ohwada, "Effects of interface micro structure in crystallization of ZnO thin films prepared by radio frequency sputtering," *Vacuum*, vol. 51, no. 4, pp. 601–607, Dec. 1998.

[240] F. C. Nix and D. MacNair, "The thermal expansion of pure metals: Copper, gold, aluminum, nickel, and iron," *Phys. Rev.*, vol. 60, no. 8, pp. 597–605, 1941.

[241] R. Liu, A. Vertegel, and E. Bohannan, "Epitaxial electrodeposition of zinc oxide nanopillars on single-crystal gold," *Chem. Mater.*, no. 23, pp. 508–512, 2001.

[242] S. J. Limmer, E. A. Kulp, and J. A. Switzer, "Epitaxial electrodeposition of ZnO on Au(111) from alkaline solution: exploiting amphoterism in Zn(II).," *Langmuir*, vol. 22, no. 25, pp. 10535–9, Dec. 2006.

[243] B. Radha and G. U. Kulkarni, "A Real Time Microscopy Study of the Growth of Giant Au Microplates," *Cryst. Growth Des.*, vol. 11, no. 1, pp. 320–327, Jan. 2011.

[244] B. Radha, M. Arif, R. Datta, T. K. Kundu, and G. U. Kulkarni, "Movable Au microplates as fluorescence enhancing substrates for live cells," *Nano Res.*, vol. 3, no. 10, pp. 738–747, Sep. 2010.

[245] R. Dammel, *Diazonaphthoquinone based resists*, Vol. TT11 . Bellingham, Washington: SPIE Publications, 1993.

[246] X. Wen, W. Wu, Y. Ding, and Z. L. Wang, “Seedless synthesis of patterned ZnO nanowire arrays on metal thin films (Au, Ag, Cu, Sn) and their application for flexible electromechanical sensing,” *J. Mater. Chem.*, vol. 22, pp. 9469–9476, 2012.